Using remote sensing to assess ecosystem resilience

Submitted by Joshua Elliot Buxton, to the University of Exeter as a thesis for the degree of Doctor of Philosophy in Geography in April 2022.

I certify that all material in this thesis which is not my own work has been identified and that any material that has previously been submitted and approved for the award of a degree by this or any other University has been acknowledged.

Signature: 

Abstract

Vegetation ecosystems are increasingly under pressure from both direct human influence and indirect anthropogenically-driven climate change. Increasing amounts of data are made available from satellite systems which can image these ecosystems from afar. The work in this thesis provides several examples of the utility of remotely sensed data from satellites to assess the resilience of ecosystems. This notion of resilience is measured by considering the return rate following a perturbation, with statistical metrics such as AR(1) and variance providing an indication of system resilience and the proximity to a potential tipping point. The first focus of this work is on direct human environmental intervention through community-based agroforestry groups in Kenya. These results show that the efforts of these groups can be detected with satellite data as a greening trend which occurs both within designated tree planting groves and in the surrounding landscape. These groups provide a case study for the power of positive social tipping points to achieve environmental improvement. Following this, the potential of high-resolution satellite data from Sentinel-2 to quantify patterned vegetation in the Sahel is explored. These striking patterns have often been associated with vegetation resilience in drylands. No correlation is found between pattern morphology and resilience, contrary to a previously held hypothesis from the literature. Precipitation is also identified as a key driver of these patterns. Moving beyond drylands, satellite data is utilised at a global scale to assess the link between vegetation resilience and climatic variables across the world. There is a clear relationship between average resilience, as measured by AR(1), and precipitation, which is evident at three spatial scales; the local (pixel), ecoregion and biome. There is also a temperature component, with hotter, drier locations displaying lower levels of resilience. This thesis finishes with a

discussion of the potential for a resilience sensing framework constructed by combining remote sensing data with new cloud computing technologies. This will enable the monitoring of resilience change across the world and the identification of regions which require further investigation and intervention.

Acknowledgements

I must first express my sincere thanks for years of support from my supervisory team; Tim Lenton, Hywel Williams and Chris Boulton.

I am extremely grateful to Tim for his patience, his boundless enthusiasm and his ability to guide research into interesting directions. He has always been willing to give up his time to work with me and has been responsible for all the opportunities I have been offered at the Global Systems Institute. Thanks is also owed to Anne Nicholls for helping me to navigate Tim's hectic calendar.

My thanks go to Hywel, who has always been excited to hear about my work and has helped to improve this research by always being the first to challenge my findings. He has always made me welcome in the SEDALab, where I have felt a valuable sense of community.

Chris has always been quick to offer support and to answer questions at any hour, no matter how repetitive they might be. He has been immensely helpful at offering technical advice and did so long before becoming an official supervisor. I owe him a debt of gratitude for his help, without it much of this research would not have been possible.

I have been most fortunate to have many collaborators who have been willing to provide their expertise and knowledge. Some of them have given up innumerable hours to help. My thanks go to Tom Powell, Kirsten Lees and Jesse Abrams, as well as Nick Barlow and Camila Rangel Smith from the Alan Turing Institute and John Ambler from TIST.

Throughout the writing process I have received much valuable advice from my peers. My thanks go to Michelle Spruce, James Young and Tristan Cann for their support and comradery.

I have been fortunate in having the continued support of both mine and my partner's family. They have always shown an interest in my work, have provided alternate work environments to give me a break from my flat and have listened to long monologues about my (lack of) progress.

Finally, my deepest thanks go to my partner, Sarah North, who has played an integral role in my PhD journey over the last four years. She has always been the first to celebrate my achievements and to support me through difficulties, including caring for me through a 12-month period of Long Covid. Every day her positivity has helped to shape my approach to research and she has inspired me more than she knows. Without her, none of this would be possible.

Table of Contents

List of Figures

Chapter 2

Chapter 3

Chapter 4

Chapter 5

Chapter 6

Appendix A

Appendix B

List of Tables

Chapter 2

Chapter 4

Chapter 5

Appendix A

Appendix B

Glossary of Acronyms and Abbreviations

Acronym	Meaning
AIC	Akaike information criterion
ALN	Abnormally low NDVI
AMOC	Atlantic Meridional Overturning Circulation
AR(1)	Lag-1 autocorrelation
AVHRR	Advanced Very-High-Resolution Radiometer
BoFT	Boreal Forests/Taiga
CAAC	Clean Air Action Corporation
CFA	Community Forest Association
CNN	Convolution Neural Networks
CSD	Critical Slowing Down
DEM	Digital Elevation Model
DFT	Discrete Fourier Transform
DSL	Dry Season Length
DXS	Desert and Xeric Shrublands
ECMWF	European Centre for Medium-Range Weather Forecasts
ERA5	ECMWF Reanalysis 5th Generation
ETM+	Enhanced Thematic Mapper plus
EVI	Enhanced Vegetation Index
EWS	Early Warning Signals
FGS	Flooded Grasslands and Savannas
GEE	Google Earth Engine
GIMMS	Global Inventory Monitoring and Modelling System
GIS	Geographical Information System
GLASS	Global Land Surface Satellite
GPP	Gross Primary Productivity
I4EI	Institute for Environmental Innovation
ICRAF	World Agroforestry
IPBES	Intergovernmental Science-Policy Platform on Biodiversity and Ecosystem Services
IPCC	Intergovernmental Panel on Climate Change
KFS	Kenyan Forest Service
LAI	Leaf Area Index
LOESS	Locally Estimated Scatterplot Smoothing
Man	Mangroves
MAP	Mean Annual Precipitation
Med	Mediterranean Forests, Woodlands and Scrub
MGS	Montane Grasslands and Shrublands

MNDWI	Modified Normalized Difference Water Index
MODIS	Moderate Resolution Imaging Spectroradiometer
MSI	Multispectral Imager
MVWR	Modified Vegetation Water Ratio
NDVI	Normalized Difference Vegetation Index
NDWI	Normalized Difference Water Index
OLI	Operational Land Imager
RGB	Red-Green-Blue
RQ	Research Question
SAR	Synthetic-Aperture Radar
SC	Subgraph Centrality
SPEI	Standardised Precipitation-Evapotranspiration Index
STL Decomposition	Seasonal and Trend decomposition using LOESS
TCF	Temperate Conifer Forests
TeBF	Temperate Broadleaf and Mixed Forests
TGSS	Temperate Grasslands, Savannas and Shrublands
TIRS	Thermal Infrared Sensor
TIST	The International Small Group and Tree Planting Program
TrCF	Tropical and Subtropical Coniferous Forests
TrDBF	Tropical and Subtropical Dry Broadleaf Forests
TrGSS	Tropical and Subtropical Grasslands, Savannas and Shrublands
TrMBF	Tropical and Subtropical Moist Broadleaf Forests
Tu	Tundra
USGS	United States Geological Survey
VODCA	Vegetation Optical Depth Climate Archive
VSI	Vegetation Sensitivity Index

Author's Declaration

Several of the chapters in this thesis have been previously published in full with the input of co-authors or contain work completed by myself which appears in other publications.

Chapter 3 has been published in full as:

Buxton, J., Powell, T., Ambler, J., Boulton, C., Nicholson, A., Arthur, R., Lees, K., Williams, H. and Lenton, T.M., (2021). Community-driven tree planting greens the neighbouring landscape. *Scientific Reports*, *11*(1), pp.1-9. https://doi.org/10.1038/s41598-021-96973-6

For this paper I:

- Conceptualised and designed the study.
- Undertook the study.
- Analysed the data and interpreted the subsequent results.
- Designed and produced the figures to visualise these results.
- Wrote the first draft of the manuscript, which I then edited following comments from co-authors and reviewers.

The version printed in this thesis is as previously published in Scientific Reports, with some minor amendments to ensure consistency in referencing style. The supplementary information for this work can be found in Appendix A.

Chapter 4 has been published in full as:

Buxton, J.E., Abrams, J.F., Boulton, C.A., Barlow, N., Rangel Smith, C., Van Stroud, S., Lees, K.J. and Lenton, T.M., (2022). Quantitatively monitoring the resilience of patterned

vegetation in the Sahel. *Global Change Biology*, *28*(2), pp.571-587. https://doi.org/10.1111/gcb.15939

For this paper I:

- Conceptualised and designed the study.
- Undertook the study.
- Analysed the data and interpreted the subsequent results.
- Designed and produced the figures to visualise these results.
- Wrote the first draft of the manuscript, which I then edited following comments from co-authors and reviewers.

The version printed in this thesis is as previously published in Global Change Biology. The supplementary information for this work can be found in Appendix B. In addition to this, I was involved with the construction of the *pyveg* python packaged which was used for this analysis and is detailed further in Barlow *et al*. (2020).

Chapter 5 is currently being prepared for submission to a relevant journal.

Chapter 6 contains analysis which I designed and undertook as part of the study published in:

Lenton, T.M, Buxton, J. E, Armstrong McKay, D I, Abrams, J F, Boulton, C. A., Lees, K. J., Powell, T. W. R, Boers, N, Cunliffe, A. M, Dakos, V. (2022) A resilience sensing system for the biosphere. *Phil. Trans. R. Soc. B* https://doi.org/10.1098/rstb.2021.0383

For this paper I:

- Conceptualised and designed the global resilience remote sensing component of this analysis.
- Undertook this section of the study.
- Analysed the data and produced the figures for this section of the study (Figures 2 and 3 in the publication).
- Provided advice and editing during the writing stage.

The figures which were produced for my section of this study are reproduced in this thesis in Chapter 6 as they appear in this publication. Additional figures and text have been produced alongside these for this thesis.

In addition to this, the code containing the Google Earth Engine component of the analysis for Chapter 5 and Chapter 6 can be found published online at:
Joshua Buxton. (2022). jbuxt/GEE_Resilience_Sensing: GEE_Resilience_Sensing v1.0.0 (v1.0.0). Zenodo. https://doi.org/10.5281/zenodo.6376843

Chapter 1: Introduction

The anthropogenic impact on natural ecosystems is experienced across the world. There are a myriad of direct effects including land-use change, degradation, deforestation, pollution, and indirect effects through rising temperatures and increased climate variability driven by anthropogenic climate change. This impact is felt so widely the term 'Anthropocene' has been proposed to describe the current epoch (Crutzen, 2006; Lewis and Maslin, 2015). The potential for drastic and irreversible changes in the state of the climate and ecosystems has encouraged research into tipping points (Scheffer *et al.*, 2001, 2009, 2012; Dakos *et al.*, 2008, 2012; Lenton *et al.*, 2008; Lenton, 2011; Kéfi *et eal.*, 2014) and has prompted an examination of the resilience of these systems to change. It is also clear that human communities have the ability to affect positive environmental change, with some authors suggesting the power of tipping points should be harnessed to promote this (Lenton, 2020).

As anthropogenic pressure on ecosystems has grown, so have the tools and data available to monitor these changes Satellites provide the opportunity to analyse inaccessible regions, to complement in situ experiments and to validate models (Woodcock *et al.*, 2008; Thépaut *et al.*, 2018; Wulder *et al.*, 2019). The increasing availability of this data from satellites offers an opportunity to analyse ecosystem resilience and land-use change in regions across the world. Improved resolution and longevity of these satellite systems allows us to conduct analysis across different spatial and temporal scales. These datasets can be applied to detect both direct and indirect human impacts.

Much of the work in this thesis is centred around examining the resilience of ecosystems. Shifts in vegetation resilience due to climate change serves as a measure of the indirect impact that humans may be having on the natural world. This notion of resilience is considered within a tipping point framework, whereby the resilience of a system relates to

its return rate following a perturbation, with declining resilience corresponding to a slowing return rate. This provides an indicator of a systems proximity to a catastrophic shift into an alternative state, i.e. a tipping point. In addition to this, the role of community-based tree planting groups in improving degraded ecosystems is considered. These community groups represent positive change and provide an example of the potential of social dynamics to induce 'positive tipping points'. Through an examination of both direct and indirect anthropogenic influences on ecosystems the utility of remote sensing for monitoring the resilience of the natural world is demonstrated.

The work in this thesis is guided by research questions which are developed through an initial literature review. These questions address themes around our ability to detect changes in the resilience of ecosystems and to understand how these changes may occur through the use of remotely sensed data. This work will assess whether satellite data is capable of measuring the impact of agroforestry community groups in Kenya, to quantify patterned vegetation in the Sahel and to analyse vegetation resilience across the world.

The literature review in *Chapter 2* focuses on summarising the literature around tipping points and ecosystem resilience and some of the available statistical methods to understand these changes. This will start with a consideration of the technical background of tipping point analysis and some of the available methods that enables the measurement of these tipping points. Following this, there is an overview of recent efforts to apply remotely sensed data to ecosystems around the world. At the end of the literature review, there is a discussion of the relevant gaps in the literature and how the research questions develop from these gaps. *Chapter 3* provides a research component of this project which focuses on community based tree planting programs in Kenya. Here an assessment is made of the

impact that these groups have had on the landscape and whether satellite data can be utilised to detect this impact as a greening trend. *Chapter 4* focuses on another dryland ecosystem, the Sahel in northern Africa, and presents an application of remotely sensed data to identify the patterned vegetation which characteristically occurs in these regions. In this chapter the issue of the resilience of these patterned vegetation systems is addressed, as well as the link between this resilience and pattern morphology. Moving beyond drylands, *Chapter 5* explores the capabilities of satellite data and cloud computing resources to assess vegetation resilience across the globe. This resilience is considered at multiple spatial scales, the local (pixel), ecoregion and biome scale. The role of climatic drivers of vegetation resilience is also assessed. *Chapter 6* provides a discussion of the implications of the work presented in this thesis, by considering the potential and limitations of remote sensing for assessing vegetation resilience. This chapter expands upon the global perspective presented in *Chapter 5* with a framework for assessing vegetation resilience trends and offers thoughts on potential future work.

Chapter 2: Literature Review

2.1 Tipping points, resilience and the statistical methods to measure them

2.1.1 Theory of tipping points and resilience

A dynamic system, when exposed to a small perturbation or change in forcing, can undergo an abrupt and substantive shift to a different state (Lenton, 2011). This is known as a 'tipping point'. There are two main ways that these tipping points can primarily occur. Bifurcation can occur when a parameter (or multiple parameters) in the system change, and this causes the system to transition to an alternative state. Alternatively, the state of a system can be shifted by some form of stochastic forcing which pushes the system outside its basin of attraction; this is known as noise-induced tipping. These two forms of tipping can occur in conjunction with each other; as bifurcation in a system approaches, the system's basin of attraction shrinks (see Figure 2.3), therefore making it more conceivable that a perturbation will lead to a state transition, or a 'tipping point'. Ashwin *et al.*, (2012) also identifies a third classification of tipping point known as 'rate-dependent tipping'; these occur when a parameter experiences rapid change and this causes the system to move to an alternate state. This third classification is not considered further here.

The potential for tipping points has been identified in a diverse range of ecological and climatic systems (Lenton, 2011; Armstrong McKay *et al.*, 2021), with recent evidence of approaching tipping points identified in the Atlantic Meridional Overturning Circulation (AMOC) (Boers, 2021), the Amazon rainforest (Boulton, Lenton and Boers, 2022), and the western Greenland Ice Sheet (Boers and Rypdal, 2021). There would be drastic regional and

global impacts should these systems tip into alternative states. Figure 2.1 maps these climate tipping elements and divides them into core and regional tipping points. These core tipping points affect the global Earth system, while regional tipping points act on a sub-continental scale (Armstrong McKay *et al.*, 2021).

Following a tipping point, it can be difficult (or impossible) to tip a system back to a previous state if it experiences hysteresis. The environmental conditions required for a return to its previous state may be different than the conditions required for the initial transition (Scheffer *et al.*, 2001)), as shown in Figure 2.2.

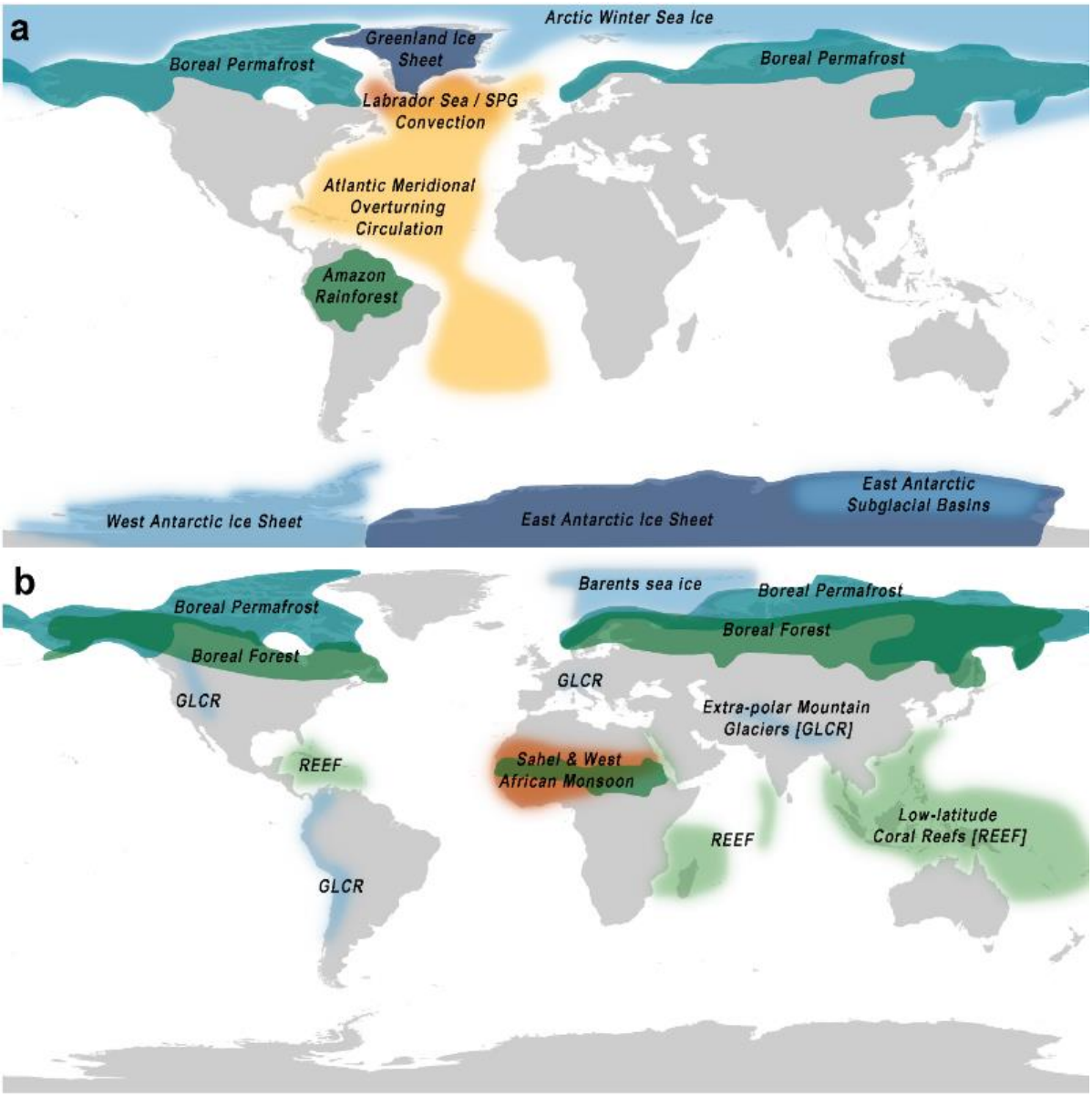

Figure 2.1: Map of potential tipping points across the Earth system that could be passed should global warming continue. Core climate tipping elements are identified in (a) and regional ones are in (b). Green areas relate to the biosphere, orange are ocean-atmosphere and blue are cryosphere. Source: Armstrong McKay et al. (2021).

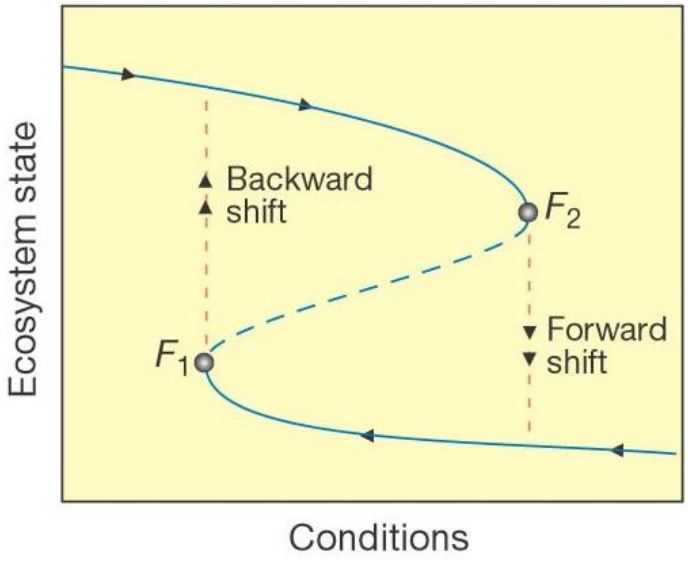

Figure 2.2: Visual representation of hysteresis of an ecosystem. A system may experience a slight change which forces it through the bifurcation point at F_2, resulting in it reaching the alternative state (the lower branch). A return to the previous state requires the conditions to be sufficiently changed to allow the system to pass through the bifurcation point at F_1. Figure adapted from Scheffer et al. (2001).

The potential for tipping points to cause non-linear, irreversible change has increased the interest in this field of study to both scientists and policy makers, with concerns around the occurrence of ecological and climatic tipping points identified in the recent IPCC Working Group 1 Sixth Assessment Report (IPCC, 2021). This requires us to think about the likelihood of a system to tip into an alternative state - its resilience.

Here the notion of the resilience of a dynamic system is considered, an idea which has a long history in the literature, with much discussion over its definition. In one of the earliest publications concerning the idea of ecological system resilience, Holling (1973) defines

resilience as the ability of a system to withstand a perturbation and to maintain internal relationships. Additionally, Holling (1973) presents the idea of stability as the return rate of a system to its initial state following a perturbation. Pimm (1984), however, restricts the definition of resilience to the recovery of the system after a disturbance, as do Grimm and Wissel (1997). In attempt to clarify these definitions, Holling (1996) defines the recovery of the system as 'engineering resilience' and describes their earlier, broader idea of resilience as 'ecological resilience'. It is therefore apparent that these differing definitions of resilience have led to confusion in the literature. Therefore it is necessary to clarify what is meant by the resilience of a system as considered here.

The focus of this work is upon a simple, well-founded notion of resilience which is applicable to both biological and climatic systems. This requires the examination of the response of systems to perturbations and their ability to return to their initial states.

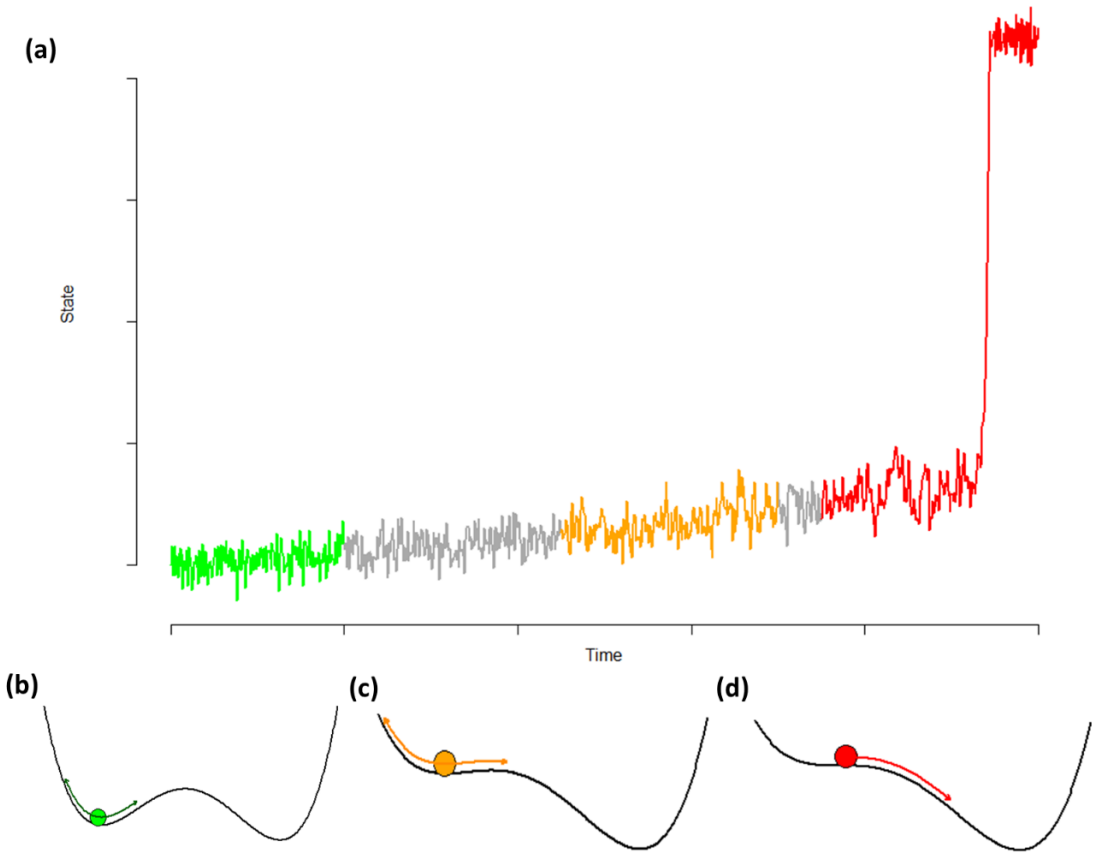

Figure 2.3: Representation of a system losing resilience before undergoing a tipping point. (a) Time series of this system as it loses resilience and then tips into an alternative state. The system experiences critical slowing down prior to the tipping point as it struggles to return to its previous state following a perturbation. The colouring of the time series corresponds to the valley cartoon of that colour. (b-d) Ball in valley cartoon of a system approaching a tipping point. As the system resilience declines over time due to the bifurcation parameter approaching a critical value, the valley becomes shallower and it is easier for the system to be tipped into an alternative state.

Consider some dynamical system, which has a state variable x and an equilibrium state x^* (there may be other equilibria of the system). When this system experiences a perturbation,

it may recover back to its previous state, in this case x*. A potential function, U(x), can be used to describe the attractor of the equilibrium state. This is commonly visualised as a valley, as seen in Figure 2.3, with the equilibrium state x* the bottom of the valley, and the current state of the system, x, shown as a ball. This visualisation includes other valleys, which represent alternative equilibria

This system experiences perturbations, which can be known events, and is also exposed to noise, such as additive white noise η with standard deviation σ. The dynamics of a system experiencing this perturbation at some time point *t* is given as:

$$\frac{dx}{dt} = -U'\big(x(t)\big) + \eta(t) \tag{2.1}$$

In the vicinity of the equilibrium point, *x**, the function *U* can be approximated such that for some value λ < 0 (Scheffer *et al.*, 2009):

$$U(x) \sim -\frac{\lambda}{2}x^2 \tag{2.2}$$

λ is the recovery rate of the system to the equilibrium state *x** following a perturbation; this provides a measure of the negative feedback. A more negative λ corresponds to a faster recovery rate, which suggests that the equilibrium state of the system is more resilient, while a λ closer to 0 corresponds to a slower recovery rate following a perturbation, which means the system is less resilient. As discussed in Scheffer *et al.* (2009), if the dynamics of the system are discretised into timesteps Δt, then the autocorrelation function, α(n), at *n* timesteps and variance can be derived as:

$$\alpha(n) = e^{\lambda \Delta t n} \tag{2.3}$$

$$var(\Delta x) = \frac{\sigma^2}{1-\alpha^2} = \frac{\sigma^2}{1-e^{2\lambda\Delta t n}} \sim \frac{-\sigma^2}{2\lambda} \tag{2.4}$$

For lag-1 autocorrelation (AR(1)), n=1. As the system loses resilience and its return time increase, λ tends towards zero as the likelihood of the system tipping into an alternative state increases. From the equations above, as this happens AR(1) increases towards one, and the variance increases (tends towards infinity). AR(1) and variance are commonly used statistical indicators for pre-tipping point 'critical slowing down' behaviour and are used throughout the literature (Carpenter and Brock, 2006; Lenton *et al.*, 2008; Scheffer *et al.*, 2009, 2012; Lenton, 2011; Dakos *et al.*, 2012).

There are numerous statistical signals that can be detected as a system approaches a tipping point and its resilience declines. These can be classified into those which analyse temporal data and those that consider the spatial properties of a system.

2.1.2 Temporal resilience indicators

As a system approaches a tipping point, its ability to return to its initial state following an external perturbation declines, therefore its return rate begins to decrease and the system experiences Critical Slowing Down (CSD) (Lenton, 2011; Scheffer *et al.*, 2015). As discussed earlier, an increase in lag-1 autocorrelation (AR(1)) is a classic signal of resilience loss in a system. As the system loses resilience and experiences CSD, each time step becomes more correlated with the previous one, and therefore the autocorrelation increases.

Some studies directly consider the return rate of a system following a perturbation as a measure of resilience (Drake and Griffen, 2010; Carpenter *et al.*, 2011), with a lower return rate corresponding to a less resilient system (Wissel, 1984). While this is a simple notion, it can be a difficult metric to measure for large scale climate systems, as it is difficult to

ascertain when a system has sufficiently returned to its equilibrium state. This behaviour is observed in various ecological models (Wissel, 1984; Van Nes and Scheffer, 2007; Chisholm and Filotas, 2009) as well as in lab experiments (Drake and Griffen, 2010).

Measuring AR(1) allows us to gain an understanding of the return rate and therefore the resilience of the system. Increases in AR(1) with loss of resilience and prior to a tipping point has been observed in models (Held and Kleinen, 2004; Boulton, Allison and Lenton, 2014), prior to numerous paleo-climate events using paleorecords, such as the end of the Younger Dryas event and glaciation periods (Dakos *et al.*, 2008) and under controlled laboratory conditions for a diverse range of ecosystems such as zooplankton populations (Drake and Griffen, 2010), aquatic food web collapse (Carpenter *et al.*, 2011) cyanobacteria exposed to increasing light stress (Veraart *et al.*, 2012) and yeast populations exposed to salt shocks (Dai *et al.*, 2012).

Another common identifier for a system approaching a tipping point and losing resilience is an increase in variance (Carpenter and Brock, 2006; Scheffer *et al.*, 2009); as the system loses resilience its ability to return to an equilibrium state declines and the perturbations do not decay away, thus the variance of the system increases. This is often tested alongside AR(1), however some studies identify an increase in AR(1) with loss of resilience without a corresponding increase in variance (Veraart *et al.*, 2012). It has been suggested by Ditlevsen and Johnsen (2010) that an increase in both AR(1) and variance are necessary predictors of a tipping point and that one without the other is not valid. However as can be seen in equation 2.4, variance can change independently of AR(1) as a result of a change in the forcing variability σ. This suggests that requiring both AR(1) and variance to increase is a potentially flawed 'necessary' condition and underlines the importance of AR(1) as a

measure of resilience loss. Other studies consider standard deviation instead of variance (Takimoto, 2009), although these are directly comparable.

Guttal and Jayaprakash (2008) identify skewness as an additional metric for detecting resilience loss in a system prior to a tipping point, as this measures the rising variability within the system. However a change in this skewness metric is only apparent in the classic fold (or saddle-node) bifurcation, rather than other bifurcation types which are symmetrical, such as a pitchfork. Takimoto (2009) suggests that standard deviation is a more robust estimate, with other studies, such as Dai *et al.* (2012) confirming this. Along with variance, skewness can also be used to identify 'flickering', a phenomenon whereby a system with a high level of stochastic forcing can be observed to flicker between the alternative basins of attraction of two states prior to a bifurcation (Scheffer et al., 2009).

Some studies have created and applied composite early warning metrics to detect collapse of whale stocks (Clements *et al.*, 2017), modelled fishing stock collapse (Clements, McCarthy and Blanchard, 2019) and critical transitions within lake ecosystems (Su *et al.*, 2021). In the global resilience analysis in Feng *et al.* (2021), a composite indicator is constructed from numerous early warning indicators in addition to AR(1) and variance, such as skewness and kurtosis.

There must be some consideration given to the response time scale of the system being studied. Faster growing ecosystems, such as grass or shrublands, may demonstrate climate-driven changes in resilience on a different time scale to slower systems, such as forests. The time series interval may not be sufficiently frequent to detect all changes in a system with a fast recovery rate. Also, the length of the time series must be long enough to detect statistically reliable changes in systems (Dakos *et al.*, 2012).

Some studies apply temporal resilience measures across space in a space-for-time substitution. This is useful in systems where the temporal extent of the data is not long enough to observe clear changes in resilience, or to ascertain whether specific climate regimes relate to differences in resilience over large regions. This enables a single resilience indicator for each location to be calculated and related to multiple potential explanatory variables. This form of analysis is used in Verbesselt *et al.* (2016), Eby *et al.* (2017) and Majumder *et al.* (2019) which are discussed further below in *Section 2.3.2.*

2.1.3 Spatial resilience signals

So far consideration has been given to measures which can be applied to time series, i.e. temporal resilience indicators. Now the utility of the spatial component of the data to understand resilience is considered. Some of these are spatial analogues of time series indicators. The correlation between nearest neighbours, the spatial equivalent of AR(1), can be calculated using Moran's i. This spatial correlation would increase as the system loses resilience (Dakos *et al.*, 2010). Similarly, spatial variance is expected to increase with declining resilience, as identified in simple models (Oborny, Meszéna and Szabó, 2005; Guttal and Jayaprakash, 2009) and marine ecosystems (Litzow, Urban and Laurel, 2008). The spatial analogue of skewness has also been identified as a signal of declining resilience (Guttal and Jayaprakash, 2009). In a connected population, Dai *et al.* (2012) identify that the recovery length, that is the distance necessary for these populations to recover from spatial perturbations, increases prior to a tipping point. This is the spatial analogue of the recovery time of a system.

Another method to identify loss of resilience via slowing down in spatial systems is to consider how the spatial spectral properties change. Discrete Fourier Transforms (DFT)

provide a measure of spatial frequency, i.e. how often a pattern repeats within a certain spatial zone. This frequency will decline with spectral reddening as the system loses resilience (Kéfi *et al.*, 2014).

While much attention has been given here to resilience indicators which are the spatial counterparts of traditional temporal early warning indicators, other approaches are unique to the spatial domain. For example, by considering vegetation pattern models as a network, with biomass grid cells as nodes and statistically significant temporal cross correlations forming edges between nodes, Tirabassi *et al.* (2014) demonstrate that increased network connectivity is observed prior to a tipping point. Network based indicators are also considered alongside more conventional early warning indicators to analyse regime shifts in a land-atmosphere-ecological model in (Yin *et al.*, 2016).

In addition to this, the emergence of patchiness within spatial systems can be a measure of system change. In irregular patterned systems patch size frequency can fit certain distributions, such as power- law. Deviations from these distributions can be an indicator of resilience change (Kéfi *et al.*, 2014). Competing feedbacks in ecosystems can lead to the formation of both irregular and regular pattern (Rietkerk *et al.*, 2004; Kéfi *et al.*, 2007; Rietkerk and Koppel, 2008; Von Hardenberg *et al.*, 2010). It has been hypothesised that these patterns given an indication of the underlying feedbacks and resilience of these systems (Rietkerk *et al.*, 2004; Kéfi *et al.*, 2014). Dryland patterned vegetation is a common topic of discussion in the literature around patterns and resilience analysis. This literature is considered further in *Section 2.3.3* and in *Chapter 4*.

2.2 Remote sensing

So far most of the previous studies to detect changes in systemic resilience have focused on the use of models, paleo-records or controlled lab experiments. Remote sensing data from satellites provides an increasingly useful tool for understanding the changing resilience of ecosystems. This section provides a brief overview on the history and developments of remote sensing technology, before discussing recent applications of remote sensing to understanding ecosystem resilience.

2.2.1 History of remote sensing

There are many definitions of what constitutes remotely sensed data (Campbell and Wynne, 2011), but at its simplest it is any data which is acquired at a distance without touching the object (Fischer, Hemphil and Kover, 1976). This was initially done through aerial photography using balloons and then planes (Campbell and Wynne, 2011); however technological developments have led to the frequent use of satellites to gain remotely sensed data. There is also an increasing use of drone technology to collect remotely sensed data for purposes such as plant biomass estimation (Cunliffe, Brazier and Anderson, 2016).

One of the earliest examples of satellite remote sensing systems was TIROS-1, a satellite launched in 1960 which was designed to record meteorological data (Campbell and Wynne, 2011). Landsat 1, a satellite launched in 1972, was the first satellite equipped with a multispectral scanner and was able to record images of the Earth at a resolution of 80m (Short, 1976; Williams, Goward and Arvidson, 2006). Following the launch of 7 more Landsat satellites, the Landsat collection now provides nearly 50 years worth of Earth observation data (Wulder *et al.*, 2019).

2.2.2 Developments in remote sensing

In addition to the Landsat collection, numerous other satellite systems have been established to monitor the Earth system. Remote sensing systems are grouped into two classes – active or passive. Active systems contain an instrument which emits electromagnetic energy and records the resulting reflection. An example of this is the synthetic-aperture radar (SAR) sensor deployed on the Sentinel-1 satellites (Torres *et al.*, 2012). Due to emitting an energy pulse, active sensors are less likely to be affected by cloud cover and can record images at night. Passive instruments are designed to measure energy which is being reflected from the Earth's surface, such as the Operational Land Imager (OLI) and Thermal Infrared Sensors (TIRS) present on the Landsat 8 satellite (Wulder *et al.*, 2019). Data quality from passive sensors can be affected by cloud cover and air quality. Some satellites are equipped with both active and passive instruments, such as Sentinel-3A, which is equipped with a radiometer and radar (Nieke and Mavrocordatos, 2017).

Temporal resolution varies between satellites and is dependent on the return time of the satellite. Some datasets are created by multiple satellites to increase the temporal resolution, i.e. the Moderate Resolution Imaging Spectroradiometer (MODIS) dataset is generated by sensors which operate on the Terra and Aqua satellites (King *et al.*, 2003), or to generate global datasets, such as the Vegetation Optical Depth Climate Archive (VODCA), which utilises data collected from several satellites with active instruments (Moesinger *et al.*, 2020). Spatial resolution can vary from the scale of kilometres, such as VODCA data on the coarser end with a Ku-band resolution of 0.25^{o}x0.25^{o} (approximately 277.5x277.5km at the equator) (Moesinger *et al.*, 2020) and the Advanced Very High Resolution Radiometer (AVHRR) with a spatial resolution of 1.1km at nadir (Cracknell, 1997), down to 30m for

Landsat 8 (Loveland and Irons, 2016) and 10m for Sentinel-2 imagery (Drusch *et al.*, 2012). Commercial satellite imagery is also available at the sub-metre scale and represents a growing dataset of Earth observations (Dial *et al.*, 2003; Tyc *et al.*, 2005).

The sensors on satellites such as Landsat and MODIS are designed to capture images which are composed of data bands from across the electromagnetic spectrum, for example images from Landsat 8's OLI and TIRS instruments are composed of 11 different bands (Loveland and Irons, 2016). The multi-band nature of these images can be used to create indices which detect different properties of land systems; some examples of these different visualisations are given in Figure 2.4. A frequently used example of this is the Normalized Difference Vegetation Index (NDVI), which is calculated from the near-infrared and infrared bands and is used as a measure of vegetation greenness (Rouse, 1973; Rouse, Benton and Haas, 1975), which is a proxy of photosynthetic capability. These properties can be analysed to understand the behaviour and resilience of vegetation systems.

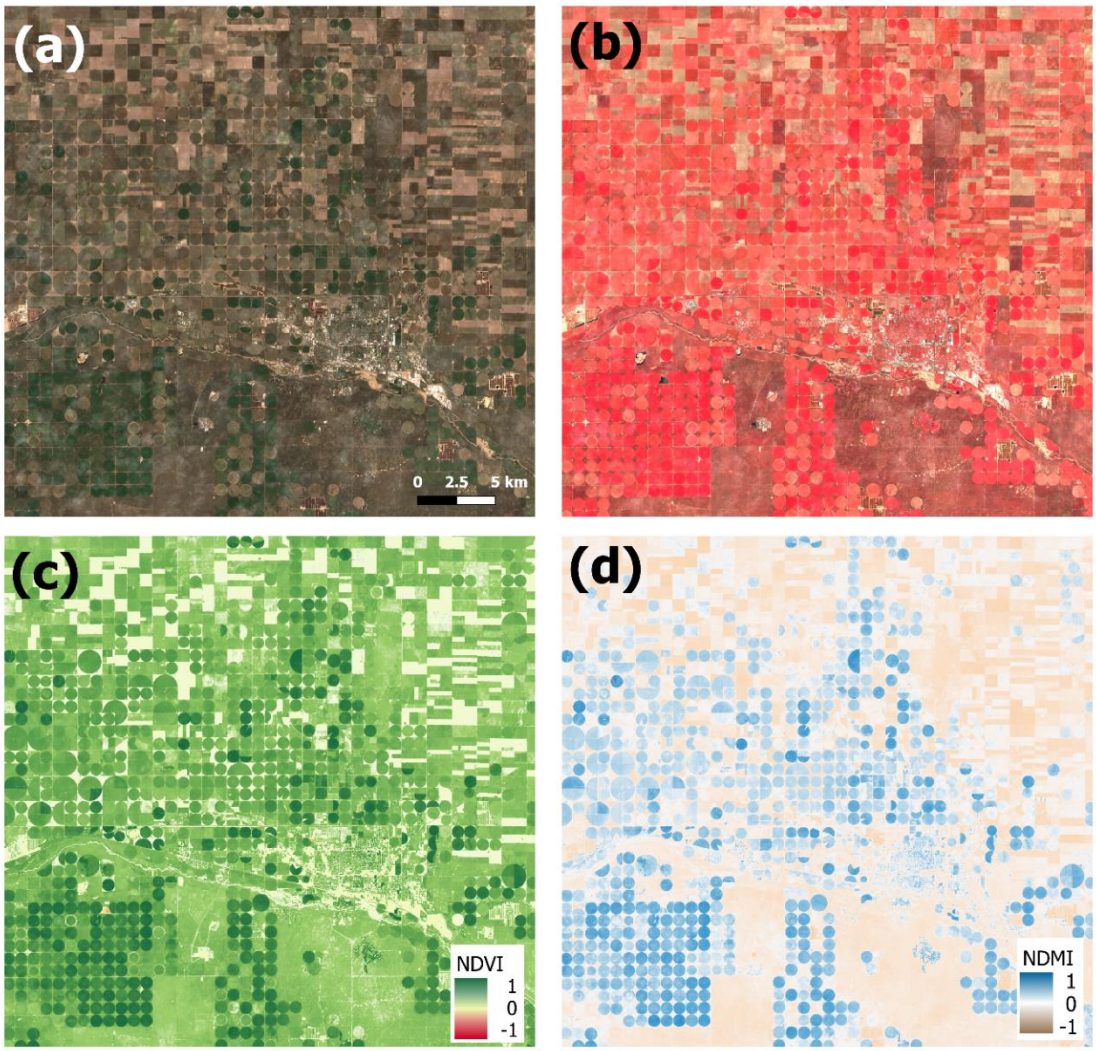

Figure 2.4 : Images from the Sentinel-2 satellite dataset which provide examples of the applicability of multi-band data for vegetation imaging. The region shown is Garden City, Kansas, USA and the surrounding agricultural landscape. The images show (a) a standard RGB image, (b) a false colour image using near-infrared, red and green bands, (c) NDVI, a measure of plant greenness calculated from the near-infrared and red bands, (d) NDMI (Normalised Difference Moisture Index), a measure of plant moisture content which is calculated from the near-infrared and short-wave infrared bands. Higher NDMI values correspond to higher canopy cover with no water stress, while negative values correspond to regions of low vegetation cover or highly stressed vegetation.

Previously, access to remotely sensed data was limited by the high cost of purchasing the data and the GIS software to analyse it, however data has become increasingly freely disseminated (Wulder *et al.*, 2012). For example, one of the largest continuous datasets, the Landsat collection, was made freely available in 2008 by the United States Geological Survey (USGS) (Woodcock *et al.*, 2008).

Another major barrier to the usability of remotely sensed data has been the computational costs associated with analysing big data. The launch of openly accessible cloud computing platforms such as Google Earth Engine (GEE) (Gorelick *et al.*, 2017) and Microsoft's Planetary Computer enables greater access to computational capabilities and allows researchers to utilise the growing resource of remotely sensed data. Combining increased computational power with freely available data provides an avenue for easily accessible continuous monitoring of terrestrial ecosystems.

2.3 Measuring ecosystem resilience with remote sensing data

2.3.1 Analysing vegetation trends

The longevity and spatial cover of remotely sensed data presents an opportunity to monitor vegetation trends and to classify land cover systems. There are numerous studies which apply multi-band data to assess vegetation trends, with AVHRR and MODIS data both popular choices for this (Cai and Yu, 2009). Vegetation trend analysis can be used to assess land degradation at a national level (Eckert *et al.*, 2015; Gichenje, and Godinho, 2018), at a regional level, such as in the Sahel where the interpretation of these trends is the subject of much discussion (Fensholt *et al.*, 2013; Dardel *et al.*, 2014; Knauer *et al.*, 2014; Mbow *et al.*, 2015), and some studies have considered greening trends across the world (de Jong *et al.*, 2011; Fensholt and Proud, 2012; Liu *et al.*, 2015). Some studies seek to analyse these greening trends following a known anthropogenic direct intervention, such as government directed afforestation campaigns in China (Zhang *et al.*, 2016). The importance of understanding and engaging local communities to monitor and avoid land degradation is well known (Gichenje, Pinto-correia and Godinho, 2019; Willemen *et al.*, 2020). However, for most remote sensing studies there is little or no available detailed data on the activities of these communities at a landscape scale.

2.3.2 Application of remote sensing to measure ecosystem resilience

The formulation of long-term time series from satellite data presents an opportunity to consider the resilience of terrestrial vegetated ecosystems. High frequency sampling is

necessary to understand a system's resilience (Scheffer *et al.*, 2009; Dakos *et al.*, 2012); repeated Earth monitoring by satellites addresses this need. In addition to this, remote sensing can provide high resolution data with a large geographical coverage and can enable analysis of regions which may be difficult to access. For this reason, this work focuses on the application of remote sensing to analyse and understand the resilience of ecosystems.

Over the last few years there has been a growth of interest in this field. A non-exhaustive list of relevant studies is provided in Table 2.1 (found at the end of this chapter) which is adapted from Lenton *et al.* (2022) and provide some discussion on some of these recent examples below. These studies utilise a range of satellites and indices to analyse the resilience of various ecosystems. The majority of these studies focus on the regional and local level, however increased computation capacity has encouraged some studies to look at the resilience of ecosystems across the globe. There are a variety of ways that 'resilience' is described in the literature. Some of these consider a framework similar or equivalent to that described earlier in this review, while others take a different approach, with some studies taking more of a 'resistance' perspective.

2.3.2.1 Regional analysis

Verbesselt et al. (2016) utilises a space-for-time substitution method to consider the resilience of equatorial tropical forests. This study uses MODIS NDVI data to analyse tropical forest resilience, as well as Vegetation Optical Depth (VOD) data. However, instead of analysing resilience changes over time, it takes an interesting approach which uses a space-for-time substitution, with mean AR(1) considered across a precipitation gradient. Notably, this study finds increasing levels of AR(1) with declining rainfall, with a sharp decline in resilience observed in areas where mean annual precipitation falls below ~2000 mm year^{-1}.

This threshold may represent a point where tropical rainforests may become more susceptible to wildfires and could be tipped into an alternative savannah state.

A space-for-time substitution method is also used in Eby *et al.* (2017). This is applied along a spatial gradient to assess critical slowing down across the Serengeti-Mara ecosystem. This study uses land classification data to classify pixels as woodland or grassland and considers the impact of rainfall as a driver of land cover types. To analyse critical slowing down they measure spatial variance, spatial skewness, spatial correlation and spatial DFT along these gradients. They find that a transition between grassland and woodland as rainfall increases, with signs of bistable regions of grassland and woodland. As stable grassland gives way to bistable regions along the spatial gradients, spatial variance, spatial correlation and DFT all show signs of an increase.

Van Belzen *et al.* (2017) measures the resilience of a tidal marsh system in the Netherlands by considering the return time of the vegetation using NDVI values from aerial photography. This was done by considering the amount of time that vegetation took to return to a grid cell after it had previously disappeared. In this study, vegetation which experiences higher levels of inundation displays a longer recovery time and is therefore less resilient. Spatial variance and correlation are also tested in this study and are found to be less consistent than return rate at detecting resilience.

The loss of resilience in a wetland system in Iran and Armenia is analysed in Alibakhshi *et al.* (2017). MODIS data from January 2001 to December 2014 is used. A composite multi-spectral index, the Modified Vegetation Water Ratio (MVWR), is created by rescaling a vegetation index, NDVI, and a water index, the Modified Normalized Difference Water Index (MNDWI). AR(1), variance and skewness are used as indicators of a loss of resilience. This

study suggests that the AR(1) of MVWR increases as the system loses resilience and approaches a critical transition.

Remote sensing data from Landsat 7 with a 30m pixel resolution is used to analyse the resilience of Californian forests in Liu *et al.* (2019). These forests are at risk from drought-induced mortality events, with a potential for the system to tip into an alternative shrubland state. Here they utilise NDVI, a measure of plant greenness, along with a Bayesian dynamic linear model to identify changes in autocorrelation. In this study, an early warning signal was identified if the autocorrelation exceeded a certain threshold (the average of the 80^{th} percentile of autocorrelation) for a minimum of three months. This study also considers abnormally low NDVI (ALN) events as precursors to mortality events; these occur when trees shed their leaves due to stress. They find that early warning signals (EWS) are apparent at least 6 months prior to mortality events and provide an earlier indication of resilience loss than ALN events.

Majumder *et al.* (2019) use a space-for-time substitution with MODIS Enhanced Vegetation Index (EVI) data to analyse bistability in woodland and savanna areas in Australia and Congo-Gabon. This analysis is also applied to a control area in the Serengeti. This study considers EVI spatial variance and spatial autocorrelation across transects with a precipitation gradient. It finds peaks in spatial variance and spatial autocorrelation of EVI at thresholds associated with a transition between savannah and woodland. This approach is applied to both transects as well as the wider study area.

White *et al.* (2020) employ MODIS EVI data to propose a framework for calculating the resilience of vegetation across the island of Ireland. Here they consider the recovery rate, variability, recovery time and resistance (as defined as the ability of the system to absorb a

disturbance (Pimm, 1984)). This study identifies long recovery rates with major weather events and crop disturbances.

Boulton, Lenton and Boers, (2022) consider trends in the AR(1) of VODCA data and AVHRR NDVI data to assess changes in resilience in the Amazon rainforest. VOD provides an estimate of plant biomass. While both VOD and NDVI are utilised, the authors identify VOD as a more reliable dataset for the study area. This study investigates the impact of precipitation and human influence as two potential drivers of loss of resilience. Here they find that after 2003 there is an increase in VOD AR(1), which corresponds to a decline in the resilience of the Amazon. This resilience loss is seen across more than three-quarters of the Amazon and is occurring in regions which are closer to human land use, as well as regions with lower mean annual precipitation (MAP).

2.3.2.2 Global analysis

A 'global' analysis of vegetation stability using a subset of MODIS NDVI data for 2001-2006 can be found in De Keersmaecker *et al.*, (2014). This analysis considers NDVI time series for a 7km x 7km area around flux tower sites (meteorological sensors which measure CO_2 and water vaper exchange between the atmosphere and biosphere) in each land cover classifications across the globe. The primary purpose of this study is to assess how the characteristics of the data, i.e. noise, uncertainties etc, can affect stability metrics. The metrics considered in this study are resistance (the impact of a perturbation), resilience (or return rate following a perturbation), and variance. These metrics are considered within the context of the 2003 European heat wave. This study finds that early warning signals are more sensitive to data noise than factors such as time series length. It also shows that

forests display the highest level of resistance and resilience to these perturbations, with grasslands and shrubland showing lower levels of resilience.

De Keersmaecker *et al.* (2015) provides a global analysis of vegetation resilience and resistance through the formulation of an AR(1) model using Global Inventory Monitoring and Modelling System (GIMMS) NDVI data. This model identifies areas of low resilience in semi-arid areas including Australia, southern Africa and western North America. Areas of poor model fit are removed from the study; this includes densely vegetated tropical rainforests and high latitude regions. These areas of poor model fit correspond to areas with snow cover or low levels of vegetation which introduce noise into the data, and regions of densely vegetated forests with a small disturbance signal.

Feng *et al.* (2021) applies remote sensing data to ascertain vegetation resilience across the globe. In this study they utilise monthly NDVI data from the GIMMS dataset covering a time period of July 1981 to December 2015. They calculate a composite early warning indicator from lag-1 autocorrelation, standard deviation, skewness and kurtosis. Resilience loss is considered at two different scales: the local, or pixel, scale and then the global scale. Greater resilience loss is identified at the local scale, with temperature and climatic mean state identified as key drivers of resilience loss. Tundras, deserts and xeric shrubland, montane grasslands and temperate grasslands are all biomes which are identified as having the lowest resilience levels. This study also measures the increase in spatial asynchrony of ecosystems and proposes it as a factor for the stability seen at the global level.

2.3.3 Patterned vegetation

A prime candidate for the application of resilience indicators are ecosystems which form clear and distinct patterns. Patterning in nature is observed across a broad range of systems (Rietkerk and Koppel, 2008), including dryland vegetation, mussel beds and ribbon forests.

Patterns in dryland vegetation are among the most commonly discussed in the literature. These patterns form across the globe in regions which experience low levels of rainfall (Deblauwe *et al.*, 2008). Vegetation pattern formation is an example of Turing patterning (Turing, 1952); they are driven by feedbacks operating across two different scales – the formation of the pattern allows more water for the vegetation within the pattern and in doing so reduces the water availability for vegetation outside of the pattern (HilleRisLambers *et al.*, 2001; Barbier *et al.*, 2006).

Dryland vegetation pattern morphologies are often classified as gaps, labyrinths, 'tiger bush', and spots, with rainfall often identified as the primary driver of these patterns (Meron and Gilad, 2004). It has been hypothesised that as rainfall levels decline, vegetation transitions through these classes, from gaps down to labyrinths, then spots, before finally disappearing to bare ground (Meron and Gilad, 2004). This suggests that the morphology of pattern vegetation provides an indication of the feedback mechanisms of the system and consequently the resilience of the ecosystem (Rietkerk *et al.*, 2004), as visualised in Figure 2.5. It is worth noting that there is an absence of work on establishing the link between patterned vegetation morphology and system resilience using real world data. Much of the work on this has relied on models (Dakos *et al.*, 2011; Siero *et al.*, 2015, 2019). In Dakos *et al.* (2011) critical slowing down is seen prior to vegetation pattern collapse for some classes of vegetation model, however for regular patterns there is no associated change in

resilience indicators, such as AR(1), for this transition. While some studies have used aerial photography to document changes in patterned vegetation (Leblanc *et al.*, 2008; Gowda, Iams and Silber, 2018) and have posited the link between its decline and tipping points (Trichon *et al.*, 2018), more work is required to assess this relationship.

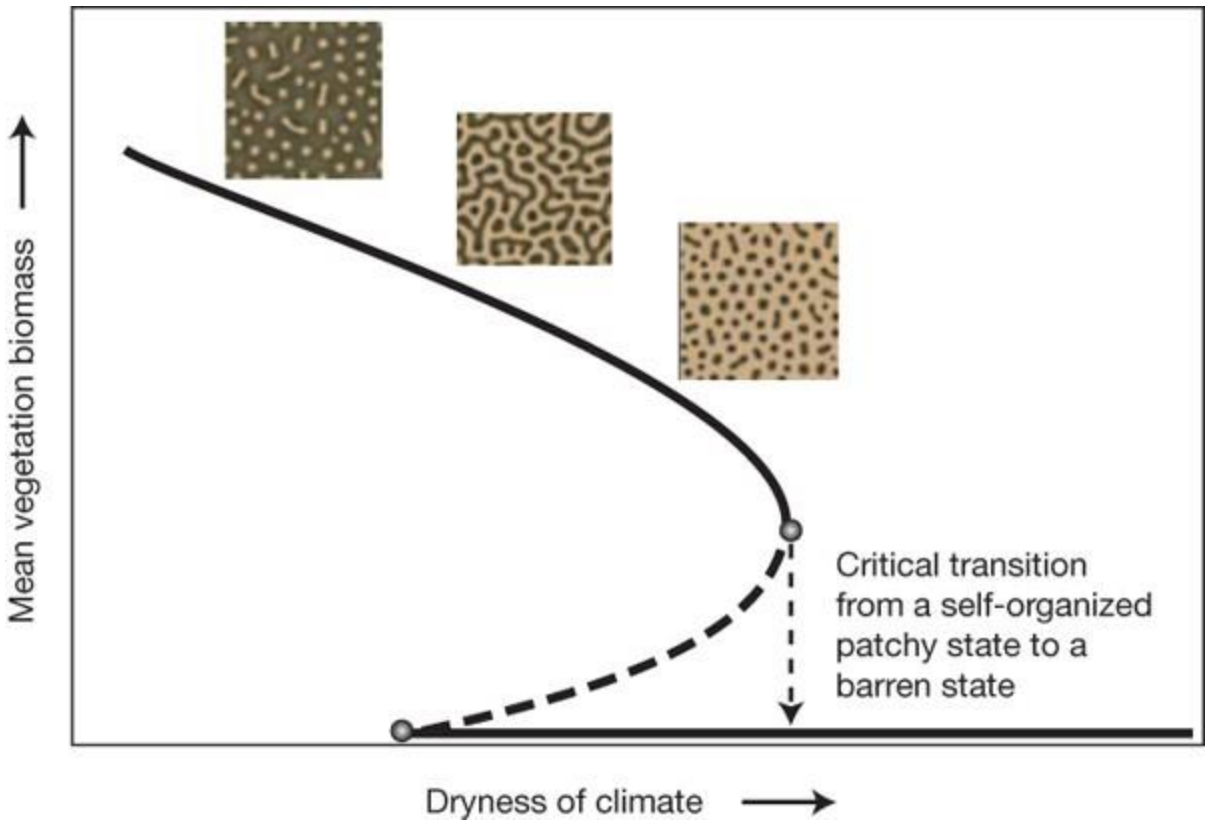

Figure 2.5: Conceptual model of declining resilience of a patterned vegetation system with increasing dryness and a reduction in vegetation cover. Vegetation transitions from gaps through labyrinths and on to spotted vegetation prior to a collapse to a homogenous barren state. Solid lines represent a stable equilibrium state. Source: Scheffer et al. (2009).

There are also suggestions that real world vegetation displays multistability, with multiple forms of patterned vegetation existing within the same area, and that the picture may be more complicated. Rietkerk *et al.* (2021) suggests that spatial pattern formation can help a system to evade a tipping point and can provide more stability.

2.4 Unanswered Questions

2.4.1 Common themes and future directions

As discussed in this literature review, there is a subset of resilience literature which utilises remote sensing to assess vegetation resilience. These studies include those which consider distinct shock events, such as extreme droughts (Lees *et al.*, 2021), and those which consider vegetation resilience over time along with the impact of long term stressors such as precipitation change or anthropogenic pressure (Feng *et al.*, 2021; Boulton, Lenton and Boers, 2022). Some studies also make use of the spatial properties of remotely sensed data to analyse resilience changes across a spatial gradient rather than a temporal gradient (Verbesselt *et al.*, 2016; Eby *et al.*, 2017; Majumder *et al.*, 2019). The nature of spatial data from satellites makes these space-for-time substitutions an ideal method for analysing the resilience of terrestrial ecosystems. This is why it is perhaps surprising that these types of analysis, along with the use of spatial resilience indicators, are less common in the literature.

In addition to this, one would expect that the spatial nature of satellite imagery should, at high enough resolution, provide a way to provide information about the resilience and trends in patterned vegetation. With these sites often occurring in inaccessible locations, thus making constant site monitoring impractical, satellite data should prove useful. However, much of the analysis of these vegetation forms has taken place with limited amounts of aerial photography or spatially limited *in situ* observations. This presents a clear gap in the literature.

As seen in Table 2.1, vegetation indices, such as NDVI or EVI, are among the most commonly used remote sensing metrics for ascertaining the resilience of terrestrial ecosystems. This is likely to be driven by the ease with which they can be calculated from most multi-spectral imagery, rather than requiring a specifically equipped satellite. This allows for the generation of long term time series. In addition to this, NDVI provides a simple, relatively robust measure of vegetation greenness, which serves as a proxy of its health and productivity. The stress experienced by vegetation as it loses resilience is likely to be manifested in reduced recovery rate of photosynthetic capabilities, something which can be detected through NDVI (Liu *et al.*, 2019). However, NDVI is not without its flaws. In regions with low levels of vegetation there is potential for soil to interfere with the NDVI values, while for high biomass areas, such as forests, NDVI values can become oversaturated (Huete, Liu and van Leeuwen, 1997). This has prompted some studies to apply other remotely sensed metrics to forests, such as VOD used in Boulton, Lenton and Boers (2022).

It is clear that remotely sensed data holds great potential for the continued monitoring of the resilience of terrestrial ecosystems in near real time. The availability of free cloud computing resources through GEE and Microsoft's Planetary Computer, combined with a growing body of satellite data, provides the potential for enhanced resilience monitoring efforts of vegetation.

2.4.2 Research questions

As outlined above, with natural ecosystems experiencing the impact of both direct and indirect anthropogenic pressures, there is clear potential for the use of satellite remote sensing data to analyse trends in vegetation cover and resilience. However, there continue to be gaps in the literature. This thesis focuses on three key areas of research; the capability

of remote sensing to identify and evaluate long term greening trends caused by agroforestry community groups in Kenya, the link between dryland patterned vegetation morphology and resilience in the Sahel, and the global relationship between vegetation resilience and climate along with the potential of remote sensing to monitor this. Each of these projects rely on freely available data from satellites, although each operates at a different spatial and temporal scale. The motivation for and the development of each research question is provided below.

To assess the capabilities of remote sensing for monitoring direct human impact on ecosystems, a human network that has undergone drastic growth in the form of an 's-curve' is considered. The case study that is the focus of this work is The International Small Group and Tree Planting Program (TIST), a network of smallholder farmers within the Mount Kenya region. Discussions with local farmers suggest that this tree planting network has had a noticeable impact on their land, however the extent of this has not been quantified. As a deforested area, there is an expectation that tree planting in the Mount Kenya region will have a noticeable effect upon the landscape. The fast vegetation growth rates associated with the tropics also makes this a favourable study area, as well as the overlap between TIST establishment and Landsat data availability. Previous studies have focused on broader, lower resolution trend greening trend analysis (Fensholt and Proud, 2012; Gichenje and Godinho, 2018) or on top-down mass tree planting projects, such as those conducted in Northern China (Zhang *et al.*, 2016). No studies have investigated large scale, dynamic and community led tree planting with high resolution satellite data. This leads us to the first research question (RQ).

RQ1: What effect are community-level tree planting groups having on a dryland landscape and can this be quantified this with remotely sensed data?

While the ability of patterned vegetation morphology to act as a predictor of system resilience has been proposed in the literature, most of the work done to assess this idea has focused on vegetation modelling. In addition to this, few studies have focused on monitoring changes in patterned vegetation in a quantitative manner. The development of high-resolution satellites with frequent return times, such as Sentinel-2, provides a potential tool for assessing these vegetation formations. This prompts the following research questions:

RQ2: Can data from satellites effectively distinguish between different patterned vegetation morphologies?

RQ3: Is the resilience of a patterned vegetation system linked to its morphology?

Much of the literature which applies remote sensing to monitor ecosystem resilience is focused on limited geographical areas or ecosystem types. While some recent studies have considered ecosystem resilience across the globe (Feng *et al.*, 2021; Rocha, 2021), these rely on composite early warning signals or employ confused notions of critical slowing down and observe conflicted trends across spatial scales. The increasing availability of easily accessible cloud computing aids the task of conducting global analysis and provides the potential for the monitoring of on-going changes in the resilience of ecosystems or to identify areas of interest for further evaluation. The following research questions are developed from this:

RQ4: What can be learnt about the relationship between ecosystem resilience and climatic drivers across the globe using remotely sensed data? If these connections do exist, how consistent are they across different geographical and ecosystem scales?

RQ5: Can geographic areas of interest with distinct resilience levels or trends be identified with remotely sensed data?

These research questions will guide the rest of this thesis and will be addressed in each research chapter, as outlined below.

2.5 Thesis outline

The work in *Chapter* 3 considers the Mount Kenya region, which has suffered from historical deforestation and land degradation. A network of smallholder farmers, TIST, have sought to implement agroforestry plots in and around their farms to build resilience. This social scheme is spread through the community. Growth of this scheme follows an s-curve, suggestive of a social tipping point, although this was not tested. However, this represents a clear example using remote sensing to show how 'social tipping' might have a positive impact on the environment, so forms a part of this thesis. In this chapter, RQ1 is addressed by developing an understanding of the impact of tree planting on the local landscape and to identify whether this can be detected using Landsat 7 remotely sensed data. The work in this chapter is adapted from Buxton *et al.* (2021).

Chapter 4 presents an analysis of patterned vegetation across the dryland region of the Sahel. This work seeks to ascertain whether data from remote sensing sources is sufficiently high resolution to distinguish between vegetation pattern classes and provide a method for quantifying vegetation morphology, thus addressing RQ2. This enables an analysis of the resilience of these vegetation sites and to understand what the potential drivers of this resilience might be. In doing so this addresses themes in the literature that link pattern morphology and resilience which have previously only been considered through modelling experiments. This work also aims to analyse the relationship between precipitation and patterned vegetation. *Chapter 4* presents work which is adapted from Buxton *et al.* (2022). The software developed for this study consists of a published python package called *pyveg* (Barlow *et al*, 2020).

A global analysis of vegetation resilience is provided in *Chapter 5*. This study aims to combine the computational capabilities offered by cloud computing with remotely sensed data to assess vegetation resilience across the globe. Here the AR(1) of MODIS NDVI data and VODCA data across the globe is considered and a space-for-time substitution is applied to understand the resilience of vegetation and the effect that climatic drivers have on this resilience. These results are presented across three different spatial scales; the local, ecoregion and biome scale. Results from NDVI and VOD are compared for this form of analysis. In addition to this, some discussion is provided around the potential limitations presented by the temporal resolution of this data.

Chapter 6 provides a discussion of the findings presented in this thesis and considers the utility of remote sensing to determine the resilience of ecosystems. Some of the limitations identified through this work are discussed and avenues for future research are highlighted. In particular, a framework for the long-term analysis of trends in vegetation resilience across the world is proposed, along with the identification of particular biomes which display signs of resilience loss and some potential ecoregions of interest that may require continued study.

Table 2.1: Summary table of select literature concerning resilience analysis using remote sensed data. Adapted from Lenton et al. (2022)

Study	Region	Ecosystem	Satellite	Data product	Time period	Environmental stressor	Resilience Metric	Results	Notes
De Keersmaecker *et al.* (2014)	Global	15 global landcover types	MODIS	NDVI	2001-2006	Sensitivity analysis of early warning signals within context of 2003 European heat wave.	Resistance, return rate and variance.	Forests display highest level of stability. Biased data points have a large impact on resilience metrics.	Study on which characteristics of the data affect stability metrics.
De Keersmaecker *et al.* (2015)	Global	All	GIMMS	NDVI	1981-2006	Temperature, SPEI (Standardised Precipitation-Evapotranspiration Index).	Linear model of standardised NDVI anomaly based on previous time step and climatic factors.	Low levels of resilience in Australia, Southern Africa and drylands in North America.	Pixels which are a poor fit of this model are removed, these primarily correspond to deserts, snow covered high latitudes and densely vegetated forests (presumably due to the fast recovery time of the latter).
Verbesselt *et al.* (2016)	Equatorial tropical rainforests	Tropical rainforests	MODIS	NDVI	2000-2011	Precipitation	Mean AR(1).	Increasing AR(1) in regions with Mean Annual Precipitation	Space-for-time substitution study.

								below 1500 mm per year.	
(Seddon *et al.*, 2016)	Global	All	MODIS	EVI	2000-2013	Water availability, air temperature and cloud cover.	Vegetation sensitivity index	Sensitive regions identified in tropical forests, alpine regions, the Caatinga dryland forest In South America, eastern areas of Australia and steppe regions in central Asia.	This study isn't strictly measuring early warning signals, and is more of a consideration of 'resistance'.
van Belzen *et al.* (2017)	Netherlands - two tidal marshes in Westerschelde Estuary.	Tidal marshes	Digitised aerial photography	NDVI	1976-2012	Seawater inundation.	Recovery rate, spatial variance, spatial correlation.	Longer recovery time with increased inundation. Some trend of spatial variance and correlation, but less robust.	Parallel transplantation experiment is conducted in Maryland, USA.
Alibakhshi *et al.* (2017)	Iran and Armenia	Wetland ecosystem	MODIS	Composite indicator MVWR created from NDVI and MNDWI	2001-2014	Water level fluctuations due to drought and overuse.	AR(1), standard deviation and skewness.	AR(1) and skewness increased as the wetland system loses resilience. One site showed a decline in standard deviation.	

Eby *et al.* (2017)	Serengeti-Mara	Savannah and woodland	Landsat	Land classification map	2000	Precipitation	Spatial variance, spatial skewness, spatial correlation, spatial DFT.	Spatial variance, spatial correlation and DFT all seemed to increase within transitional regions between grassland and woodland.	Space-for-time substitution study.
Schwalm *et al.* (2017)	Global	All	MODIS	GPP (as well fluxnet and observation driven drought modelled data)	2000-2010	Drought	Recovery time	Recovery time most associated with post-drought temperature and precipitation. Tropical and high latitude regions had the longest recovery times. Recovery times from drought have increased over time too.	
Liu *et al.* (2019)	California, USA	Forests	Landsat 7	NDVI	2000-2016	Drought-induced mortality	Autocorrelation of Bayesian dynamic linear model.	EWS are apparent at least 6 months prior to mortality event.	
Majumder *et al.* (2019)	Australia, Congo-Gabon and Serengeti	Savannah and woodland	MODIS	EVI	2010	Precipitation	Spatial variance and spatial autocorrelation.	Peaks in EWS at transitional threshold	Space-for-time substitution study.
White *et al.* (2020)	Island of Ireland		MODIS	EVI	2003-2019	Disturbances from major weather events	Recovery rate, variability, recovery	Long recovery rates associated with	

							time and resistance.	known ‘fodder crisis’ event.	
Wu and Liang (2020)	Global	All	GLASS and GIMMS AVRR	Leaf Area Index (LAI)	1982-2016 and 1982-2011	Temperature, precipitation and soil moisture	Resilience as ratio of maximum resistance to the return time.	Evergreen broadleaf forests show the highest resilience, while deciduous needleleaf trees showed the lowest. No consistent relationship between temperature and resilience.	
White *et al.* (2021)	Island of Ireland	Agricultural pastures	MODIS	EVI	2000-2019	Impact of species richness, land cover heterogeneity and climatic history	Recovery rate, variability, recovery time and resistance.	Long-term history of extreme events leads to slower recovery rates.	
Feng *et al.* (2021)	Global	All	GIMMS	NDVI	1981-2015	Precipitation and temperature	Composite early warning metric created from AR(1), standard deviation, skewness and kurtosis.	Loss of resilience at the 'local' (or pixel) scale. Moist broadleaf forests, montane grasslands, and deserts were most sensitive to change in mean climate state. Not replicated at the global scale.	

Lees *et al.* (2021)	UK	Peatland	Sentinel -1	Synthetic Aperture Radar (SAR)	2016-2019	Drought	Recovery time	Areas with high recovery time, and are therefore less resilient, have suffered from large amounts of human pressure, such as excessive draining.	
Boulton, Lenton and Boers (2022)	Amazon rainforest	Tropical rainforests	AVHRR	VOD	1991-2016	Precipitation and anthropogenic pressure.	AR(1) and variance.	Increase in AR(1) with decreasing rainfall and with distance to human settlements.	
(Rocha, 2021)	Global (Terrestrial and Marine)		FLUXCOM	Terrestrial systems: Gross primary productivity and ecosystem respiration. Marine ecosystems: Chlorophyll-a concentration	Terrestrial systems: 2001-2018 Marine systems: 1998-2018		AR(1), variance, skewness and kurtoses.	Resilience loss is observed in approximately 29% of terrestrial and 24% of marine ecosystems.	Author considers both critical slowing down and 'critical speeding up' as loss of resilience. This seems to not be backed up by established theories of resilience.

Chapter 3: Community-driven tree planting greens the neighbouring landscape

This chapter is based on Buxton, J., Powell, T., Ambler, J., Boulton, C., Nicholson, A., Arthur, R., Lees, K., Williams, H. and Lenton, T.M., (2021). Community-driven tree planting greens the neighbouring landscape. *Scientific Reports*, *11*(1), pp.1-9.

3.1 Abstract

Nature-based solutions to climate change are growing policy priorities yet remain hard to quantify. Here we use remote sensing to quantify direct and indirect benefits from community-led agroforestry by The International Small group and Tree planting program (TIST) in Kenya. Since 2005, TIST-Kenya has incentivised smallholder farmers to plant trees for agricultural benefit and to sequester CO_2. We use Landsat-7 satellite imagery to examine the effect on the historically deforested landscape around Mount Kenya. We identify positive greening trends in TIST groves during 2000-2019 relative to the wider landscape. These groves cover 27,198 hectares, and a further 27,750 hectares of neighbouring agricultural land is also positively influenced by TIST. This positive 'spill-over' impact of TIST activity occurs at up to 360m distance. TIST also benefits local forests, e.g. through reducing fuelwood and fodder extraction. Our results show that community-led initiatives can lead to successful landscape-scale regreening on decadal timescales.

3.2 Introduction

At least 29% of land is degraded globally, negatively affecting living conditions for 40% of people (Le, Nkonya and Mirzabaev, 2016). Land degradation can be driven by deforestation, grazing and poor cropland management, demographic and economic trends, as well as climatic trends (IPBES, 2018). It reduces both the resilience of terrestrial systems to climate change, and the capacity of agricultural communities to adapt (Webb *et al.*, 2017). Extensive land degradation has occurred in sub-Saharan Africa, and is expected to continue in the future (IPBES, 2018), threatening the livelihoods of smallholder farmers by reducing land productivity, eroding soil and reducing soil fertility (Waswa *et al.*, 2013; Mbow *et al.*, 2014).

Agroforestry can reverse degradation, improve soil quality and increase the resilience of smallholder farmers (Thorlakson and Neufeldt, 2012; Lasco *et al.*, 2014; Giusti, Kristjanson and Rufino, 2019), however perceptions of costs and risks among farming communities with marginal livelihoods mean that uptake of restorative practices has not been widespread (Meijer *et al.*, 2015). Agroforestry in degraded African landscapes has potential to sequester significant amounts of carbon (Henry *et al.*, 2009), indicating the potential for carbon markets as a funding mechanism for environmental rehabilitation (Jindal, Swallow and Kerr, 2008) with potentially powerful benefits for participating communities (Estrada and Corbera, 2011), but the need to aggregate sequestration across large numbers of small farms has been identified as a significant barrier (Henry *et al.*, 2009). As such, successful projects are often localised and limited in scalability, and the impacts of grass-roots actions in rural areas are under-quantified. Local knowledge is essential in enabling context-dependent solutions that prioritise the agency of community-members in decision-making (Reed, 2007; Willemen *et al.*, 2020), and successful and sustained adoption is more likely

when farmers are able to adapt new technology themselves and apply in their local context (Meijer *et al.*, 2015), as well as carrying socio-economic benefits for participants (Giusti, Kristjanson and Rufino, 2019). One project offering a scalable, farmer-led approach that accesses benefits from carbon markets is The International Small Group and Tree Planting Program (TIST) (Jindal, Swallow and Kerr, 2008; Shames *et al.*, 2012).

TIST is a farmer-led network of over 100,000 smallholder farmers in Tanzania, Uganda, Kenya and India, organised around agroforestry and regenerative farming practices (Henry *et al.*, 2009). The TIST programme develops and shares best-practices for tree-planting, sustainable agriculture and gender-balanced leadership opportunities, bringing multiple economic, social and health benefits to its members (I4EI, 2014). TIST provides a strong incentive to plant and maintain trees by training farmers to systematically quantify and aggregate tree-growth data, which is packaged as verified carbon credits for sale on international voluntary markets. Trees are generally grown from locally collected seed, with species choice left entirely to the farmer, and many TIST members or their families establish tree nurseries and sell on seedlings to generate extra income. In this study we focus on the Mt Kenya region of Kenya, which has the highest concentration of TIST members across all four countries. Farmers in this region typically grow a range of crops, most commonly including maize, legumes and tubers (Oppenheimer, 2011), with two cropping seasons determined by the two distinct rainy seasons each year.

TIST-Kenya farmers plant a mix of tree species, with over 160 species reported, including more than 90 indigenous species (Oppenheimer, 2011; I4EI, 2014). Species selection is dominated by trees that provide the most reliable products including fuelwood, animal fodder and coppiced timber (Giusti, Kristjanson and Rufino, 2019), often supplemented with

fruit and nut trees which can provide high value crops. Early in the programme farmers planted a high proportion of *Eucalyptus grandis* due to encouragement by the Kenyan Forest Service (KFS). TIST have since discouraged planting of Eucalyptus, but standing trees from this period still represent a high proportion of the total (up to 33.1% in some project areas (I4EI, 2014)). *Grevillea robusta*, a multi-use non-native tree planting of which has been encouraged by World Agroforestry (ICRAF), is also a dominant species, with native and non-native *Acacia* species and a range of others also present in significant numbers.

TIST credits have high value due to their associated social and environmental benefits (I4EI, 2014; CAAC, 2020). In addition to the income derived from carbon credit sales, TIST farmers gain substantial benefits via production of fuelwood, animal fodder, food and diversification of livelihoods, with an estimated average value of USD $1,324 per member per year (I4EI, 2014; CAAC, 2020). Other benefits include shade provision, reduced soil erosion and increased water penetration (Jose, 2009; Lasco *et al.*, 2014), with certain TIST activities aimed at maximising these, e.g. targeted planting in riparian areas (I4EI, 2014). Alongside tree-planting, TIST farmers often use sustainable farming practices such as 'conservation farming' (I4EI, 2014; CAAC, 2020), which can improve soil organic matter and water retention through a combination of no-till planting, mulching and cover cropping (Mafongoya *et al.*, 2016). The rapid growth of TIST, which resembles an s-curve (as seen in Figure A.1), combined with its potential to improve the local environment suggests that it may represents an example of a social tipping point which can affect positive environmental change (Lenton, 2020).

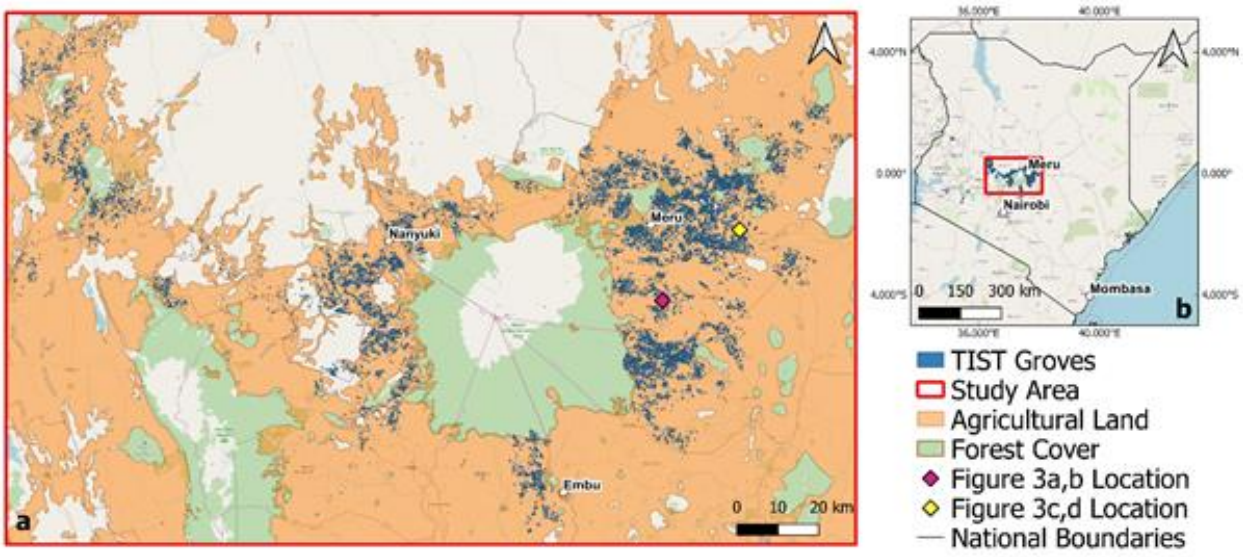

Figure 3.1: Study area: a) Map of TIST groves in the Mount Kenya region and agricultural land within the study area. TIST groves are clustered and spatially correlated within the study area due to the spread of TIST through community networks. b) Map of TIST groves and study area within Kenya. Map data: © OpenStreetMap contributors. Figure created with QGIS.

Here we use Landsat 7 satellite data to examine whether TIST farmers in Kenya have achieved regreening within their own farms and at landscape scale. Figure 3.1 shows the location of TIST tree-groves in Kenya and the study region. We analyse trends in the Normalised Difference Vegetation Index (NDVI), a measure of plant greenness (Wang *et al.*, 2004), over the period 2000-2019 at 34,699 TIST tree-groves established since 2005. A 'grove' represents a defined tree planting area within the boundaries of a farm, which we compare with the wider agricultural landscape. Trends in NDVI are measured using Mann-Kendall's Tau rank correlation coefficient; this statistic indicates the tendency of a trend, with $\tau=1$ showing a continuous increase, $\tau=0$ showing no trend, and $\tau=-1$ showing a continuous decrease. Therefore pixels with a $\tau>0$ value display a 'greening' trend, while

those with $\tau<0$ display a 'browning' trend. As detailed below, we further classify these greening and browning trends as 'moderate' or 'strong', following Gichenje and Godinho (2018). Other studies have used similar methods to analyse trends in NDVI and land degradation across Kenya with lower resolution data (Fensholt and Proud, 2012; Gichenje, and Godinho, 2018).

3.3 Results

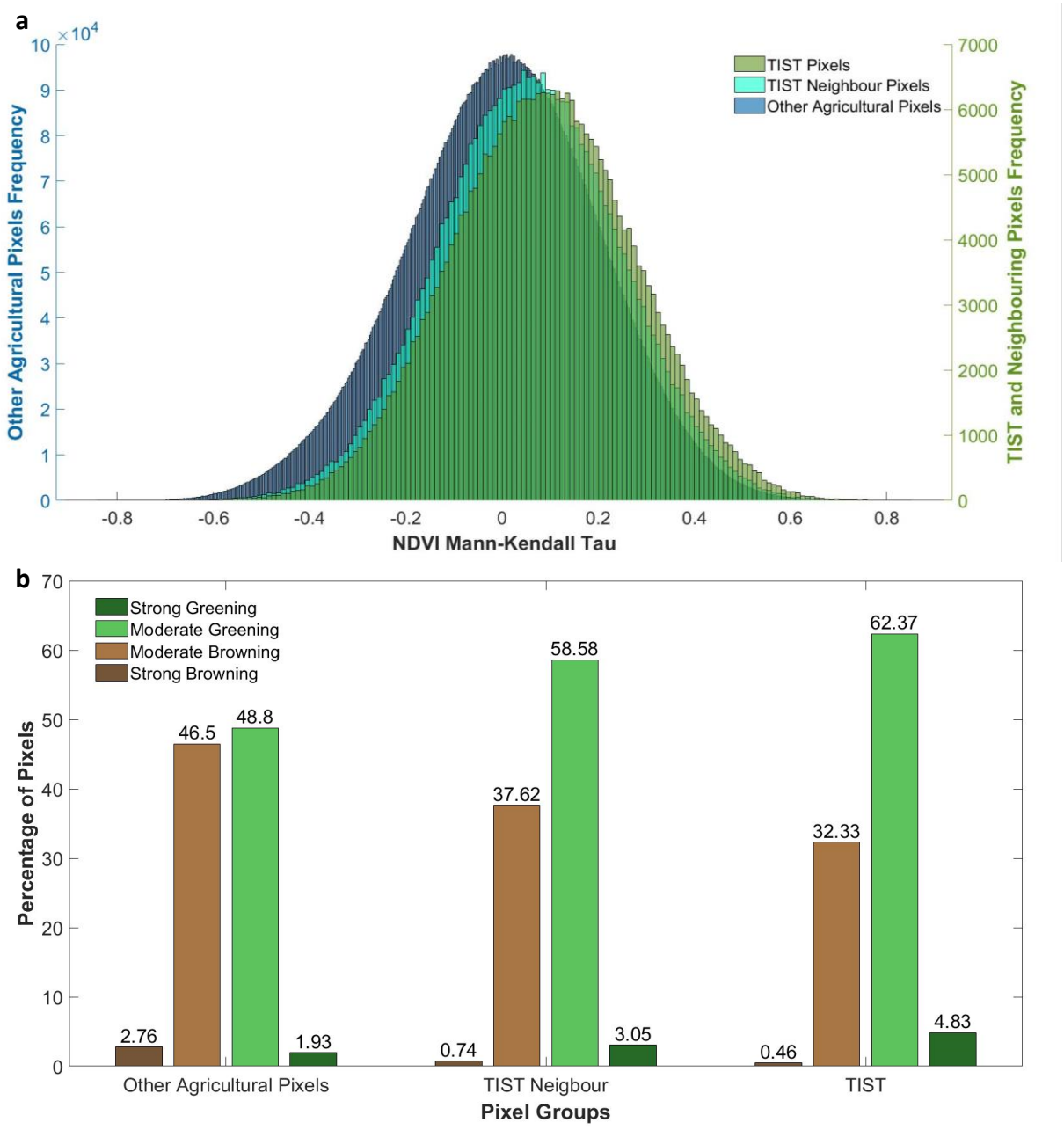

Figure 3.2: Greening trends across study area: (a) Distribution of NDVI Kendall Tau for TIST groves, neighbouring pixels and other agricultural pixels within the study area. Trends in NDVI Kendall tau are positively shifted for TIST groves and neighbouring pixels relative to other agricultural pixels within the study area. (b) Classified greening and browning trends

within TIST groves, TIST Neighbour pixels and other agricultural pixels. Based upon Mann-Kendall Tau values pixels are binned into ordered groups showing "strong browning" (-0.8 < τ < -0.4), "moderate browning" (-0.4 < τ < 0), "moderate greening" (0 < τ < 0.4) and "strong greening" (0.4 < τ < 0.8), following Gichenje and Godinho (2018). TIST grove pixels and TIST neighbouring pixels show a larger proportion of greening pixels than other agricultural land. Over 67% of TIST grove pixels show some form of greening compared to 51% of other agricultural land.

Figure 3.2a shows the distribution of NDVI Mann-Kendall Tau values for pixels which subdivide the study area into three landscape classes: TIST groves, neighbouring pixels and other agricultural pixels. Due to the 30m resolution of Landsat, TIST groves are defined as those which have a centroid either within a TIST grove or a 15m radius from a grove boundary, while neighbouring pixels are defined such that they fall within a 30m buffer of TIST pixels. These neighbouring pixels represent farmland upon which TIST farmers may utilise sustainable agricultural practices, as well as neighbouring farms.

As can be seen in Figure 3.2b, the majority (67.20%) of TIST grove pixels and neighbouring pixels (61.63%) display a positive greening trend, while other agricultural pixels display a broadly neutral trend. A two sampled t-test determined that TIST groves are significantly different to other agricultural areas ($p<0.001$). This suggests that TIST groves are distinct from the wider landscape and that trees planted by farmers contribute an observable change. While not all TIST grove pixels display an absolute greening trend, it is worth noting that there is a large amount of variability across the TIST network in the number and density of trees planted in a grove. Some groves consist of boundary trees or windbreaks, with

crops, buildings or other land use types included within the grove, these may cause a browning trend. Other factors which may cause browning within TIST groves are climatic trends, the possibility that the groves are unsuccessful or the farmer leaves TIST. Neighbouring pixels display a closer similarity to TIST groves than to the rest of the landscape and appear to have a stronger greening trend than other agricultural pixels. TIST neighbouring pixels are statistically significantly different to other agricultural regions ($p<0.001$), as well as to TIST groves ($p<0.001$).

Spill-over effects in the surrounding agricultural landscape due to TIST farmers are likely to be the result of several factors, such as the sustainable agriculture employed by these farmers, as well as the microclimatic effects of tree planting. Figure 3.3a and 3.3b shows an example of a group of TIST groves which are situated within a wider greening of agricultural land.

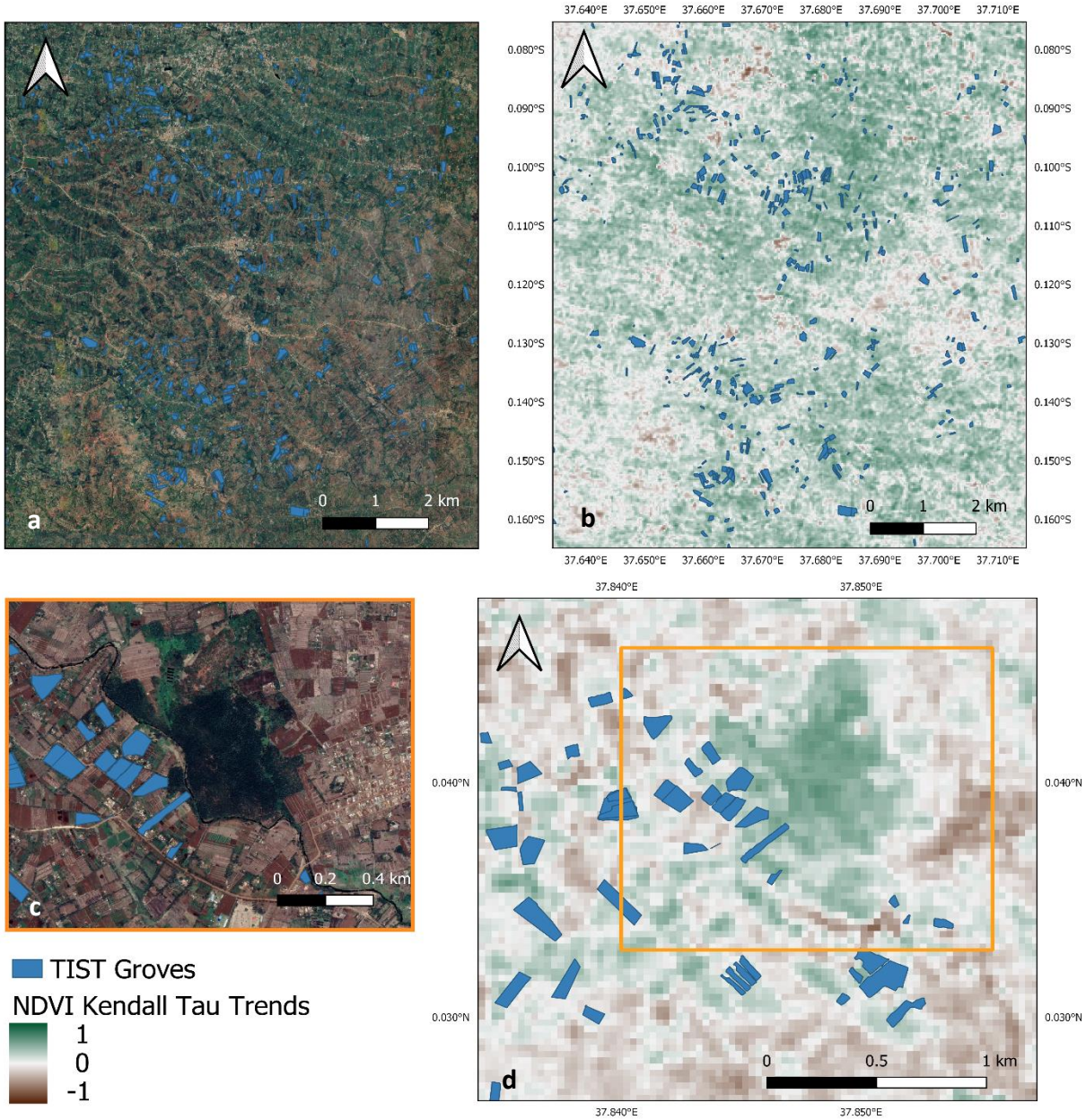

Figure 3.3: Examples of greening in the vicinity of TIST groves: (a,b) Example of a group of TIST sites within a greening agricultural landscape. (a) TIST sites within a heterogenous landscape. (b) NDVI Kendall Tau greening trends for this area. (c,d) TIST sites in Meru County bordering a small woodland. (c) Extent of this small woodland area neighbouring TIST groves. (d) Greening of the woodland. This greening effect is likely to be caused by a reduction in the extraction of firewood and forage from these woodlands and represents a

very specific form of natural vegetation improvement. (a) and (c) map data: ©2020 Google, CNES/Airbus, Maxar Technologies.

Discussions with TIST farmers suggest that in areas with numerous TIST groves there can be co-benefits to local woodland as well as agricultural land. Figure 3.3c and 3.3d shows an example of this, with numerous TIST groves bordering a confirmed natural woodland site which has a positive NDVI Kendall Tau. This strong positive trend is noticeable within the borders of these woodland areas and is in addition to improvements in farmland due to the restorative activities of TIST farmers. This woodland greening trend serves as an additional environmental benefit to the positive trends seen in agricultural land adjacent to TIST sites. Woodland improvements are attributed to a reduction in human pressures on woodland for firewood and forage for animals. Other reasons given by farmers is the creation of woodland protection and education groups due to the increased environmental awareness promoted by TIST membership. TIST have also encouraged members to establish Community Forest Associations (CFAs) (I4EI, 2014).

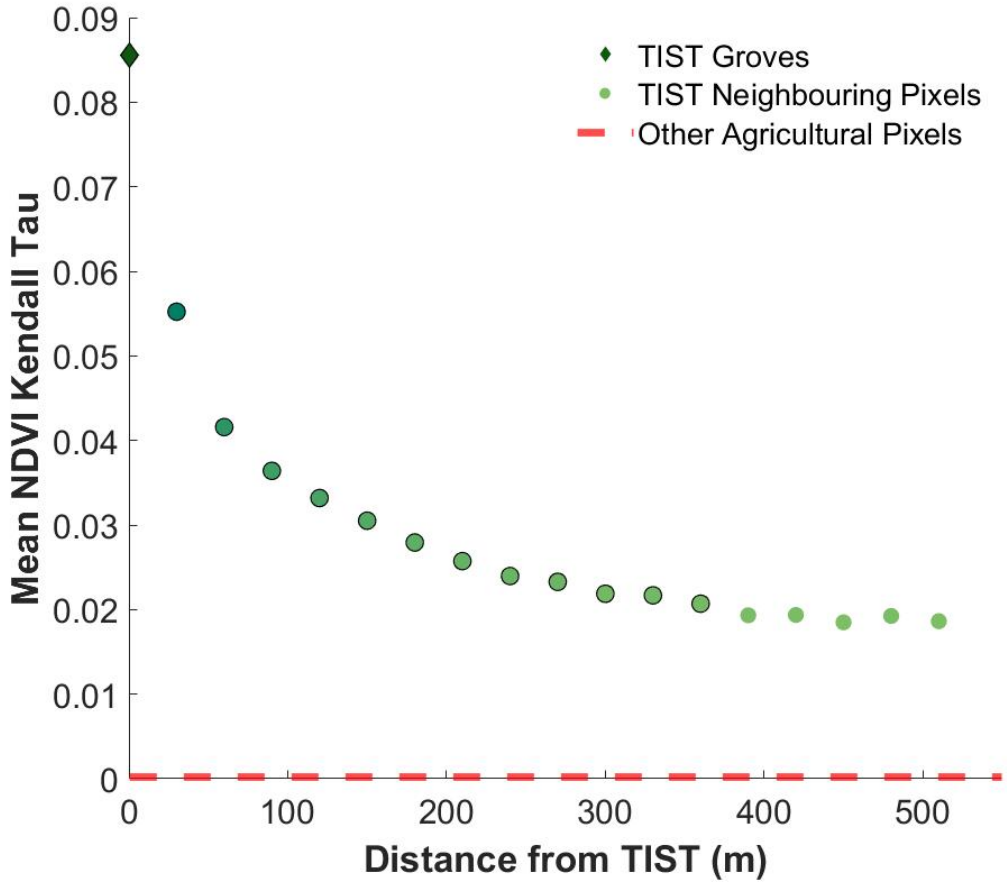

Figure 3.4: Average NDVI Kendall Tau of TIST groves compared with neighbouring pixels at increasing distances: Greening effect of TIST is observable in neighbouring pixels and then declines with distance from TIST groves. The red line represents the average NDVI Kendall Tau value for all Non TIST values in the study area. Distances which display a significant TIST effect are represented with a black outline. Standard error not shown due to very small size, provided in Table A.1.

Figure 3.4 shows the NDVI trend at increasing distance from TIST sites. TIST groves' immediate neighbours have a stronger average greening trend than those which are further away. This TIST effect seems to decay with distance, until it reaches a local background

greening level which is higher than the average trend across the agricultural land within the study area. This suggests that TIST groves are clustered in areas that already show a weak greening trend, but that TIST activities contribute to a greening trend of greater magnitude on top of this. TIST groves are themselves spatially correlated to a degree, as can be seen in Figure 3.1, due to the way that TIST spreads through local community networks. While TIST groves tend to be in areas that experience a greening trend (Figure A.2), background greening is not exclusive to areas with a high density of TIST groves.

The benefits of TIST, such as microclimatic effects and the use of sustainable farming practices adjacent to tree-groves, decline with distance hence the decay in greening. An analysis of the TIST effect over distance considers the asymptotic nature of the curve in Figure 3.4. With the use of a categorical regression model, as detailed in the *methodology*, we establish that pixels do not reach the local background level of greening until 390m away from TIST groves (Table A.2). This suggests a secondary TIST effect present up to 360m away, although this weakens greatly with distance.

3.4 Discussion

Here we have shown that the activities of a community-led tree planting programme are observable using Landsat 7 satellite imagery as increasing greening trends that are clearly distinguishable from the wider landscape. TIST groves display a trend not seen in the rest of the study area, with over 67% of TIST pixels displaying a greening effect, compared to 51% of other agricultural land in the study area. This greening is directly associated with tree planting by farmers in TIST tree-groves over a total area of 27,198 hectares in our study area.

In addition to this, we observe an overspill effect, with land near to TIST groves showing a greening trend. This effect is most strongly observed in pixels immediately adjacent to tree groves, suggesting direct impacts of TIST activities on an additional 27,750 ha of farmland; an area slightly greater than that of the groves themselves. Weaker, but statistically significant, effects can be observed up to 360m away from TIST groves, suggesting that the full extent of TIST impacts in the study area may extend across a further 234,720 ha, leading to a total area of 289,668 ha (Figure 3.5). This spill-over effect highlights a substantive benefit of mosaic tree-planting schemes and shows that membership of TIST, which promotes both tree planting and sustainable agriculture, can have landscape level impacts.

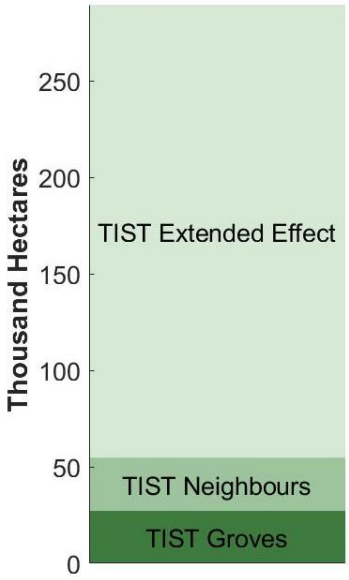

Figure 3.5: Total extent of greening associated with TIST groves.

Spill-over effects from agroforestry programs have previously been identified with regards to community capital and knowledge (Borish, King and Dewey, 2017), and 'positive leakage' of carbon sequestration (De Jong, Bazán and Montalvo, 2007). Spill-over impacts on NDVI trends in our study area are likely to be caused by multiple interacting drivers. Immediately in and around TIST groves, reduced soil erosion, increased soil nutrition and increased shade from TIST planted trees is likely to benefit other vegetation (Jose, 2009; Lasco *et al.*, 2014). There is also evidence that managed tree planting within dry tropical areas can improve groundwater recharge (Ilstedt *et al.*, 2016), which is likely to be of benefit in some TIST groves. In addition to tree-planting, TIST is an example of community capital that serves an important role in generating and spreading other best practices for sustainable land management. Higher yields and the use of cover crops associated with 'conservation farming' (Mafongoya *et al.*, 2016) are likely to play a significant role in the strong greening trend in pixels immediately adjacent to TIST groves, many of which will fall within the boundaries of farms belonging to TIST members. Furthermore, as TIST membership itself is most commonly spread via neighbour-to-neighbour interactions, adoption of beneficial farming practices likely spreads in the same way.

A secondary effect identified by TIST farmers suggests that areas of natural woodland can be improved by the presence of TIST farms, as shown in Figure 3.3c. As farmers produce more animal fodder and firewood within their farm (I4EI, 2014), they are less likely to remove vegetation from local woodland, thus reducing anthropogenic pressure on the woodland (Ndayambaje and Mohren, 2011; Iiyama *et al.*, 2014; Giusti, Kristjanson and Rufino, 2019). In addition, farmers have become more environmentally aware due to their engagement with TIST (TIST, 2011) and some have joined with forest protection groups to

educate others on the dangers of depleting local woodlands (TIST, 2012). Further research is needed to understand the full extent of these effects.

There is currently little available literature which combines remote sensing with grassroots community tree planting. Much of the focus is placed upon large scale, government led projects, such as that in semi-arid Northern China (Zhang *et al.*, 2016). These tree planting projects are often driven from the top down and occur over a large contiguous area, in contrast to farmer-led initiatives that contribute to development of rural livelihoods and which are likely to have more successful adoption and more sustained impacts (Reed, 2007; Meijer *et al.*, 2015). Governments worldwide have announced tree planting projects with large target numbers (Holl and Brancalion, 2020), with international efforts such as the Trillion Tree Campaign and Africa's Great Green Wall. Our results show that the cumulative impacts of a bottom-up, community-driven tree planting initiative can contribute to rehabilitating degraded landscapes, while enabling local farmers to access direct economic benefits from carbon credit payments, substantial indirect benefits from diversified livelihoods and farm improvements (Jindal, Swallow and Kerr, 2008; I4EI, 2014; CAAC, 2020) and agricultural, health and other training opportunities (I4EI, 2014). These restoration schemes can have multiplier effects, with improvements occurring in land adjacent to tree planting sites. This restoration can be achieved with the engagement of local people, with organisations like TIST providing agency to farmers and highlighting the value that these grassroots initiatives can have. We suggest that enhanced community capital and the biophysical and agro-ecological impacts of TIST best-practices combine in a reinforcing feedback to produce widespread, landscape-scale effects, with such programmes representing a mechanism to initiate rapid positive change through social-ecological tipping points (Lenton, 2020).

3.5 Methodology

3.5.1 Study area

The study area outlined in Figure 3.1 covers a total area of 26,864km^2 and was chosen to include TIST groves in proximity to Mount Kenya and the Aberdare Mountain Range. This area constitutes the majority of TIST groves within Kenya as seen in Figure 3.1. The expansion and intensification of agricultural land in the region of Mount Kenya has occurred at the expense of the natural environment, with increasing pressure associated with a growing population (Eckert *et al.*, 2017). Within the Mount Kenya region there exists two rainy and two dry seasons per year. The topography of the region means that there is much spatial variability in rainfall, with mean annual rainfall varying between 600 mm year^{-1} and >1300 mm year^{-1} (Schmocker *et al.*, 2016).

As well as the bounding box around this region, satellite data was then filtered to only include agricultural areas as defined by the FAO (FAO, 2000). This agricultural boundary ensures the removal of pixels within National Parks and forests, large urban areas and other non-agricultural regions, the extent of this is shown in Figure 3.1.

3.5.2 Data

Grove locations and shapefiles were supplied by TIST for this analysis. These shapefiles are constructed of the perimeter of TIST groves and are recorded by TIST quantifiers who walk the boundary of the grove several times to get an accurate measurement using GPS trackers. These groves are usually distinct areas of farms where TIST members have chosen to plant trees and often represent degraded land (I4EI, 2014) where other crops may not be

suitable. However, it is not uncommon for farmers to plant trees around the borders of their farm, meaning that some grove shapefiles will contain the whole farm. TIST grove data in Kenya is provided from the beginning of 2005 up to the end of 2018 and includes TIST groves which have been validated. The median grove size in the study area is 0.285 hectares, with the median number of trees being 83.

Due to the establishment of TIST in Kenya in 2005 and the small size of TIST groves, it was necessary to select a satellite which had both sufficient temporal coverage and spatial resolution. Landsat 7 ETM+ data was used because of its 30m resolution and availability since 1999 (Williams, Goward and Arvidson, 2006). The study period was from January 2000 to December 2019, as this is the largest full year extent available for the satellite. The Landsat 7 Collection 1 Tier 1 8-Day NDVI Composite was selected from the GEE data repository.

This 8 day NDVI composite dataset was used to calculate monthly data based upon the monthly maximum value composite technique. This method selects the maximum value for each pixel within a monthly period and is used in order to reduce the impact of water vapour, cloud cover, aerosols and the angle of the sun (Holben, 1986). This monthly NDVI data was then used to calculate multi-annual monthly averages for the period.

3.5.3 Analysis

The trend in NDVI was calculated using the following steps (see Figure A.3 for workflow). To remove the seasonal cycle from the data, the multi-annual monthly averages are subtracted from the monthly maximum composite. This creates a decycled dataset. Then, to smooth

and detrend the data, a 12-month moving average is taken of the decycled data. Any values which did not fall within a full 12 month window are then removed.

The non-parametric Mann-Kendall tau, or Kendall's tau, is a common test of the trend of a time series. It provides a value between -1 and 1. The Kendall Tau of the detrended and decycled NDVI data set is calculated, with Kendall Tau values of greater than 0 suggesting a greening trend, and thus more vegetation, with values less than 0 suggesting a browning trend of a pixel, and therefore less vegetation.

These pixels are then separated into TIST pixels, TIST neighbour pixels and other agricultural pixels. A pixel is classed as a TIST pixel if its centroid falls within a 15m buffer of a TIST grove. This is to ensure that border areas of TIST groves are included as these are often where a farmer will plant their trees. Pixels are classed as neighbouring to a TIST grove if their centroid falls within a 30m buffer of a TIST pixel. This 30m buffer represents the size of a Landsat pixel. Other agricultural pixels are defined as those which are neither TIST or neighbouring pixels and fall within the agricultural area as defined by the FAO (FAO, 2000) and within the study area.

This method of calculating neighbours is then applied to each successive set of neighbours, with the buffer increasing by 30m each time. Each distance class only includes unique values and ignores values that might be within a smaller distance class. This is done to calculate any spill-over effects of TIST groves, as well as to compare the groves to their local trend. We include all pixels within the study area for the neighbouring analysis to consider non-agricultural land such as national parks.

The magnitude of the trends in greening and browning are then classified as strong browning ($-0.8 < \tau < -0.4$), Moderate Browning ($-0.4 < \tau < 0$), Moderate Greening ($0 < \tau <$

0.4) and Strong Greening ($0.4 < \tau < 0.8$) (Gichenje, and Godinho, 2018). Two sample t-tests were used to assess for statistically significant differences between TIST pixels, neighbouring pixels and other agricultural areas.

To assess the effect of TIST upon neighbouring agricultural land, as shown in Figure 3.4, we considered the declining effect with distance as an asymptotic curve. We consider the largest 3 distances, at 450m, 480m and 510m, as an asymptote of this curve and take the mean of these values. We then fit a categorical regression model with an intercept of this mean and with categories corresponding to each distance class. We then test whether coefficient of each category is statistically different to the intercept (the asymptote value). If a coefficient is statistically different then this suggests that the TIST effect is present, while if it is not statistically different then that distance class does not differ from the local background level.

The remote sensing component of this study was undertaken primarily with Google Earth Engine (GEE) (Gorelick *et al.*, 2017). This data was then extracted from GEE for further analysis in QGIS (QGIS.org, 2021), Matlab R2020a and R (R Core Team, 2021).

3.5.4 Limitations

There are well known difficulties with cloud cover when using remote sensed data to conduct time series analysis. To create a continuous time series and to reduce the influence of cloud cover, this study has relied on decycling and detrending techniques. A reduction in cloud cover influence was also achieved by the use of maximum monthly pixel composites (Holben, 1986). An additional aim of this study was to assess changes in vegetation resilience within the Mount Kenya region due to TIST farmers. However, flickering resilience

signals in adjacent pixels caused by the well documented scan line error of the Landsat 7 satellite (Williams, Goward and Arvidson, 2006) meant that this was not possible. An expanded Landsat 8 dataset may enable this form of long-term resilience analysis in the future. An additional limitation is presented by the TIST grove data. As some TIST groves include the entirety of a farm, this will include cropland and buildings. These are likely to influence the trends in NDVI.

Chapter 4: Quantitatively monitoring the resilience of patterned vegetation in the Sahel

This chapter is based on Buxton, J.E., Abrams, J.F., Boulton, C.A., Barlow, N., Rangel Smith, C., Van Stroud, S., Lees, K.J. and Lenton, T.M., (2022). Quantitatively monitoring the resilience of patterned vegetation in the Sahel. *Global Change Biology*, *28*(2), pp.571-587.

4.1 Abstract

Patterning of vegetation in drylands is a consequence of localised feedback mechanisms. Such feedbacks also determine ecosystem resilience - i.e. the ability to recover from perturbation. Hence the patterning of vegetation has been hypothesised to be an indicator of resilience, i.e. spots are less resilient than labyrinths. Previous studies have made this qualitative link and used models to quantitatively explore it, but few have quantitatively analysed available data to test the hypothesis. Here we provide methods for quantitatively monitoring the resilience of patterned vegetation, applied to 40 sites in the Sahel (a mix of previously identified and new ones). We show that an existing quantification of vegetation patterns in terms of a feature vector metric can effectively distinguish gaps, labyrinths, spots, and a novel category of spot-labyrinths at their maximum extent, whereas NDVI does not. The feature vector pattern metric correlates with mean precipitation. We then explored two approaches to measuring resilience. First we treated the rainy season as a perturbation and examined the subsequent rate of decay of patterns and NDVI as possible measures of resilience. This showed faster decay rates - conventionally interpreted as greater resilience - associated with wetter, more vegetated sites. Second we detrended the seasonal cycle and examined temporal autocorrelation and variance of the residuals as possible measures of resilience. Autocorrelation and variance of our pattern metric increase with declining mean precipitation, consistent with loss of resilience. Thus, drier sites appear less resilient, but we find no significant correlation between the mean or maximum value of the pattern metric (and associated morphological pattern types) and either of our measures of resilience.

4.2 Introduction

Ecosystems with strong internal feedback mechanisms can exhibit multiple stable states. Abrupt changes, known as regime shifts, can occur when such systems pass a tipping point and transition from one stable state to another (Scheffer *et al.*, 2001). Once a system has transitioned to a new stable state it is usually difficult to reverse this transition, due to hysteresis. Hence regime shifts can have severe consequences for those who depend upon an ecosystem. Predicting tipping points in complex systems is difficult because of their inherent nonlinearity. However, a growing body of work has shown that the phenomenon of 'critical slowing down' prior to a tipping point can give generic early warning signals (Dakos *et al.*, 2008; Scheffer *et al.*, 2009; Lenton, 2011). In essence, a system becomes slower at recovering from short term fluctuations before it undergoes an abrupt shift. This is because under steady forcing, the restoring negative feedbacks that maintain the original state get weaker before strong positive feedbacks take over at the tipping point. This precursor signal is often referred to in ecology as 'loss of resilience' - where resilience is defined as the rate at which a system recovers to its initial state after perturbation (Pimm 1984).

Multiple metrics have been employed to measure changes in resilience. Where individual perturbations can be clearly identified, the response time of a system to return back to its initial state can be directly measured (Pimm, 1984; Lees *et al.*, 2021). Where a system is subject to continual stochastic perturbations ('noise'), increasing temporal autocorrelation (e.g. lag-1 autocorrelation; AR(1)) (Dakos *et al.*, 2008) and increasing variance (Scheffer *et al.*, 2009) signal loss of resilience. Spatial equivalents of these temporal signals can also be used (Kéfi *et al.*, 2014). Due to the difficulty in obtaining frequent, high quality spatial data and the high levels of computational power required to analyse it, most studies focus solely

upon spatially aggregated data for time series analysis of systems to analyse their resilience. This difficulty can be mitigated by using space-for-time substitutions (Kéfi *et al.*, 2014; Verbesselt *et al.*, 2016). Other spatial resilience studies are often conducted with modelled data (Chen *et al.*, 2015; Siero *et al.*, 2019) or in laboratory conditions (Dai *et al.*, 2012). Kéfi *et al.* (2014) suggest that a combination of spatial pattern analysis with temporal analysis can improve our understanding of system resilience.

Dryland patterned vegetation belongs to a special class of reaction-diffusion systems, first recognised by Alan Turing (1952), where feedback gives rise to regular spatial patterns. The patterns result from an interplay of a local facilitation mechanism; here plants retain water, and a more distant competition mechanism; this denies other plants water (HilleRisLambers *et al.*, 2001; Barbier *et al.*, 2006). Typically patterns transition from “gaps” to “labyrinths” to “spots” as rainfall declines - then vegetation reaches a tipping point - abruptly disappearing below a critical rainfall level (Meron and Gilad, 2004). Furthermore, different pattern morphologies affect the ability of the system to conserve resources (Mayor *et al.*, 2013). Consequently, in patterned systems the pattern itself may act as a visual indicator of the changing balance of feedbacks - leading to the hypothesis that the pattern could act as a resilience indicator of proximity to a tipping point (Rietkerk *et al.*, 2004; Kéfi *et al.*, 2014). However, Dakos *et al.* (2011) find that different models of vegetation patterning give qualitatively different results for how resilience varies approaching a tipping point. In particular, a ‘scale dependent feedback’ pattern vegetation model displays slowing down prior to a tipping point, but AR(1) does not increase as the pattern morphology transitions. Hence we set out to test the hypothesis of a link between vegetation pattern and resilience with remotely sensed data.

Here, we focus on patterned vegetation in the Sahel, this region extends across Northern Africa from Mauritania in the west through to Chad and central Sudan in the east. The region is characterized by low levels of rainfall (Le Houérou, 1989), depleted soils (Sanchez, 2002), increasing use of marginal lands (Doso Jnr, 2014), weak states and institutions (Raleigh, 2010), extreme poverty (Beegle and Christiaensen, 2019), a growing population (May, Guengant and Barras, 2017), and degradation of land and resources during times of drought (IPBES, 2018). The Sahel became a region of international concern following the severe droughts and famines of the late 1960s and 1970s. It was thought that this would lead to the southwards expansion of the Sahara desert and provoked a broader discussion about desertification (Helldén, 1991; Nicholson, Tucker and Ba, 1998). The changes affecting the precipitation regime and the vegetation across the Sahel were seen, by some, as irreversible (Charney, 1975) and led to the development of the United Nations Convention to Combat Desertification (Herrmann and Hutchinson, 2005). Subsequent changes in precipitation and the apparent recovery of vegetation in parts of the Sahel has caused much debate about the wider resilience of Sahelian vegetation to precipitation changes (Herrmann and Hutchinson, 2005; Kusserow, 2017).

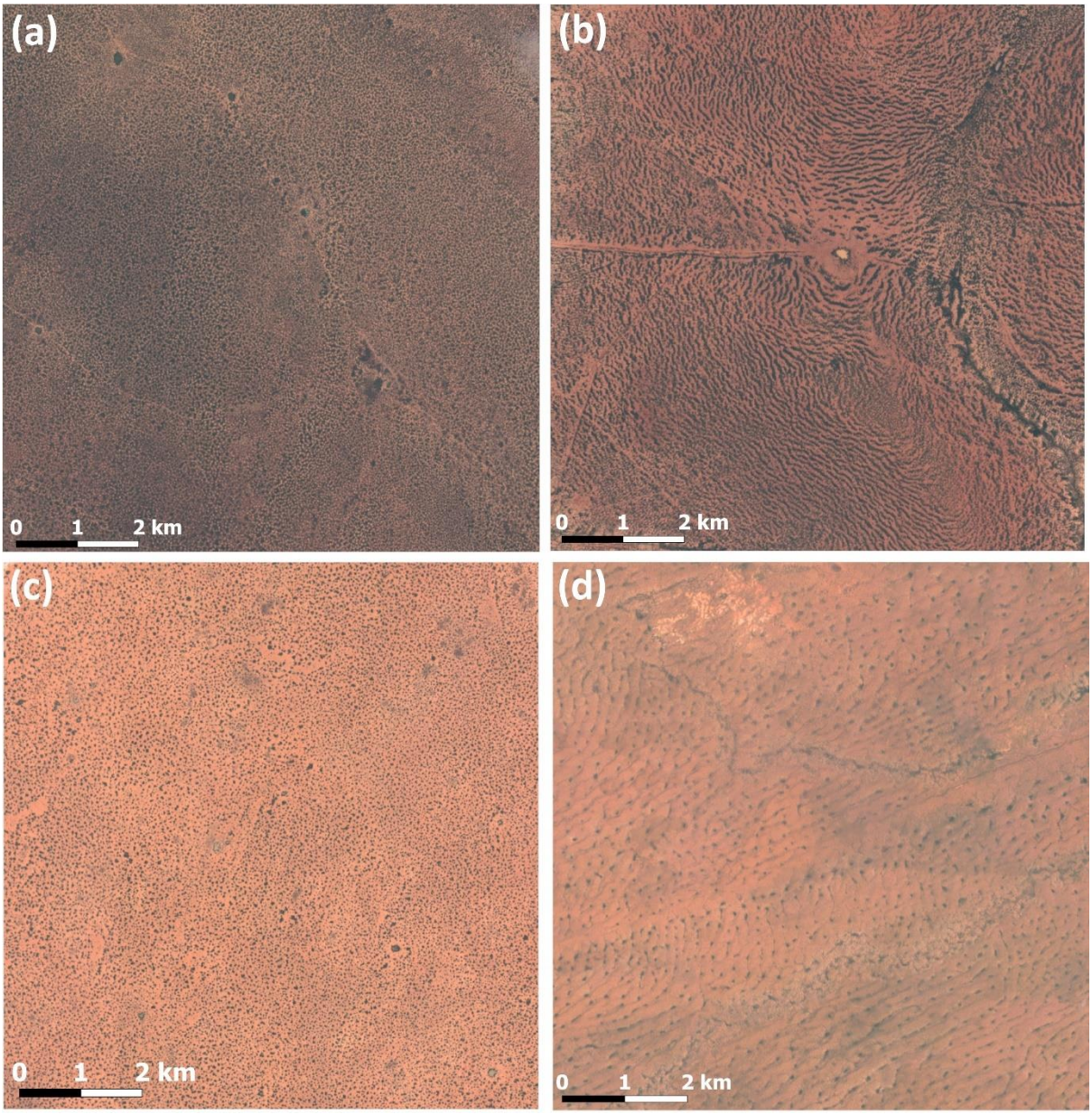

Figure 4.1: Examples of the four classes of pattern vegetation site analysed in this study. (a) Gaps - ID 02 - 10-2016. (b) Labyrinths - ID 01 - 10-2016. (c) Spots - ID 00 - 10-2016. (d) Spot/Labyrinths - ID 28 - 09-2017. All images are of the (cloud free) peak cover of the vegetation within a seasonal cycle.

The pronounced North-South precipitation gradient of the Sahel (Le Houérou, 1989) enables the formation of vegetation patterns of diverse morphologies, including gaps, labyrinths and

spots (Deblauwe *et al.*, 2008; Mander *et al.*, 2017; Trichon *et al.*, 2018), as seen in Figure 4.1. Some of these patterns have previously been studied within the context of wider Sahelian precipitation trends and human influence (Barbier *et al.*, 2006; Leblanc *et al.*, 2008). Trichon *et al.* (2018) present evidence of vegetation patterns undergoing degradation and decline during Sahelian drought periods, with some recovery observed following the increase in rainfall. This recovery is limited to areas of higher precipitation, with northern sites undergoing less recovery. It is suggested that this is due to lower precipitation sites displaying lower resilience and therefore having proceeded past a tipping point during the drought (Trichon *et al.*, 2018). Model studies have shown that in addition to changes in rainfall, overgrazing can decrease the resilience of patterned vegetation and induce tipping points at rainfall levels that would otherwise be stable (Siero *et al.*, 2019).

Few quantitative measures of pattern vegetation are available; these include Fourier analysis (Couteron, 2002; Penny, Daniels and Thompson, 2013), Shannon entropy (Konings *et al.*, 2011) and morphometric analysis (Mander *et al.*, 2017). Due to the necessity of having high resolution data in order to perform these analyses, few studies have quantified changes in patterned vegetation. Existing studies rely on infrequent historical aerial data (Trichon *et al.*, 2018) or consider the changes in vegetation at certain time points relating to human intervention, such as road construction (Gowda, Iams and Silber, 2018) or firewood collection and land-use change (Leblanc *et al.*, 2008). We build upon the method presented in Mander *et al.* (2017) and offer a novel way of continued monitoring of patterned vegetation sites and their response to precipitation. Satellite imagery from Sentinel-2 has the potential to provide high-resolution data over large areas of land at a frequent time step, thereby enabling the changes in pattern vegetation to be analysed across regions.

Here we examine the utility of morphological analysis to distinguish between patterned vegetation classes and the relationship between these patterns and precipitation. We apply our vegetation pattern metric to understand the resilience of patterned vegetation and which factors, such as morphology and rainfall level, affect this resilience. We measure resilience as decay rate following a perturbation, and in terms of AR(1) and variance. We also investigate the spatial distribution of pattern trends across the Sahel in the context of the North-South rainfall gradient and changes in the East-West precipitation regime (Nicholson, Fink and Funk, 2018).

4.3 Methods

In this study we utilise a remotely-sensed resilience monitoring Python toolkit for patterned vegetation, with an initial focus on drylands, called *pyveg* (Barlow *et al.*, 2020). This draws on a number of existing tools and insights. It requires: (1) a source of remotely-sensed data of patterned vegetation, derived from the Sentinel-2 satellite accessed through Google Earth Engine (GEE); (2) a method of turning the qualitative observation of pattern into a quantitative metric called Offset50, based upon feature vector analysis used in Mander *et al.* (2017); and (3) additional data on the potential environmental determinants of resilience, using precipitation data from the ERA5 dataset.

4.3.1 Sites of patterned vegetation

We reviewed existing literature for sites across the Sahel that were characterized by patterned vegetation. We considered a wider range of locations, of an initial 56 sites (8.5km x 8.5km in size) and filtered the sites selected for analysis down to 40 sites, as shown in Table 4.1, based on several criteria. Some initial sites in northern Africa had two rainy seasons per year and were therefore not true Sahelian sites, other historical sites that were reported in the literature were removed as they had suffered such significant degradation that the vegetation morphology was unclear or occupied very small areas, such as a tiger bush and dotted vegetation site in Burkina Faso (Leprun, 1999). Other sites were removed due to unclear vegetation patterning or incorrect labelling (see Table B.1 for full list) or due to outliers linked to too small vegetation to be recorded (Figure B.4). Of the sites considered as part of this analysis, 13 are in Mali, 2 in Mauritania, 5 in Niger, 1 in Nigeria, 4 in Senegal and 15 in Sudan (Figure 4.2 and Table 4.1). The chosen sites represent a mix of different

types of patterned vegetation with 7 sites demonstrating gaps (near complete vegetation coverage with patches of bare ground), 12 demonstrating labyrinths (interconnected vegetation and bare soil) and 11 demonstrating spots (clusters of vegetation surrounded by near complete bare soil), examples of these are given in Figure 4.1. In addition to these recognised vegetation patterns, we include sites which we call 'spot-labyrinths', these patterns seem to be highly dependent on precipitation and have more dramatic annual changes than spots or labyrinths. The form that these patterns take post-precipitation is determined by the landscape, with the precipitation that collects in small channels and gullies enabling the spread of this vegetation (an example of the topography of this region is provided in Figure B.3). In the dry season the 'spot-labyrinth' patterns often appear to be isolated, highly degraded spots. However, following the rainy season the vegetation will spread across the landscape and form 'labyrinth-esque' patterns. There are 10 of these 'spot-labyrinth' sites. They are included due to their resemblance to other vegetation patterns and rapid changes across their annual cycles. The pattern morphology of sites were classified by inspection by considering the images of the sites across the whole time series, with particular focus given to the fullest extent of vegetation following a rainy season. This was done by two researchers initially, before consensus was gained from the rest of the authors.

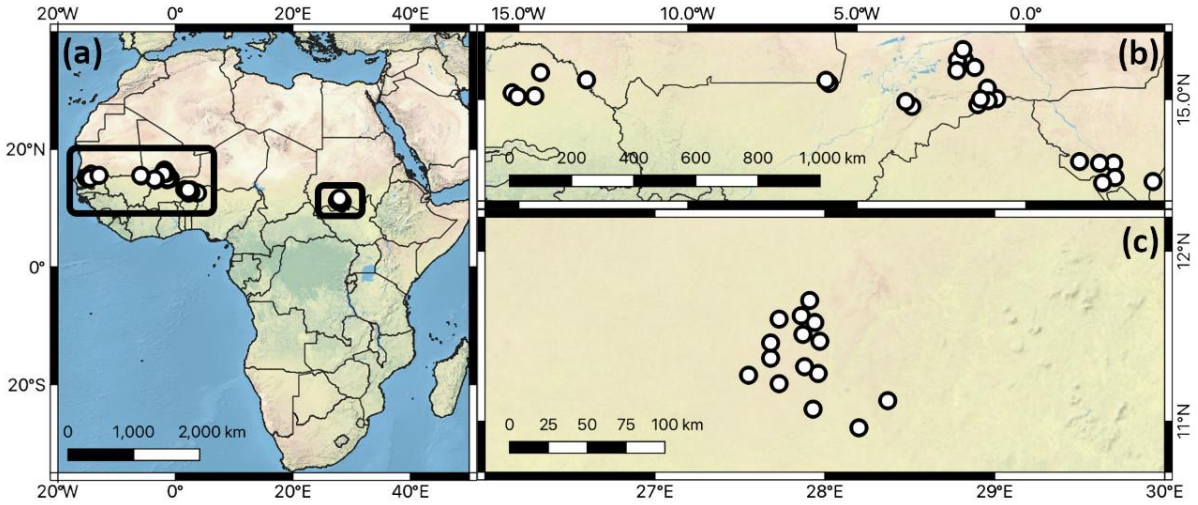

Figure 4.2: Map of patterned vegetation sites within the Sahel in North Africa. Western sites are shown in panel (b) and eastern sites are in panel (c).

Table 4.1: Table of patterned vegetation sites included in this study.

ID	Country	Latitude	Longitude	Type	Source
0	Sudan	11.58	27.94	Spots	Mander *et al.* (2017)
1	Sudan	11.12	28.37	Labyrinths	Mander *et al.* (2017)
2	Sudan	10.96	28.2	Gaps	Mander *et al.* (2017)
3	Niger	13.12	2.59	Labyrinths	Valentin and d'Herbès (1999)
4	Niger	13.17	1.58	Labyrinths	Valentin and d'Herbès (1999)

5	Senegal	15.2	-15.2	Labyrinths	Deblauwe *et al.* (2008)
6	Senegal	15.09	-15.04	Labyrinths	Deblauwe *et al.* (2008)
7	Senegal	15.8	-14.36	Gaps	De Wispelaere (1980)
8	Senegal	15.11	-14.53	Gaps	De Wispelaere (1980)
16	Mali	15.03	-0.87	Spot-labyrinths	Leprun (1999)
18	Mali	15.34	-1.15	Spot-labyrinths	Leprun (1999)
20	Mali	14.85	-1.43	Spot-labyrinths	Leprun (1999)
21	Mali	14.97	-1.12	Spot-labyrinths	Leprun (1999)
23	Mali	15.02	-1.35	Spot-labyrinths	Deblauwe *et al.* (2008) (by inspection)
25	Mali	16.19	-1.83	Spot-labyrinths	Deblauwe *et al.* (2008) (by inspection)
26	Mali	16.17	-2.03	Spot-labyrinths	Deblauwe *et al.* (2008) (by inspection)
27	Mali	16.48	-1.87	Spot-labyrinths	Deblauwe *et al.* (2008) (by inspection)
28	Mali	15.95	-1.52	Spot-labyrinths	Deblauwe *et al.* (2008) (by inspection)
29	Mali	15.86	-2.05	Spot-labyrinths	Deblauwe *et al.* (2008) (by inspection)

30	Mali	14.8	-3.38	Labyrinths	Leprun (1999)
31	Mali	14.94	-3.56	Labyrinths	Leprun (1999)
48	Mali	15.48	-5.83	Labyrinths	Audry and Rossetti (1962)
49	Mauritania	15.57	-5.92	Labyrinths	Audry and Rossetti (1962)
50	Mauritania	15.58	-13	Gaps	De Wispelaere (1980)
51	Nigeria	12.58	3.75	Labyrinths	Barbier *et al.* (2006)
52	Niger	12.7	2.63	Labyrinths	Barbier *et al.* (2006)
53	Niger	12.54	2.26	Gaps	Barbier *et al.* (2006)
54	Niger	13.12	2.17	labyrinths	Barbier *et al.* (2006)
55	Sudan	11.07	27.93	Gaps	Mander *et al.* (2017)
56	Sudan	11.28	27.96	Gaps	Mander *et al.* (2017)
57	Sudan	11.27	27.55	Spots	Mander *et al.* (2017)
58	Sudan	11.47	27.97	Spots	Mander *et al.* (2017)
59	Sudan	11.51	27.87	Spots	Mander *et al.* (2017)

60	Sudan	11.22	27.73	Spots	Mander *et al.* (2017)
61	Sudan	11.62	27.86	Spots	Mander *et al.* (2017)
62	Sudan	11.32	27.88	Spots	Mander *et al.* (2017)
63	Sudan	11.37	27.68	Spots	Mander *et al.* (2017)
64	Sudan	11.6	27.73	Spots	Mander *et al.* (2017)
65	Sudan	11.46	27.68	Spots	Mander *et al.* (2017)
66	Sudan	11.71	27.91	Spots	Mander *et al.* (2017)

4.3.2 Satellite data and preliminary data processing

The data used in this analysis were taken from the Sentinel-2 satellite, which captures remotely sensed data with a resolution of 10m with its multispectral imager (MSI) (Drusch *et al.*, 2012). This resolution provides enough clarity to visualize vegetation patterning. For the purpose of this study, Sentinel-2 data from January 2016 to December 2019 was extracted from Google Earth Engine (GEE), a data repository and cloud computing service (Gorelick *et al.*, 2017). Large scale data analysis was undertaken using the Microsoft Azure Cloud computing service.

Our data processing workflow is as follows and is outlined in Figure 4.3. We start preliminary data processing by creating monthly median composites of the multi-band Sentinel-2 data. This is done in order to remove extreme pixel values caused by clouds, air pollution, and sun

angle. From these monthly multi-band images two sets of images are constructed; Red-Green-Blue (RGB) images and Normalized Difference Vegetation Index (NDVI) images. NDVI is a measure of plant health and is connected to the level of chlorophyll in plant leaves (Rouse, 1973), it is calculated from multispectral images using the near-infrared (NIR) band and the red band (RED), and is defined as:

$$NDVI = \left(\frac{NIR - RED}{NIR + RED}\right) \tag{4.1}$$

These NDVI images are rescaled from the original -1 to 1 in order to fit a 0-255 greyscale. Prior to the morphological analysis of vegetation patterns, several image enhancement steps occur for the greyscale NDVI images. Image contrast is increased through histogram equalization, these images then undergo adaptive thresholding to classify vegetation pixels as black and background pixels as white. This adaptive thresholding step calculates the mean brightness of a 51x51 pixel block around each pixel, and offsets this value by 5 to create the soil-vegetation threshold. Median filtering is also applied to reduce noise within the image. Once processed, these images are then divided into a 17x17 grid of 50x50 pixel sub-images, these sub-images contain the same number of pixels as those used in Mander *et al.* (2017).

Sub-image patterned vegetation is quantified using the network centrality calculation first described in Mander *et al.* (2017). A graph with vertices corresponding to each pixel is formed for each binary sub-image. If a vegetation pixel falls within a 3x3 neighbourhood of another, then an edge connects the corresponding two vertices. These graph vertices are then ranked using subgraph centrality (SC) (Estrada and Rodríguez-Velázquez, 2005). For some vertex *v*, with a non-negative integer *l*, where u_l is the number of closed walks with length *l* which begin at *v*, the centrality of the vertex *v* is given by:

$$SC(v) = \sum_{l=1}^{\infty} \frac{u_l(v)}{l!} \tag{4.2}$$

This can be calculated using eigenvalues and eigenvectors of the graph's adjacency matrix. These vertices are then collected into a sequence of expanding subregions based upon their subgraph centrality rank. 20 of these subgraphs are formed, beginning with the top 5% vertices, with the groups then expanded by each 5% increment. A graph, designated *G*, to describe each subregion is composed of each connected component. We define the Euler characteristic of a subregion as:

$$\chi(G) = V - E \tag{4.3}$$

Where *V* is the number of vertices of the graph *G*, and *E* is the number of edges. This Euler characteristic is plotted for each subregion of an image in order to create a 20-dimensional feature vector which describes the morphology of a pattern vegetation image.

In order to generate a single value corresponding to a pattern's morphology, we subtract the feature vector value at the 50% point from the 100% point of the feature vector. This was chosen as this part of the vector is often more linear than the slope at the start of the vector, and allows us to convert from a vector to a scalar value. We call this value the 'Offset50'. Each sub-image has an Offset50 value, these are then averaged to form one Offset50 value per image. This process is then repeated across the full extent of the available satellite data in order to create an Offset50 time series.

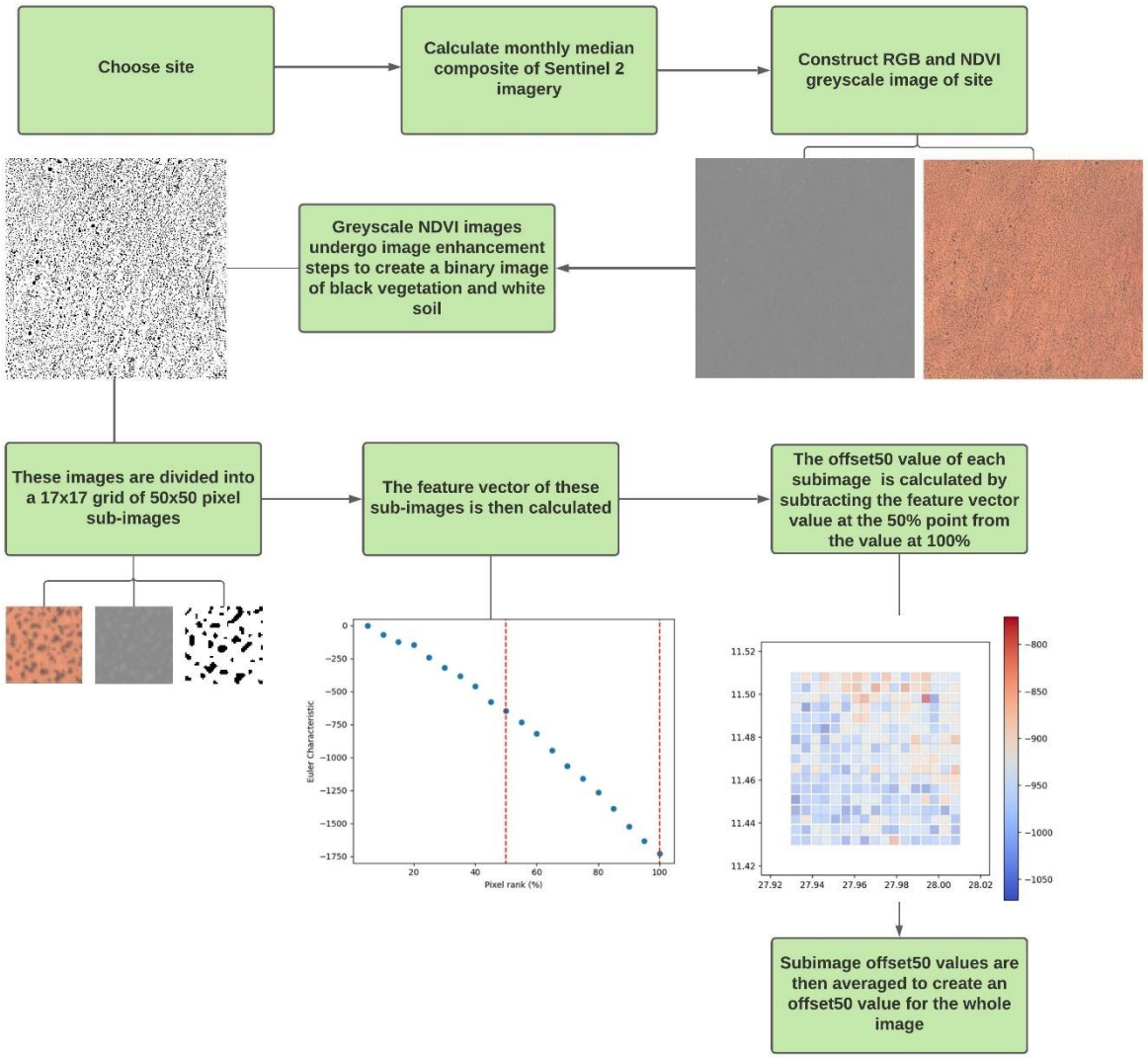

Figure 4.3: Data analysis workflow. This flow diagram shows the steps taken to calculate the Offset50 value of a patterned vegetation site (ID: 58).

Steps are taken at several stages of this process to ensure high data quality and to mitigate the effects of cloud cover on Offset50 values. The formation of monthly median images removes some influence of cloud cover and aerosols. Cloud masking is applied to Sentinel 2 images in GEE; pixels which are masked will appear as completely black pixels. When the images are separated into sub-images, any sub-image which appears as completely black,

due to clouds or unsuitable vegetation morphology, or completely white, such as bare soil, is rejected. For each sub-image within a given month that is rejected, we resample this by taking the mean of the same sub-image in the same month in other years. Despite this step, some interference due to cloud cover is still possible and small clouds can still be present in final images and sub-images which can lead to spurious NDVI or Offset50 values. Any values which are more than three standard deviations away from the time series mean are classed as outliers and are removed.

In images which consisted of small amounts of patterned vegetation or of mixed land cover, such as patterned vegetation and seasonal agriculture, we tested methods to remove the influence of non-patterned vegetation. These methods include reduced image sizes and image classifiers and are detailed further in the supplementary information provided in *Appendix B* (Figures B.1 and B.2). However, we found that these steps did little to change the trend of the results.

4.3.3 Weather data

Daily precipitation data is taken from the ERA5 dataset via Google Earth Engine, which is a comprehensive reanalysis that provides hourly estimates of a large number of atmospheric, land and oceanic climate variables. Currently, ERA5 data is available from 1979 to within 5 days of real time (Hersbach *et al.*, 2020). The dataset has a resolution of 31km and is formed by combining as many historical observations as possible with an atmospheric model that is coupled with a land surface model and a wave model (Hersbach *et al.*, 2020). We generate monthly averages of the ERA5 precipitation data obtained from GEE to compare with monthly NDVI and Offset50 values by plotting precipitation time series against the Offset50 time series (Figure 4.7) and the mean annual precipitation values at different sites.

Precipitation data from 1986 - 2016 is also included in this analysis to understand the role that historical precipitation has played in the formation and stability of patterns. Furthermore, we calculate the cross-correlation of Offset50 and precipitation at increasing time lags.

4.3.4 Resilience - Decay rate analysis

One way to calculate the resilience of these patterned vegetation systems is to consider rainfall as a perturbation event from a background dry state. Return rate following a perturbation can be taken as a direct measure of resilience (Pimm, 1984; Lees *et al.*, 2021), with higher decay rates associated with more resilient systems. Usually this approach considers detrimental perturbations, instead we consider how vegetation responds to the beneficial perturbation of rainfall, yet we retain the definition that faster recovery to the background dry state equates to greater resilience (see *Discussion*). The average annual cycle of Offset50 and NDVI were taken with a monthly resolution. In order to fit an exponential model to these time series, the natural log of the average annual cycle is taken, followed by a linear regression, an example is shown in Figure 4.4. This was used to determine the rate of decay for the system from its peak greenness, for NDVI, or peak connectedness, for Offset50, to the state of minimum vegetation in the dry season.

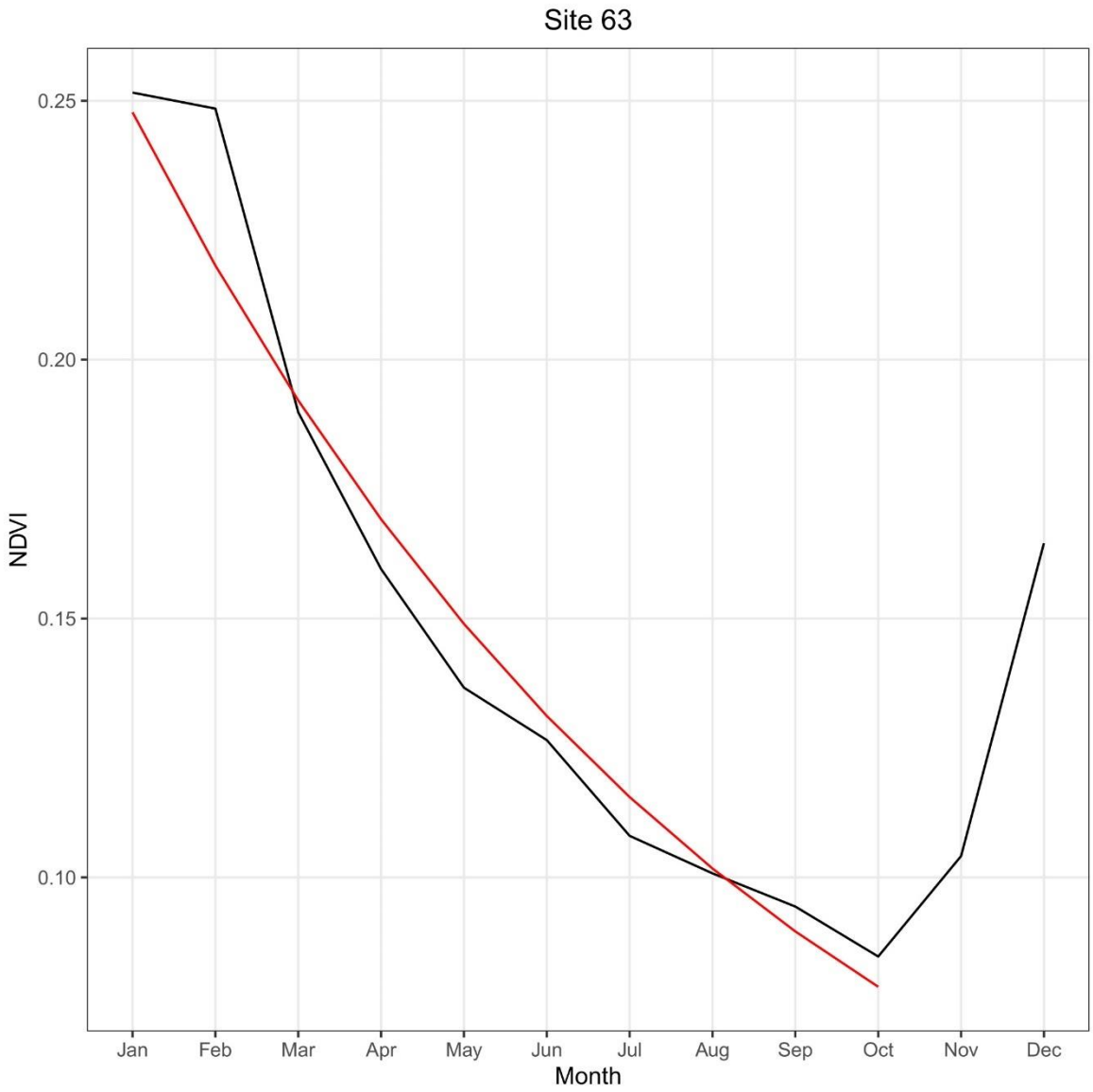

Figure 4.4: Example of exponential decay curve (red line) fitting for annual average NDVI cycle (black line) at site 63.

4.3.5 Resilience - Autocorrelation and variance

Another way to test the resilience of patterned vegetation is to calculate the well-established resilience metrics lag-1 autocorrelation (AR(1)) and variance, of Offset50 and NDVI. Prior to this we remove the seasonality of the Offset50 and NDVI time series by

calculating a multi-annual monthly average, this is then subtracted from the time series. These residuals are then smoothed by applying LOESS smoothing.

Usually when calculating AR(1) we would use a moving window of length equal to half of the time series (Boulton, Allison and Lenton, 2014). However, due to the shortness of these time series (48 data points), the average AR(1) and variance of the whole time series were calculated. This provides us with a single AR(1) and variance value for each time series.

4.3.6 Trend analysis

STL-decomposition of NDVI and Offset50 time series is used in order to establish the trends for each site. This separates these time series into the corresponding trend and seasonality of the underlying data. We then calculate the Mann-Kendall Tau value of this trend component. This gives a positive value if a trend is increasing, a negative value if a trend is decreasing and we classify non-significant changes as 'no trend'. We also calculate the precipitation trend of each site in this way. In addition to this we calculate the change in precipitation in every pixel across the whole of the Sahel. This is done by taking monthly precipitation averages, removing the seasonal trend by subtracting a multi-annual monthly average, then taking a 12-month moving average, before the Kendall Tau of each pixel is calculated.

4.4 Results

4.4.1 Distinguishing patterns with 'Offset50'

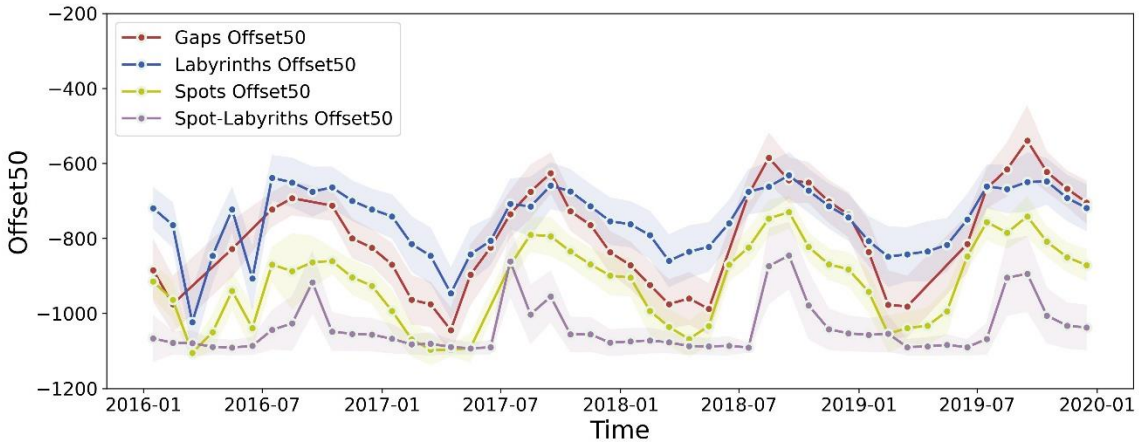

Figure 4.5: Examples of time series of Offset50 metric across four sites. An example is provided for each type of pattern. These sites correspond to the pattern type examples given in Figure 4.1. Offset50 standard deviation is given for each time series.

As seen in Figure 4.5, the Offset50 value of a site displays a seasonal cycle and tracks the changes in vegetation connectivity. The Offset50 value is different for each pattern type; for the examples shown, spot-labyrinths display the lowest Offset50 values, followed by spots, whilst the most connected vegetation patterns, gaps or labyrinths, display the highest Ofset50 values.

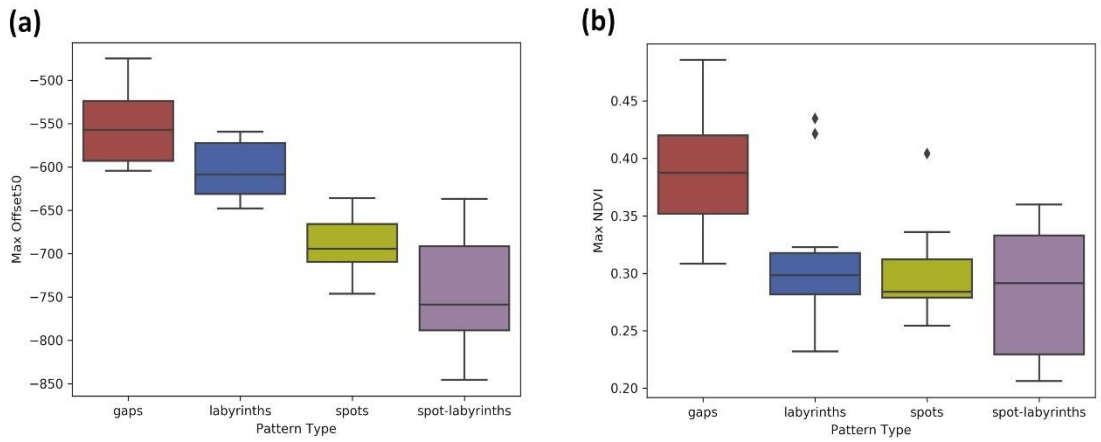

Figure 4.6: (a) Box plots of Max Offset50 values for pattern vegetation sites as grouped by pattern classification. Two tailed Mann-Whitney U-tests suggest that the Max Offset50 value for these group classes are statistically significantly different from each other (p-values in Table B.2). ***(b)*** *Box plots of Max NDVI values for pattern vegetation sites as grouped by pattern classification. Use of a Mann-Whiteny U-test suggests that while the gaps class may be distinct from the other groups, there is no statistically significant difference between the other classes (Table B.3). Mean Offset50 and Mean NDVI are shown in Figure B.5.*

We have chosen to compare the Max NDVI and Max Offset50 values of the vegetation as this represents the extent of the vegetation following a precipitation event when the vegetation is at its full extent, is most connected, and most representative of the pattern label assigned at the classification stage (as detailed in the methodology). When comparing the Max Offset50 value as grouped by vegetation pattern, as in Figure 4.6, we can see that they are broadly distinct classes; there is some overlap between gaps and labyrinths, although gaps display broadly larger values. We also find that despite the visual similarities between 'spot-labyrinths' and conventional labyrinths and spots, they exist as a distinct class. Max NDVI values for each pattern type are also given. U-tests suggest that the max

Offset50 of each pattern for these sample sites is statistically significantly different to each other ($p < 0.05$; Table B.2). When using U-tests to distinguish between the pattern classes for Max NDVI values, we find that while the gaps vegetation is distinct, the rest of the vegetation classes are not statistically significantly distinct (Table B.3). When compared with the Max NDVI of a site over the same time period, we can see that Max Offset50 does a better job of differentiating between the different patterns.

4.4.2 Seasonal and interannual variability of Offset50

As can be seen in Figure 4.7, the timing of the peak of Offset50 is closely linked with the peak of the annual precipitation cycle, with this peak occurring either within the same or following month of the precipitation peak. The Offset50 signal then decays away following the end of the rainy season. At the peak Offset50 value '(i)' in Figure 4.7, there is much more vegetation cover than during the dry season '(ii)'.

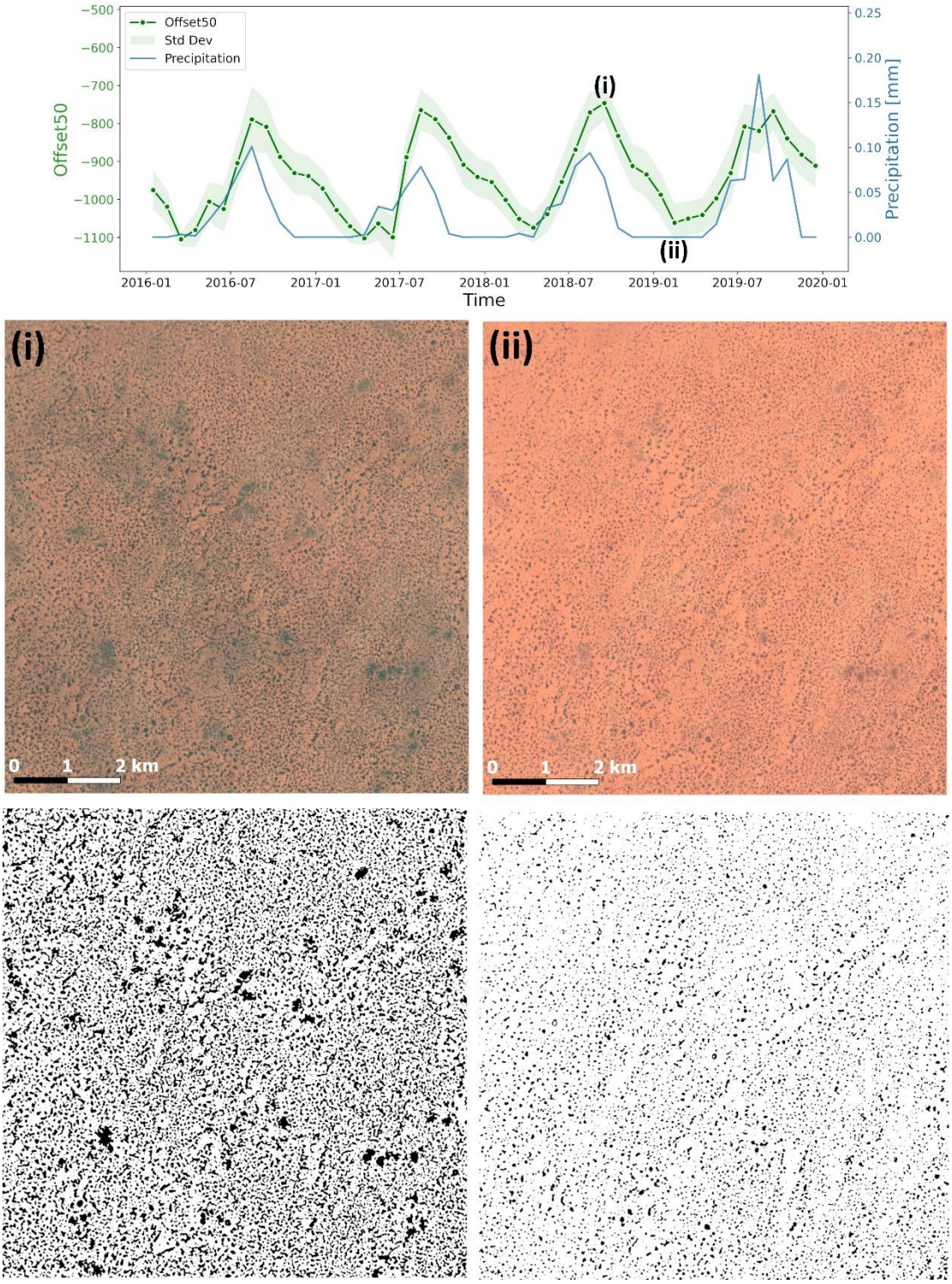

Figure 4.7: Example of Offset50 seasonal variability in a spotted vegetation site (ID: 61) with (i) an image of the vegetation at its 2018 peak and (ii) the following Offset50 minimum in March 2019. Shown below (i) and (ii) are the binary images used to calculate the Offset50

value for that month. In these binary images, black pixels are vegetation, while white pixels are bare soil.

The vegetation shown in Figure 4.8 is classified as 'spot-labyrinths'. This vegetation forms a pattern which resembles faint, degraded spots in drier years, while in wetter periods it forms interlinked stripes across the landscape. The morphology of these patterns appears to be topographically driven, with vegetation forming within shallow gullies and between sand dunes following a rainy season. These patterns display strong interannual variability. It is clear that if there is not sufficient rain within a season, then much of the vegetation will not grow.

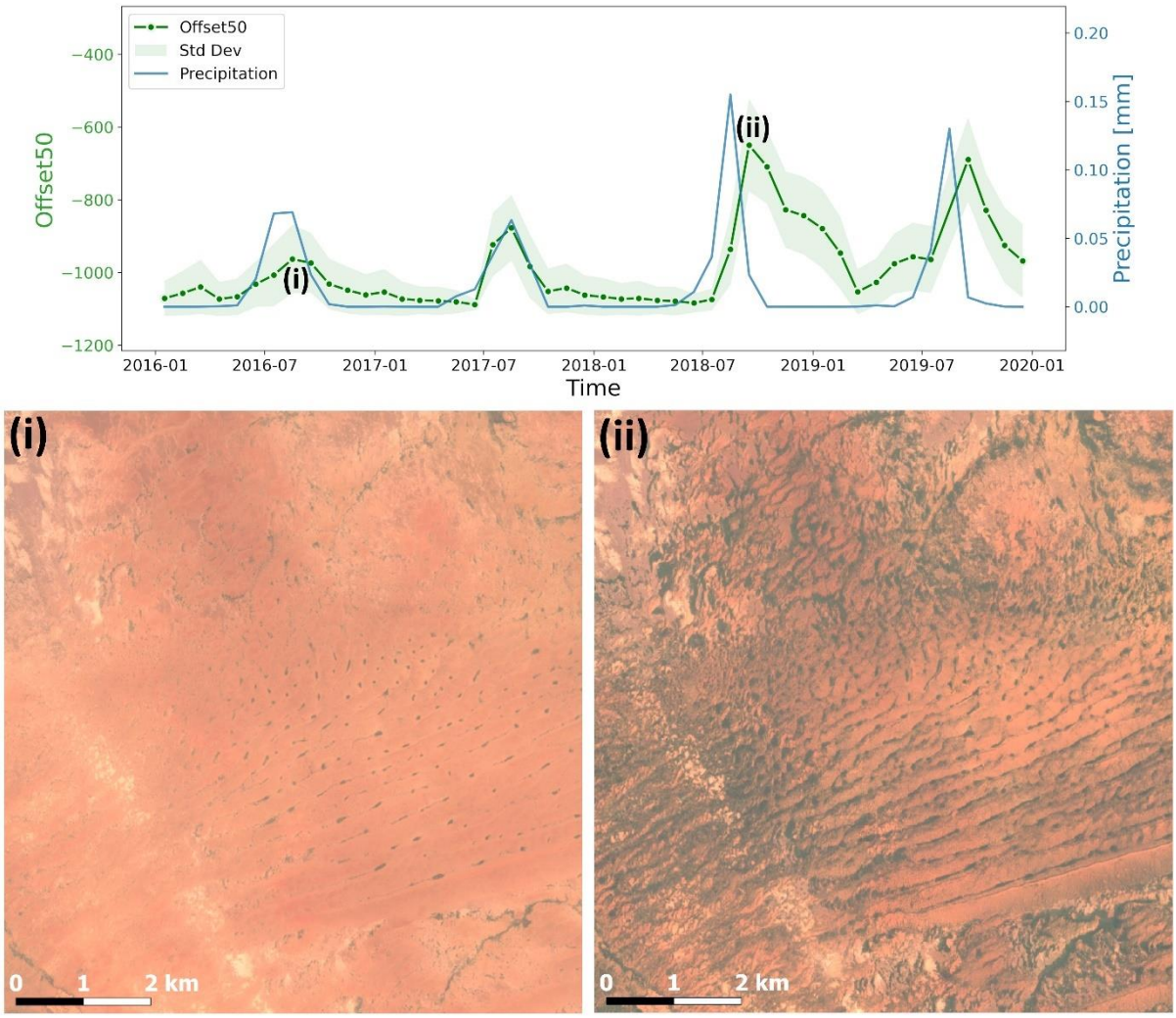

Figure 4.8: An example of interannual variability of spot-labyrinth vegetation (ID 26). This displays the extreme variation in this vegetation with (i) an example of peak vegetation cover in a dry year and (ii) an example of peak vegetation cover in a comparatively wet year. The formation of this vegetation as influenced by the topography, as detailed in Figure B.3.

4.4.3 Factors determining Offset50 and vegetation pattern resilience

Figure 4.9 displays the correlation values for important variables which measure vegetation connectedness (Offset50), abiotic influences (precipitation, latitude), and measures of resilience of vegetation (decay rates, AR(1), variance). We have used these to further

understand the dynamics and resilience of the vegetation pattern system as well as the utility of our Offset50 metric.

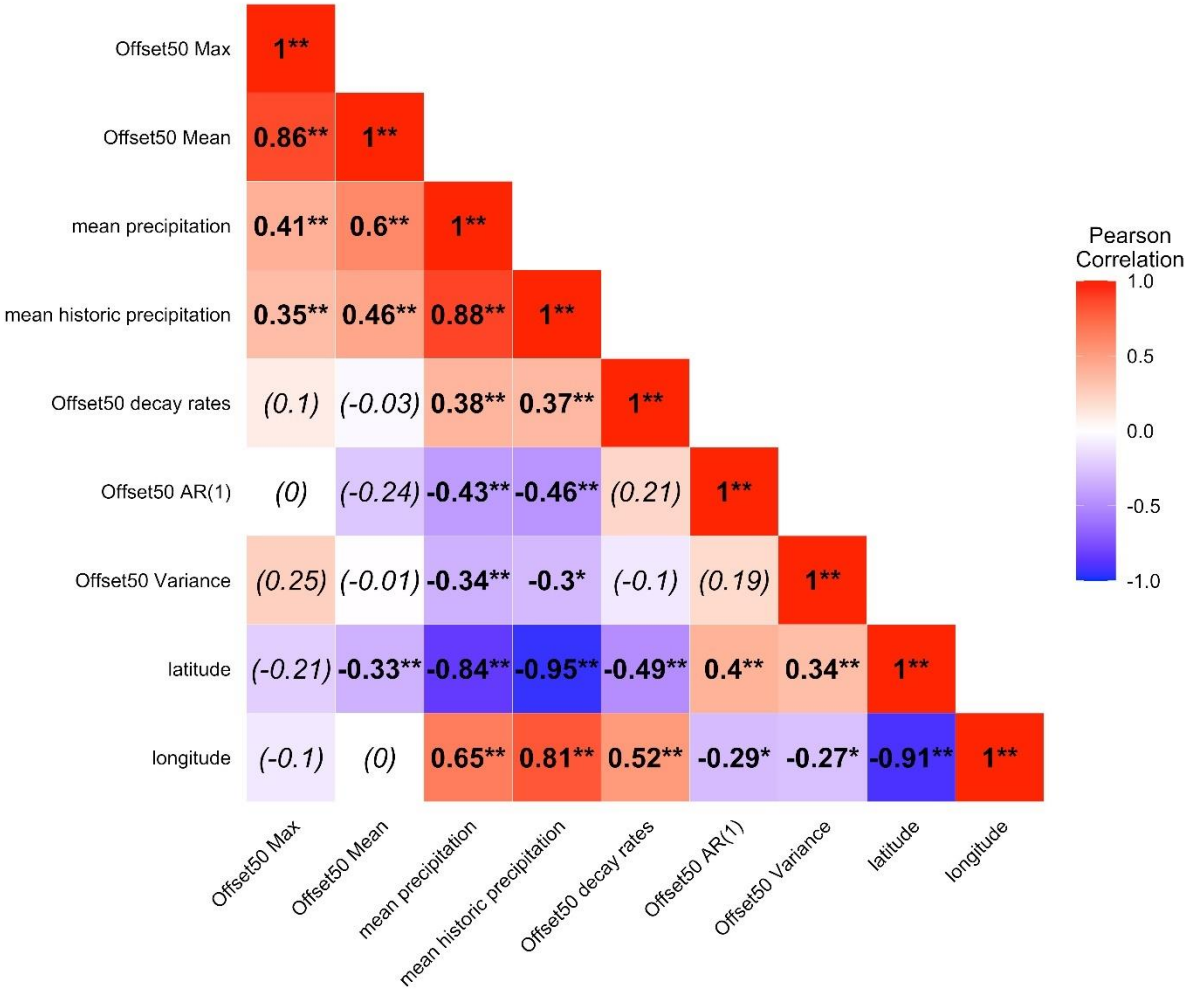

*Figure 4.9: Correlation image showing Pearson's correlation values for Offset50-precip correlation, Offset50 decay rate correlations, and AR(1) and Variance correlations. Values in bold are significant, with ** corresponding to p<0.05 and * corresponding to p<0.1. Scatter plots are given in Figures B.6-B.13. Pearson's correlation coefficient and p-values for Offset50 and NDVI variables are given in Tables B.4-B.7.*

4.4.3.1 Precipitation and Offset50

As seen in Figure 4.9, Offset50 max displays a significant moderate positive correlation with mean precipitation, while Offset50 mean has a strong positive correlation with precipitation. This means that 'gap' sites are the wettest, while 'spot-labyrinth' sites are the driest. Thus, precipitation levels contribute to pattern morphology, as measured by Offset50.

The historic precipitation mean from 1976-2016 is included in order to understand whether historic climate has influenced the current pattern morphology or its resilience. We find that while historic rainfall means do correlate with the Offset50 metric, these correlations are less strong than current precipitation levels, noting also the strong link between historical and current precipitation levels.

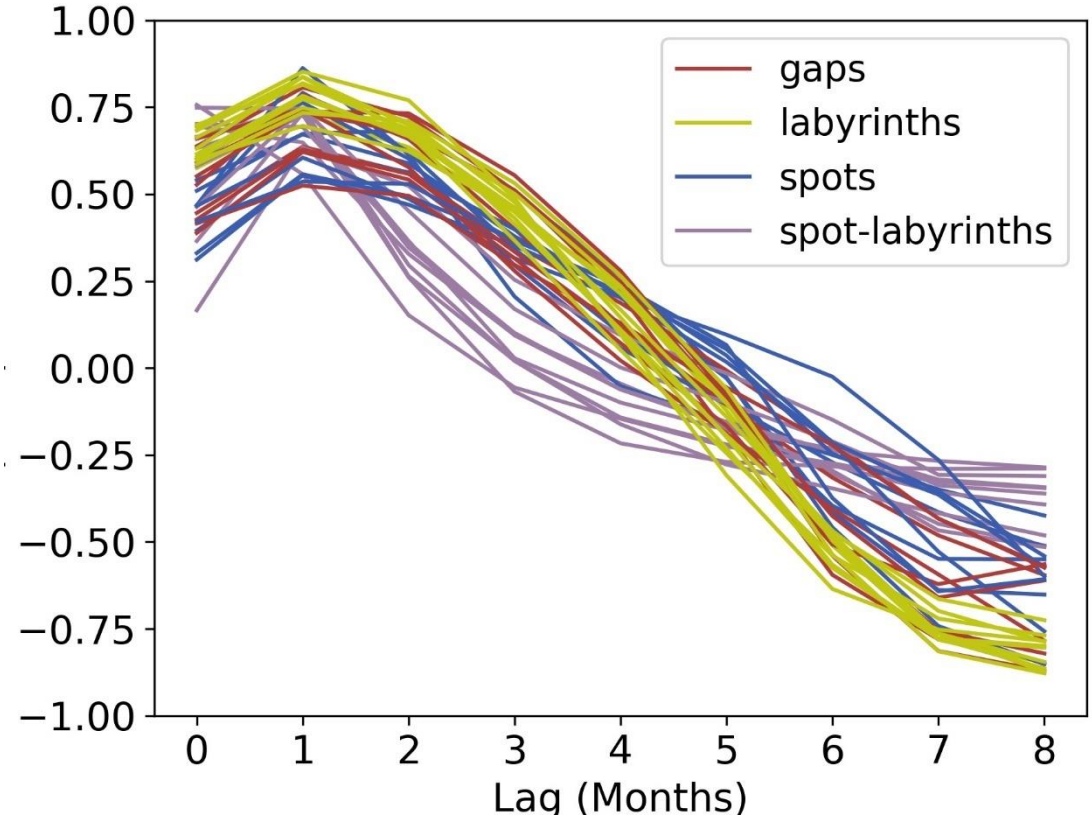

Figure 4.10: Correlation between Offset50 and precipitation at increasing monthly lags across all sites. Each line represents one of the sites in this study.

As can be seen in Figure 4.10, there is a lagged relationship between precipitation and the Offset50 metric across all of the sites. With a close coupling between precipitation and vegetation, these sites experience one significant rainy season per year, after which the vegetation reaches its maximum extent, and therefore so does the Offset50.

There are two trends apparent in this plot, with most sites experiencing the highest correlation between Offset50 and precipitation after 1 month. A clustering analysis of these trends reveals that there are two separate groupings (as seen in Figure B.14), with one group composed almost entirely of all of the spot-labyrinth sites. These sites display a faster

decline in the correlation between Offset50 and precipitation following their initial peak. We propose that this is due to the morphological nature of these patterns, in addition to needing to have a certain threshold of rainfall to enable large scale vegetation growth.

4.4.3.2 Resilience

As seen in Figure 4.9, the Offset50 decay rate has a significant moderately positive correlation with the average precipitation. Therefore, areas with higher rainfall are (by convention) more 'resilient' following this perturbation. This is perhaps a surprising result, as it suggests that areas with a higher level of precipitation experience a faster decay from the peak vegetation state to the minimum vegetation state and that this base state is more resilient. Importantly, Offset50 decay rate does not show a significant correlation to either maximum or mean Offset50 values, thus suggesting that pattern morphology does not correlate with a decay rate measure of resilience (and this null result would, of course, still hold if we inverted our assumed relationship between decay rate and resilience).

When we consider the NDVI decay rate (Table B.6), we find it is greater at wetter sites. We also find a strong positive correlation between average NDVI and NDVI decay rate. Therefore, wetter sites with higher NDVI levels have a higher decay rate from maximum greenness to the bare soil state.

For our other metrics of resilience of vegetation patterns, AR(1) and variance of Offset50, there are significant, moderate negative correlations with mean precipitation (Figure 4.9). Thus, wetter sites have a higher level of resilience of vegetation patterns by these metrics. However, we find that there is no significant correlation between mean or max Offset50 and AR(1) or variance of Offset50. This fails to support the hypothesis from the literature that the morphology of a pattern affects its resilience.

There are also significant weak positive correlations between AR(1) or variance of Offset50 and latitude. This supports an observation in the literature that more northern sites are less resilient (Trichon et al., 2018). This is likely driven by the lower level of precipitation at higher latitudes.

There is a weak negative correlation (which tends towards significance, $p<0.1$) between AR(1) or variance and longitude (Figure 4.9) - i.e. resilience increases with longitude. This is likely linked to a strong positive correlation between longitude and precipitation (Figure 4.9).

4.4.4 Offset50 and precipitation trends across sites

We now turn to trends in the absolute values of precipitation and Offset50 across sites (Figure 4.11).

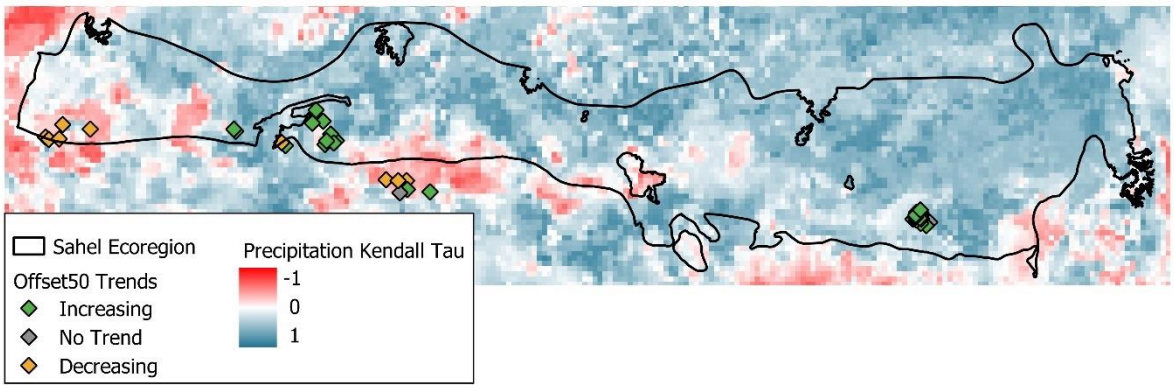

Figure 4.11: ERA5 Precipitation trends from 2016-2019 in the vicinity of the Sahel ecoregion. Also shown are the Offset50 trends of each patterned vegetation site. NDVI trends are given in Figures B.15 and B.16.

Western sites, such as those in Senegal, display a negative trend of Offset50, while those in Mali are much more mixed. Eastern sites all show a positive or no Offset50 trend. Sites with positive Offset50 trends are broadly clustered in areas with a positive precipitation trend, while negative Offset50 trends are clustered in areas where there has been a declining level of precipitation from 2016-2019. This makes sense given the established positive correlation between Offset50 and rainfall (Figure 4.9).

4.5 Discussion

4.5.1 Utility of Offset50 metric and relationship with precipitation

This study provides a framework for vegetation pattern quantification and long term analysis of these sites within the Sahel. The *pyveg* package (Barlow *et al.*, 2020) allows for long-term analysis of patterned vegetation sites, which often occur in hard to reach places around the world. By building on the work presented in Mander *et al.* (2017) we use Offset50, a numerical metric, to quantify vegetation patterns using freely available satellite data. Previous studies have sought to visually assess vegetation pattern health using infrequent aerial photography (Couteron, 2002; Trichon *et al.*, 2018), these are often limited in extent both spatially and temporally. Sentinel-2 data, with its 10m resolution, when combined with the *pyveg* package, provide a way to repeatedly analyse pattern vegetation anywhere in the world and to generate time series of its state. We find that our Offset50 metric is more capable than NDVI of differentiating between four pattern vegetation classes at their maximum extent; gaps, labyrinths, spots and spot-labyrinths. This allows us to quantify inter- and intra-annual changes in vegetation pattern morphology.

Precipitation levels have often been identified as the predominant factor in patterned vegetation formation and morphology (HilleRisLambers *et al.*, 2001). The correlation between Offset50 values and average precipitation levels at our sites shows that our Offset50 metric successfully captures this relationship. We have also considered the lagged correlation between Offset50 and precipitation, which for most sites peaks after 1 month and then declines. The difference between spot-labyrinths and other vegetation types is clear in the lagged correlation trend. This further reveals the different mechanisms of

formation of the vegetation morphologies, with the lagged correlation decreasing faster for the spot-labyrinth sites. This is likely to be the result of vegetation formation from the collection of rainfall within gullies and between sand dunes, within which the vegetation then grows. If this precipitation stays below a certain threshold then the vegetation is minimal and unconnected.

4.5.2 Resilience

We have taken two different approaches to measuring the resilience of vegetation patterns by examining different time series properties of the Offset50 metric.

First we considered the decay rate of Offset50 following the annual rainy season. The conventional understanding is that a faster decay rate equates to a more resilient system. Here we conceptualise the stable state as one of low vegetation cover in the dry season and consider the resilience of this state to an annual rainy season which acts as a perturbation to this system. This unconventional approach would suggest that sites with a faster decay rate have a more 'resilient' low vegetation state, or potentially a less resilient wet state. Following this, we find that sites which have higher precipitation display a higher decay rate from the peak vegetation to low vegetation cover and are therefore more 'resilient'. However, this is somewhat counter-intuitive, in that it refers to the resilience of the dry season minimum vegetation cover state to occurrences of rainfall, which is found to be more 'resilient' under higher precipitation levels. We also find the same result when considering the NDVI decay rate. This suggests that, while higher levels of precipitation may lead to a larger burst in vegetation cover, it tends to die off faster. This can also be seen in the positive correlation between average precipitation and NDVI standard deviation

(correlation = 0.4752, p=0.0019), with wetter sites showing greater standard deviation due to the greater quantity of vegetation die off each year.

Second we removed the seasonal cycle and then calculated lag-1 autocorrelation (AR(1)) and variance of the detrended Offset50 time series, both of which are conventional resilience measures. This probes behaviour on shorter timescales than the annual cycle, which is appropriate given the multi-month memory in the system (Figure 4.10). We find that sites which experience higher precipitation levels show lower AR(1) and variance levels and are therefore more resilient according to these metrics. This is in agreement with our understanding of rainfall levels and vegetation morphology, and suggests that vegetation which exists under lower rainfall regimes may be at risk of further degradation or state transitions. This is supported by results found in the literature, which find that drier sites have experienced greater levels of degradation during a drought period and have been less able to recover (Trichon *et al.*, 2018). We consider the relationship between historical precipitation levels and patterned vegetation resilience to understand the effect that past climate may have had on the adaptive capacity of patterned vegetation. While there is some correlation, this is most likely due to the strong correlation between historic and modern precipitation, as opposed to any underlying property of the system.

We also tested the hypothesis that vegetation pattern morphology itself provides a measure of resilience (Rietkerk *et al.*, 2004; Mayor *et al.*, 2013). Dakos *et al.* (2011) suggest that while critical slowing down is observed as pattern morphology shifts in a 'scale dependent feedback' vegetation model, there is no consistent increase in AR(1) with these changes. This is in line with our results, which show that pattern morphology does not significantly correlate with any of the resilience indicators we consider; decay rate, AR(1) or variance.

This suggests that while the nature of vegetation patterning does reflect underlying precipitation, it cannot be linked directly to the resilience of the vegetation, at least across the sample of 40 sites we consider.

There is evidence that severe and prolonged droughts cause a greater reduction in coverage of northern Sahelian patterned vegetation sites (Trichon *et al.*, 2018). This is consistent with our results that patterned vegetation sites at higher latitudes have a lower level of resilience, likely linked to the lower levels of precipitation at higher latitude.

4.5.3 Trends in Offset50

Identification of trends in Offset50 between 2016 and 2019 in sites across the Sahel reveal a mixed picture. No sites with negative trends for Offset50 appear in the east of the Sahel, while these are more common in the west. This is in line with trends in precipitation (Figure 4.11), with declining Offset50 trends situated in areas with declining precipitation trends. Nicholson, Fink and Funk (2018) identifies a difference in rainfall between the east and west, with the eastern precipitation regime showing a greater recovery from historic dry periods. This east-west division is reinforced by the eastern vegetation sites displaying higher resilience levels. However, more data is needed to understand whether this east-west divide in patterned vegetation trends is sustained at the decadal level. A more global analysis could provide an indication of different pattern vegetation resilience and the drivers of this. Aside from climatic factors, other potential causes of declining pattern vegetation cover, and therefore declining Offset50, relate to human activities, such as the collection of forage for livestock, or the conversion of land to agriculture.

4.5.4 Limitations and future work

Interference from cloud cover creates difficulties for most remote sensing studies. In this study we have sought to limit the impact of cloud cover through numerous methods, as detailed in the *Methods*. There are some limitations introduced by the availability of satellite data. Sentinel-2 was launched in 2015, therefore we have been unable to observe multi-decadal trends in the patterned vegetation at the appropriate scale. The time series was also determined to be too short to conduct some forms of time series analysis. To counter this, attempts were made to use data from Landsat 7 and Landsat 8 to provide longer analysis at lower spatial resolution; however well documented issues with the Landsat 7 scan line error (Storey, Scaramuzza and Schmidt, 2005) prevented this.

In addition to this, attempts were made to source vegetation patterning from a diverse range of sites across the Sahel. This was successful for every form apart from spots, where difficulty with establishing degraded spot sites meant the removal of several sites from the dataset. This meant that all of the sites are located within a similar area of Sudan. This was further compounded by inconsistencies in historical literature in spot definition, with gaps and spots often interchangeable terms. Some sites which were identified in historical literature as showing spotted vegetation were limited in size and difficult to analyse or have since become much more degraded.

The creation of the *pyveg* package will allow future work to continue monitoring pattern vegetation morphology and the health of dryland ecosystems. The increasing availability of high resolution Sentinel-2 images will enable longer and more in depth time series analysis. In addition to this, future work could apply the *pyveg* package to global drylands in order to develop a more comprehensive understanding of resilience trends in these regions.

Based upon the lack of relationship between pattern morphology and resilience, we suggest that further work is required to define and measure resilience of these patterned systems. With an increased availability of sufficiently high resolution satellite data, we believe that other resilience tools should be brought to bear on these systems, with consideration given to spatial resilience statistics as well as temporal analysis.

4.6 Conclusion

Dryland ecosystems are among the most sensitive to climate change. Accurately assessing and understanding vegetation patterning morphology is an important step towards understanding the effect of a changing climate and direct anthropogenic pressure on drylands. Here we have shown that a previously proposed feature vector Offset50 metric detects changes in pattern vegetation morphology and is sensitive to changes in precipitation, the underlying driver of pattern vegetation. We find that three different measures of resilience - the decay rate from perturbation, AR(1) and variance of Offset50 - all show declining resilience of vegetation patterns with declining rainfall (as do the same statistics for NDVI). However, we find no significant correlation between the Offset50 pattern metric and any of these three measures of resilience. This fails to support a widely cited hypothesis in the literature that the nature of vegetation pattern (quantified here) reflects resilience. This negative result should not be wholly surprising, as we are unaware of any theoretical demonstration that there should be a direct relationship between regular pattern morphology and resilience. We also find that geographical gradients of patterned vegetation resilience reflect well known rainfall gradients, and that recent trends in rainfall are largely reflected in corresponding trends in vegetation patterns. Notably, consistent recent wetting of eastern sites is reflected in positive trends in Offset50, while the picture for the west is more mixed. As a longer timescale sample of high resolution satellite data accumulates, this should enable further enhanced understanding of the resilience of these special ecosystems.

Chapter 5: Global relationship of vegetation resilience with precipitation

5.1 Abstract

Across much of the world, vegetation is being affected by climate change, but how does climate affect the resilience of different ecosystems? A generic measure of resilience is the recovery rate from perturbations, which theory suggests is inversely related to lag-1 temporal autocorrelation (AR(1)). Here we assess how vegetation resilience depends on climate by analysing remotely-sensed vegetation greenness (MODIS NDVI) and optical depth (VODCA) data. We show that for NDVI, vegetation resilience is strongly correlated with precipitation levels across three spatial scales; local (pixel), ecoregion and biome. Vegetation resilience declines markedly below 2000mm of precipitation per year. Additionally, higher temperatures tend to lead to lower resilience, especially when associated with low precipitation. A similar, but less clear, relationship is observed between VOD resilience and precipitation. Our results support suggestions that regions subject to drying due to climate change will lose vegetation resilience. Here we show the opportunity for global resilience analysis with increased data availability and computational resources.

5.2 Introduction

Vegetation in many ecosystems around the world is at risk from interlinked pressures such as rising temperature, drought and pests (McDowell *et al.*, 2011). We take 'resilience' to mean the capacity of a system to recover from perturbations, measured as its recovery rate, which theory suggests is inversely related to lag-1 temporal autocorrelation (AR(1)). This has recently been validated with remotely sensed data in Smith, Traxl and Boers (*in press*). Less resilient vegetation is more affected by a given perturbation and responds slower, when compared to the effect the same perturbation would have on more resilient vegetation. For those ecosystems that display bistability (Hirota *et al.*, 2011; Staver, Archibald and Levin, 2011; Abis and Brovkin, 2017; Wuyts, Champneys and House, 2017), loss of resilience is expected before they reach a tipping point to an alternative state. These early warning signals of loss of vegetation resilience have been detected using remotely sensed data prior to localised forest dieback events (Liu *et al.*, 2019) and over the much larger spatial scale of the Amazon (Boulton, Lenton and Boers, 2022). Such analysis can be limited by the availability of climatic and vegetation data over a sufficient time scale to detect changes in resilience, particularly for intrinsically 'slow' vegetation systems. Instead, space-for-time substitutions can be utilised to assess how vegetation resilience changes with environmental conditions (Verbesselt *et al.*, 2016). Existing application to tropical forests shows that areas with lower precipitation levels display lower resilience, with a notable loss of resilience (increase in AR(1)) below a precipitation threshold of ~2000mm year^{-1}. Here we apply this approach globally to see if there is a general relationship between climate drivers and vegetation resilience.

We analyse the average lag-1 temporal autocorrelation (AR(1)) of fluctuations in vegetation across the world to understand the effect of climatic drivers on resilience. For this, we utilise the Normalised Difference Vegetation Index (NDVI) from MODIS data from 2001-2020, which is used to calculate AR(1) at its native 250m resolution in Google Earth Engine (GEE), then aggregated to 2.5km for offline analysis. We also conduct the same analysis using Vegetation Optical Depth data (VODCA) from 1991-2016, at 0.25°x0.25° resolution, for comparison. Seasonality and any trend in the data are first removed (see *Methods*), before using the NDVI residuals to calculate the mean NDVI AR(1) and compare this with mean precipitation and temperature data, as well as mean Dry Season Length (DSL) and percentage tree cover. This analysis considers these relationships across the world at three different scales; the local (pixel), ecoregion and biome levels.

5.3 Methods

5.3.1 Data

In this study we use NDVI data from the MODIS satellites for the period of January 2001 to December 2020. The initial stages of data analysis are undertaken in GEE which allows for large scale computational processes (Gorelick *et al.*, 2017) and enables us to build upon the work of Verbesselt et al. (2016) at a global scale. The dataset that we utilised is a NDVI dataset which is available on GEE. NDVI is a commonly used remote sensing metric which measures the greenness of vegetation, i.e. the photosynthetic activity of plants. It is used as a proxy of vegetation productivity (Pettorelli et al., 2005) and relates to plant biomass (Zhu and Liu, 2015) and leaf area index (Carlson and Ripley, 1997; Tian et al., 2017; Waring, 1983). Due to the link between NDVI and vegetation health, it has been used in other vegetation resilience studies (De Keersmaecker *et al.*, 2014, 2015; Verbesselt *et al.*, 2016; Liu *et al.*, 2019; Feng *et al.*, 2021). Although it is worth noting that NDVI does have some limitations, with issues concerning oversaturation in high biomass regions and soil reflectance in areas with little vegetation (Huete, Liu and van Leeuwen, 1997).

To address any potential limitations in NDVI, data is also used from the ku-band of the Vegetation Optical Depth Climate Archive (VODCA), which has a spatial resolution of 0.25°x0.25° and a temporal resolution of 1 month (Moesinger *et al.*, 2020). The VODCA data used covers the period from January 1991 to December 2016. VODCA responds to moisture content in the canopy and may be a better proxy for changes in biomass than NDVI in tropical forest settings (Boulton, Lenton and Boers, 2022), but potentially has issues from biased data in high latitudes for certain years (Moesinger *et al.*, 2020). Due to differences in

resolution, comparisons between VODCA and NDVI data are made at the ecoregion level, rather than the pixel level.

Precipitation and surface temperature datasets were used from the ERA5-Land reanalysis dataset with post processing from ECMWF (Hersbach *et al.*, 2020). This was accessed via GEE. We use the precipitation data to define our average dry season length (DSL) as the average number of months in a year that the precipitation value falls below 100mm in keeping with Boulton, Booth and Good (2017). We also consider the average percentage tree cover in 2000 using data from Hansen *et al.* (2013).

5.3.2 Methodology

To conduct our global analysis, we calculate the NDVI AR(1) values using the cloud computational capabilities of GEE. This enables us to calculate the AR(1) for each individual pixel, rather than having to spatially aggregate data prior to analysis. It also allows a global overview which can then be easily reapplied to specific areas of interest. We calculate this resilience metric without the impact of seasonality and any confounding trends as these can influence AR(1) in ways unrelated to response to short-term perturbations.

We begin by aggregating the NDVI data at a monthly level, this reduces the likelihood of missing data due to cloud cover. Then we calculate a multi-annual monthly average value, i.e. an average January across all 20 years. To remove the average seasonal cycle we subtract the multi-annual monthly average from our monthly average time series. Following this, we subtract a 25 month moving average from the decycled time series. This then leaves us with a series of residuals which have had the seasonal cycle removed and have been smoothed. Finally, we calculate the AR(1) of this residual time series using a moving window

which is equal to half the length of the time series. This method is applied globally to every pixel with the use of GEE. The VODCA AR(1) is also calculated in this way for consistency, however where VODCA data is missing, this is infilled using linear interpolation at the decycling stage, but this infilled data is then removed when the residuals are calculated, so should not overly influence the AR(1) values.

The 250m NDVI AR(1) data is then exported from GEE with a coarser resolution of 2.5km for further analysis. Spatial averages are used to reduce the image resolution. We then utilise QGIS, Matlab and R to analyse the resilience relationship at a global, ecoregion and local scale. Pixels with low average NDVI corresponding to ice, cloud and soil, are removed from the analysis. The threshold for this is 0.16, with pixels below this removed. This value was chosen by considering the distribution of mean NDVI pixels and identifying 0.16 as the minima between the peaks corresponding to no vegetation and low vegetation. The same method is used for VOD data, with a threshold of 0.25 identified. This data is divided according to the Ecoregions2017 map (Dinerstein *et al.*, 2017). These 846 ecoregions are contiguous regions which are defined according to local climatic values and vegetation types, with ecoregions then grouped into 1 of 14 larger biomes. Ecoregions are removed from our ecoregion level analysis if more than 50% of their constituent pixels consist of low-NDVI pixels (corresponding to no or very low vegetation); this leaves us with 715 ecoregions. We then compare the average AR(1) against climatic data at the biome, ecoregion and pixel scale.

5.3.3 Comparing decycling methods

To properly isolate and analyse changes in resilience in this study we have removed the seasonal cycle from the data prior to calculating the AR(1) using a relatively simple method,

as detailed above. This method is necessary due to the limited functionality of the Javascript coding language required to use GEE and is similar to other methods found in the literature (De Keersmaecker *et al.*, 2015). We compare the utility of this relatively simple approach with a more complex STL decomposition on 100 random points (4 of which are removed as they are located in regions with no data). This STL decomposition utilises a periodic seasonal window. The mean AR(1) of each pixel is consistent across each method, but our initial approach produces larger mean AR(1) values, as shown in Figure 5.1. We also find similarities in the AR(1) time series for each method. The focus of this study is to compare the AR(1) between points, rather than the absolute value of AR(1) at each point. As such, the decycling method which has been applied here seems valid for this purpose.

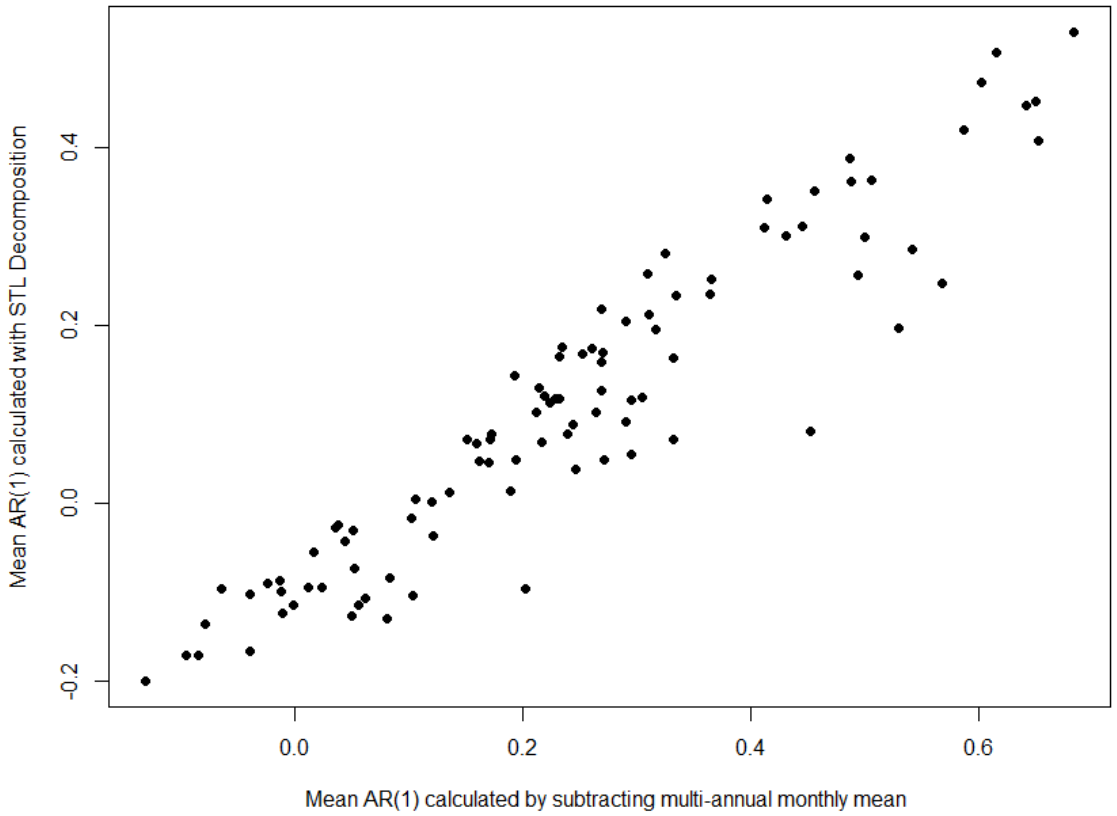

Figure 5.1: Scatter plot of mean AR(1) values from time series which have been calculated by our initial method and by an STL decomposition. Spearman's rho = 0.94, p<2.2e-16.

5.4 Results

5.4.1 Spatial distribution of resilience

Mean ecoregion-scale AR(1) values across the globe (Figure 5.2) clearly show arid and semi-arid regions generally have highest mean AR(1) values (suggesting lowest resilience), including the Mediterranean, Australia, southwestern North America and southern Africa. Some equatorial tropical rainforest regions have the lowest AR(1) values (corresponding to the highest resilience). However, higher latitude ecoregions also display low AR(1) values. This could represent the impact of snow cover in these regions, which may introduce noise into the data and will buffer changes in NDVI (De Keersmaecker *et al.*, 2015). There are also contrasting trends in this region, with both greening and browning observed due to a changing climate (Myers-Smith *et al.*, 2020). Negative AR(1) values should also be noted as potentially erroneous, as these are likely to be a product of the noise in the data in densely forested regions with greater cloud cover, poor fit of our detrending model or the slow response time of this dense vegetation.

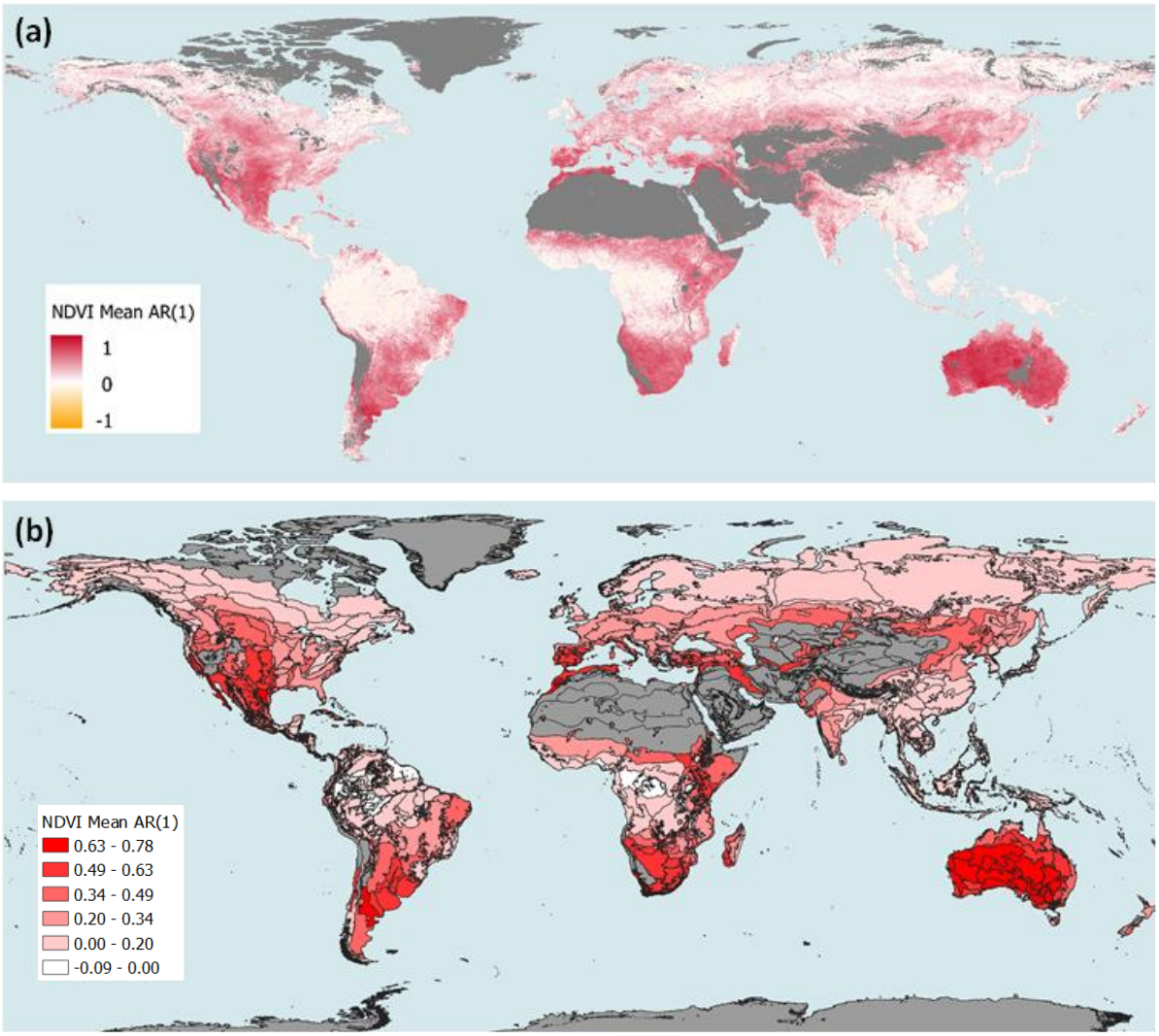

Figure 5.2: A map of mean NDVI AR(1) values at (a) the pixel level and (b) as averaged by ecoregion. Darker regions correspond to higher AR(1) and therefore lower resilience levels. Grey pixels in (a) have low vegetation cover (NDVI <0.16), while grey ecoregions in (b) have been removed due to >50% of their pixels filtered out because of low NDVI levels.

5.4.2 Precipitation and resilience

The relationship between mean NDVI AR(1) and precipitation at the pixel level, then aggregated to the ecoregion and biome levels shows a consistent pattern (Figure 5.3). AR(1) generally increases (therefore resilience declines) below precipitation levels of ~2000 mm

year^{-1}. As this relationship is nonlinear, we consider the Spearman's rho to compare variables.

At the pixel level, low AR(1) values of ~0.1 (high resilience) occurs for precipitation >2000 mm year^{-1}. AR(1) increases (resilience decreases), approximately linearly, with decreasing precipitation levels <2000 mm year^{-1}. There is a moderate to strong negative correlation (rho=-0.39, p<2.2e-16) between AR(1) and precipitation. The relationship is consistent with previous findings for tropical forests (Verbesselt *et al.*, 2016) which identifies a threshold of ~1500-2000 mm year^{-1} below which there is resilience loss.

Aggregating to the ecoregion scale, the same nonlinear threshold relationship is apparent, with drier ecoregions displaying lower resilience (correlation=-0.77, p<2.2e-16). There are some outliers, some of which are Arctic or boreal ecoregions which is evident from the map in Figure 5.2.

When we consider the biome scale, the wettest biomes, Mangroves and Tropical Moist Broadleaf Forests, have a mean annual precipitation ~2250 mm year^{-1}; below this there is an approximately linear relationship of AR(1) to precipitation. Two high latitude biomes, Tundra and Boreal Forest/Taiga, represent clear outliers, and may suggest other drivers of ecosystem resilience which we proceed to investigate.

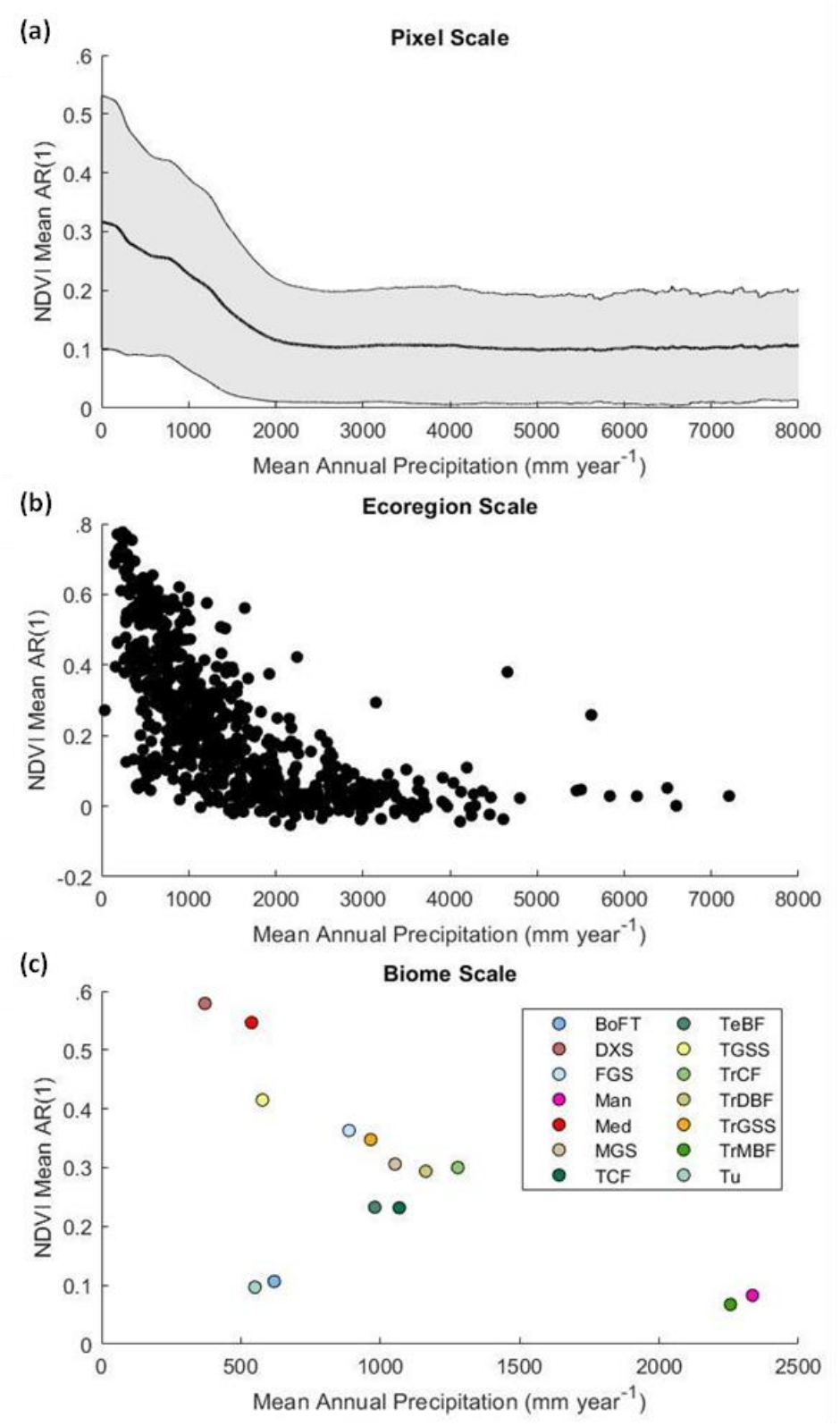

Figure 5.3: Mean AR(1) compared with mean annual precipitation at (a) pixel scale (rho = -0.39, p<2.2e-16), with a moving average of 1000mm applied, grey area represents standard

deviation, (b) ecoregion scale (rho=-0.77, p<2.2e-16) and (c) biome scale (rho=-0.62, p= 0.02). Biome abbreviations correspond to the following biomes: BoFT – Boreal Forests/Taiga, DXS – Desert and Xeric Shrublands, FGS – Flooded Grasslands and Savannas, Man – Mangroves, Med – Mediterranean Forests, Woodlands and Scrub, MGS - Montane Grasslands and Shrublands, TeBF – Temperate Broadleaf and Mixed Forests, TCF – Temperate Conifer Forests, TGSS – Temperate Grasslands, Savannas and Shrublands, TrCF – Tropical and Subtropical Coniferous Forests, TrDBF - Tropical and Subtropical Dry Broadleaf Forests, TrGSS – Tropical and Subtropical Grasslands, Savannas and Shrublands, TrMBF – Tropical and Subtropical Moist Broadleaf Forests, Tu – Tundra.

5.4.3 Temperature and resilience

The outlier results for tundra and boreal forest showing high resilience despite low precipitation led us to consider whether there is also a temperature control on resilience.

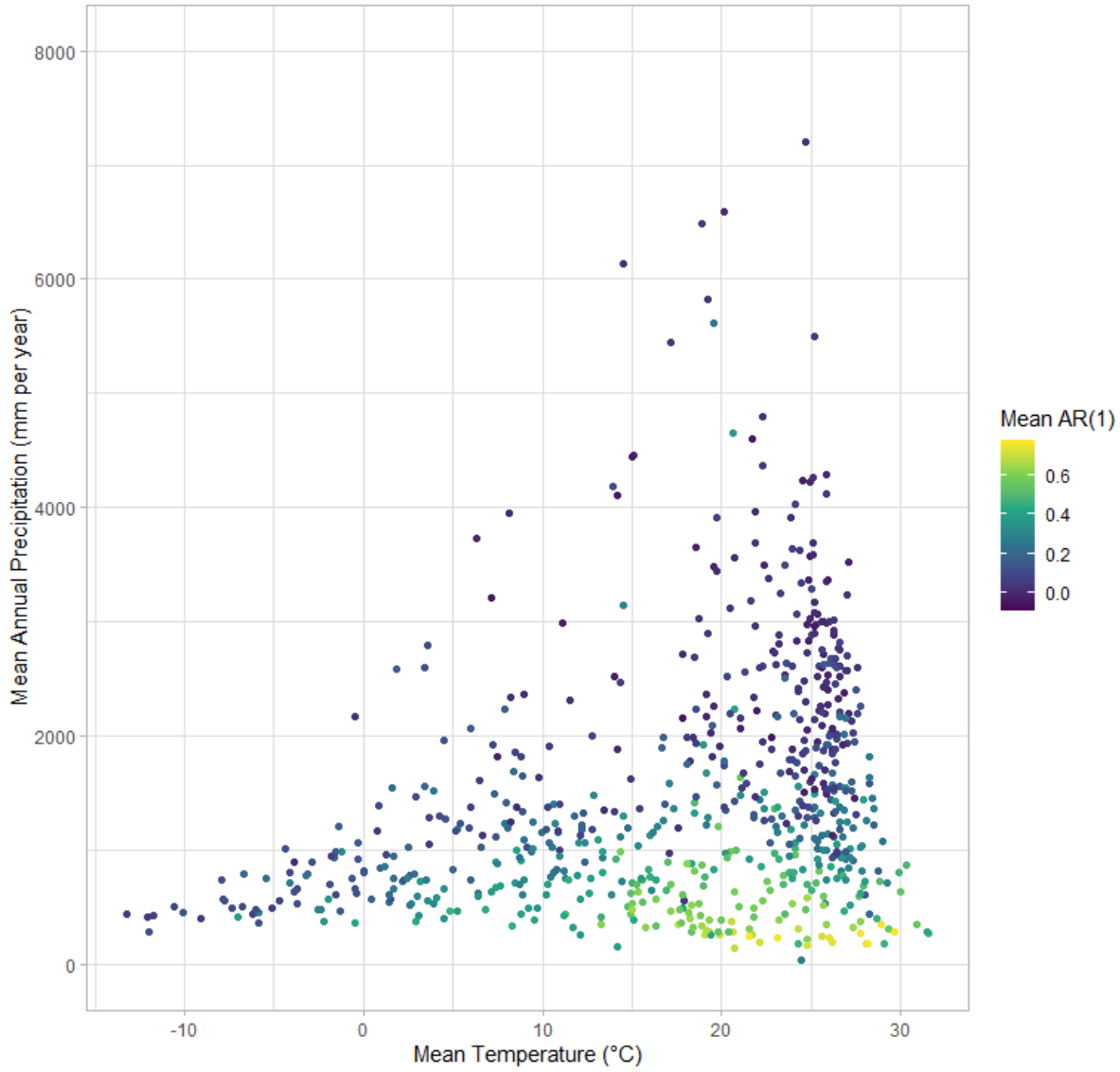

Figure 5.4: Scatter plot of each ecoregion's mean annual precipitation and mean temperature which is coloured according to the mean AR(1).

While there is no statistically significant relationship between mean AR(1) and temperature at the ecoregion scale (correlation: -0.07, p=0.07), when we consider the relationship between these variables and precipitation (Figure 5.4) then there is a trend that appears. Vegetation in ecoregions with higher temperature and low precipitation levels experience the highest AR(1) values and therefore the lowest resilience, while drier, cooler regions display a higher resilience level.

5.4.4 Dry season length and resilience

In addition to temperature and precipitation, we also consider the effect of dry season length on ecosystem resilience. The relationship between mean DSL and temperature for each ecoregion are displayed in Figure 5.5. Here we can see that high AR(1) (low resilience) ecoregions primarily have a large DSL and high temperature. These ecoregions also have low levels of tree cover. There is a visual boundary between forested and non-forested areas within the DSL-temperature space, beyond which the ecosystems display low resilience. This seems to support the findings of Boulton, Booth and Good (2017) which identify such a boundary in models of tropical rainforests.

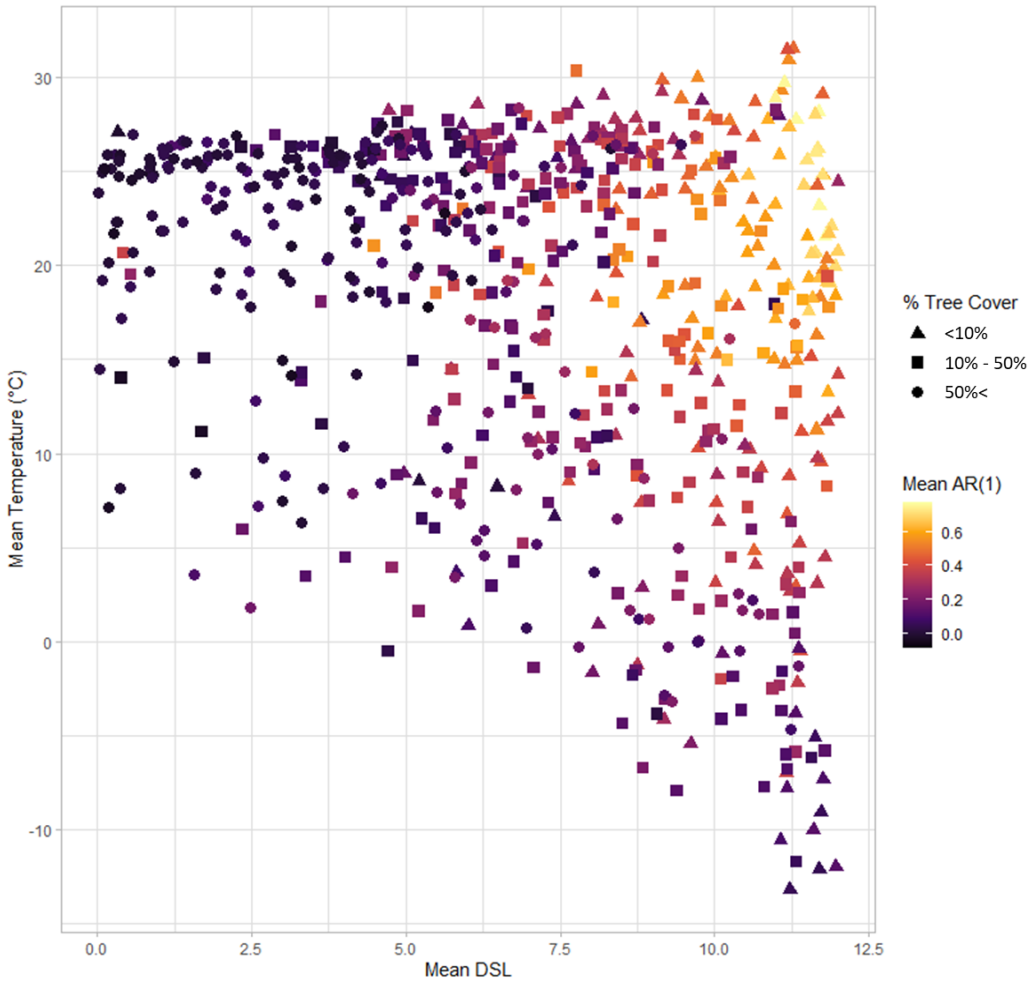

Figure 5.5: Scatter plot of mean temperature and mean dry season length (DSL) at the ecoregion level. Colour is given by mean AR(1) and shape is based upon the average percentage tree cover within each ecoregion.

5.4.5 Linear regression analysis

To investigate the potential role of multiple climate drivers on vegetation resilience we utilise multivariate linear regression models using temperature, precipitation (MAP), dry season length and percentage tree cover. We consider this at the ecoregion scale and the pixel scale, with R^2 values presented in Table 5.1. As some variables, such as precipitation, may not have a linear relationship with NDVI AR(1) (as seen in Figure 5.3), we examined

whether linearity was achieved by taking the logarithm of each variable. We found that precipitation has a long tail distribution, so by taking the logarithm we convert it to a Gaussian distribution, and find that the relationship between NDVI AR(1) and the logarithm of precipitation is linear.

Here we find that the primary predictive variable is precipitation, which accounts for most of the variance within the mean AR(1) values. This suggests that precipitation is the primary driver of vegetation resilience. The inclusion of temperature and tree cover also increases the accuracy of our predictive model, while DSL does not improve it. This is confirmed by the R^2 values below, as well as by using a stepwise regression function, which selects the variables which produce the model with the lowest AIC (Akaike Information Criterion); this indicates the best fit. The regression model relationships are consistent between the ecoregion and pixel scale, although the pixel level models display a lower R^2 value, which is to be expected due to the substantially larger number of data points.

Also considered are the regression models at ecoregion scale which have had high latitudinal ecoregions removed. These ecoregions are classified as part of the Tundra or Boreal Forest biomes, which are noted as outliers in Figure 5.3. We can see that the R^2 values increase for each model when these outliers are removed, with precipitation accounting for 66% of the variation in vegetation resilience.

Table 5.1: R^2 value for NDVI linear regression models.

NDVI Regression model	Pixel scale: R^2 values	Ecoregion scale: R^2 values	Ecoregion scale without Boreal or Tundra ecoregions: R^2 values
AR(1) ~ MAP + Temperature	0.3953	0.4313	0.4546
AR(1) ~ log(MAP)	0.1951	0.5597	0.6615
AR(1)~ Temperature	0.1185	0.0002314	0.0025
AR(1) ~ log(MAP) + Temperature	0.4735	0.6296	0.6718
AR(1)~ Temperature + DSL	0.4515	0.595	0.6414
AR(1) ~ log(MAP) + Temperature + DSL	0.4828	0.6384	0.6833
AR(1) ~ log(MAP) + Temperature + DSL + Tree Cover	0.5285	0.6178	0.7136
AR(1) ~ log(MAP) + Temperature + Tree Cover	0.5252	0.6715	0.7129

We also assess the ability of these climatic variables to predict resilience by comparing the linear regression model predicted values with the original NDVI AR(1) values (Figure 5.6). Here we use the linear regression model with predictor variables log(MAP), temperature

and tree cover. The predicted AR(1) values and the original NDVI AR(1) values are highly correlated (rho= 0.83, p<2.2e-16). However it seems that model predicted AR(1) values are lower. This can be seen in biomes with high AR(1) values, such as the Desert and Xeric Shrubland and Mediterranean Forests, Woodlands and Scrub biomes. These biomes display low levels of resilience on account of the high temperature and lower precipitation. This may suggest that there is a non-linear relationship between temperature and precipitation in regions with high AR(1) which our linear regression models are unable to resolve.

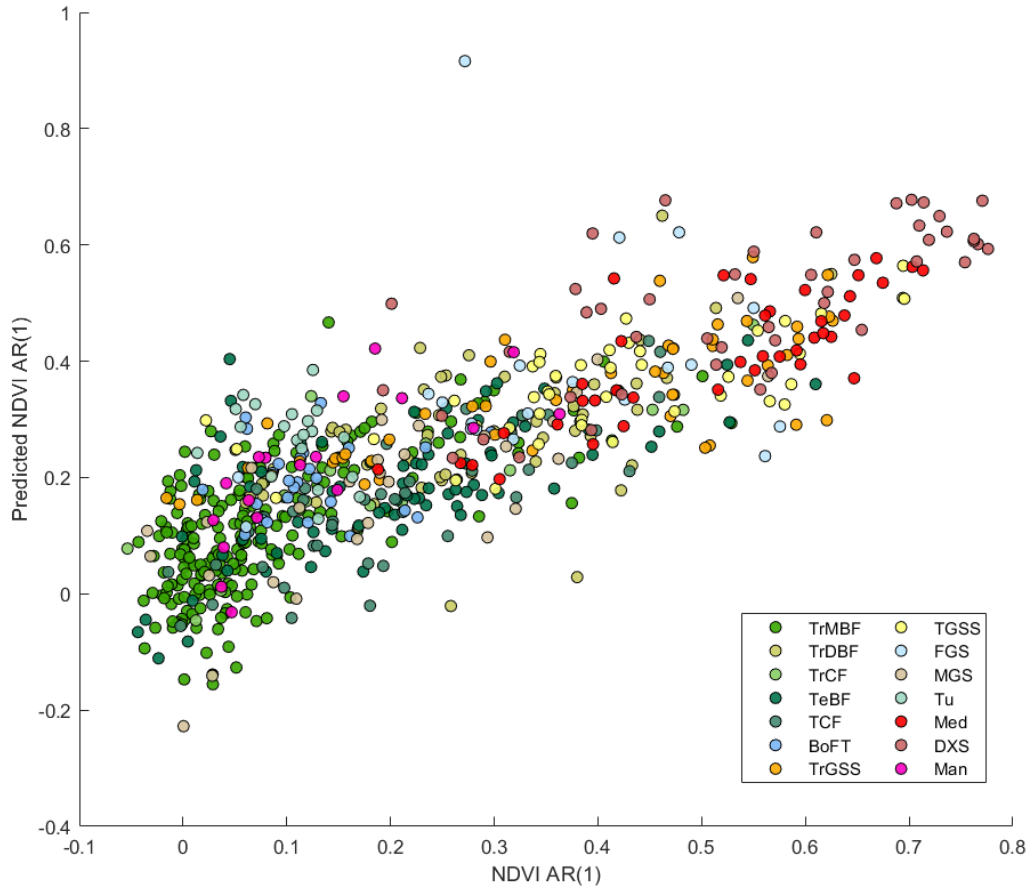

Figure 5.6: Comparison of NDVI AR(1) with the predicted AR(1) values from the linear regression model at the ecoregion scale. Ecoregions are coloured according to their biome. The model used for this is AR(1) ~ log(MAP) + Temperature + Trees. Rho: 0.83, p<2.2e-16.

5.4.6 VOD Resilience and Climate Variables

We also measure vegetation resilience with data from the Vegetation Optical Depth Climate Archive which provides a measure of vegetation structure and water content.

The spatial distribution of vegetation resilience as measured with VOD (Figure 5.7) shows a similarity to NDVI AR(1). High AR(1), and therefore low resilience, is seen in Australia, the Mediterranean and southern Africa, which mirrors the NDVI resilience measure. Similarly, low AR(1) (and high resilience) is seen in tropical forests and high latitudes.

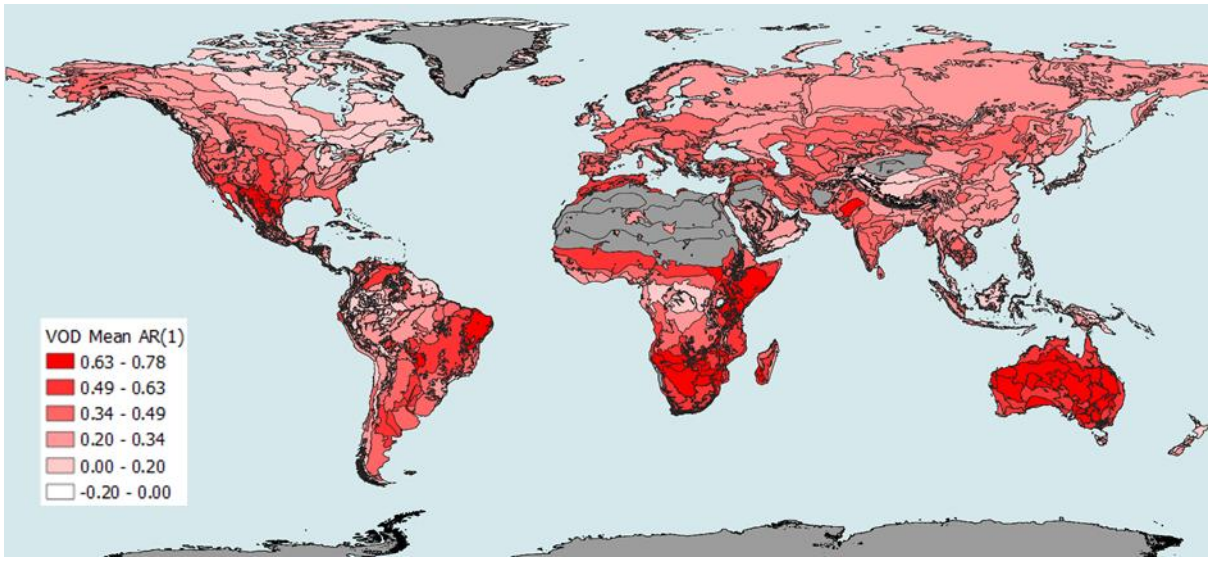

Figure 5.7: Map of VOD mean AR(1) values aggregated by ecoregion. Higher AR(1) values correspond to less resilient vegetation. Low vegetation pixels are removed if VOD <0.25, ecoregions in grey have had more than 50% of their pixels filtered out.

A comparison of VOD mean AR(1) with precipitation (Figure 5.8) supports our evaluation that drier ecoregions are less resilient. However, at the ecoregion scale, resilience, as measured by VOD, is less closely correlated with precipitation (rho = -0.43, $p<2.2e-16$) than

our NDVI AR(1) measure. Unlike NDVI, there is no clear precipitation threshold below which resilience begins to decline.

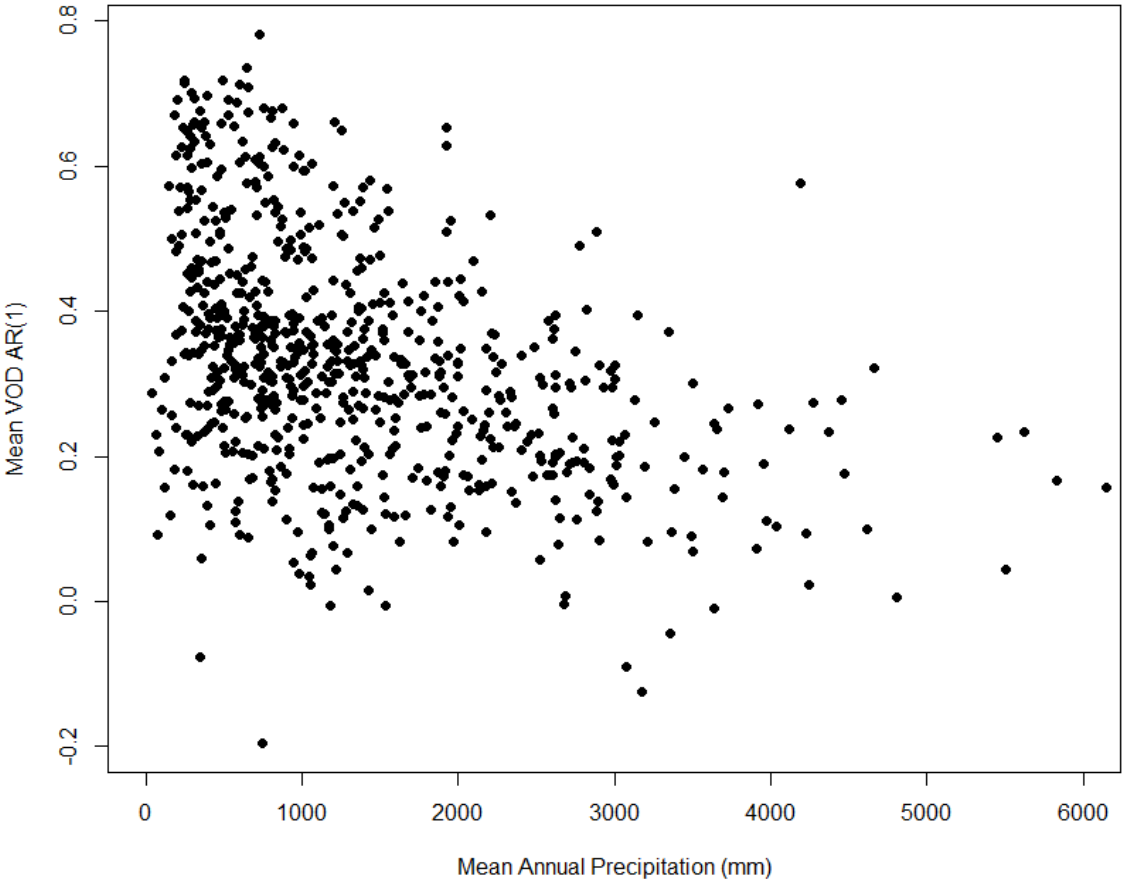

Figure 5.8: Mean VOD AR(1) compared with mean annual precipitation. VOD pixels with low vegetation levels (VOD <0.25) are removed prior to analysis and VOD ecoregions with less than 50% pixels remaining are also removed. Rho = -0.4345, with p<2.2e-16.

We construct the same multivariate regression models for VOD AR(1) to detect the influence of climate variables on resilience (Table 5.2). Compared to those of our NDVI AR(1), these display less predictive power when using VOD data; this is unsurprising given the lower correlation between VOD AR(1) and precipitation.

Table 5.2: R^2 value for VOD linear regression models.

VOD Regression model	VOD Ecoregion result R^2
AR(1) ~ MAP + Temperature	0.2746
AR(1) ~ log(MAP)	0.1635
AR(1)~ Temperature	0.04995
AR(1) ~ log(MAP) + Temperature	0.2682
AR(1)~ Temperature + DSL	0.3387
AR(1) ~ log(MAP) + Temperature + DSL	0.3437
AR(1) ~ log(MAP) + Temperature + DSL + Tree Cover	0.3569
AR(1) ~ log(MAP) + Temperature + Tree Cover	0.3135

5.4.7 Recovery time scales

In this analysis, we have used remotely sensed data with a monthly resolution to analyse resilience. However, following a perturbation, some vegetation may display a recovery time which is faster than 1 month, thus making it difficult to resolve these responses with monthly resolution data. As outlined in *Chapter 2*, the relationship between AR(1) and the

recovery rate λ is as follows:

$$\alpha(n) = e^{\lambda \Delta t n} \tag{5.1}$$

With the recovery timescale of a system equal to 1/ λ (assuming linearity). We can therefore establish an AR(1) threshold below which the recovery timescale will be faster than 1 month. As discussed in *Section 5.3.3*, the detrending method can cause a shift in AR(1) values. As such, we consider the recovery timescale from the raw data. From equation 5.1 above, a pixel with a recovery timescale shorter than 1 month corresponds to a mean AR(1) of 0.367 or lower. Therefore we plot the mean AR(1) from the raw NDVI data (Figure 5.9) to ascertain which pixels fall below this threshold.

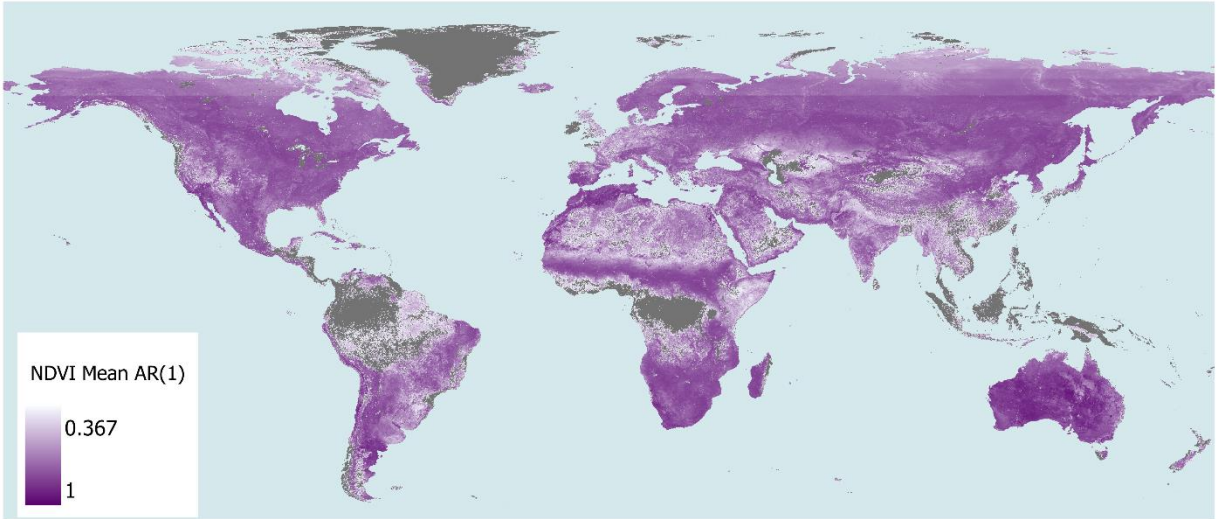

Figure 5.9: NDVI Mean AR(1) from monthly data with no detrending or removal of the seasonal cycle. Values which are below 0.367, corresponding to a response timescale < 1 month, are shown in grey.

Here we can see that the primary areas which may have a response timescale lower than our data temporal resolution are dense tropical forests. These high biomass regions may respond too quickly to the average perturbation to be detected at a monthly resolution. This suggests that some caution is needed when considering trends in these regions.

Similar spatial trends are observed with VOD data, as seen in Figure 5.10. Less tropical forest pixels have a recovery timescale less than 1 month with VOD, as the recovery in 'greenness' for NDVI appears to be faster than the recovery in biomass as recorded by VOD. Some high latitude regions also display a fast timescale for VOD data.

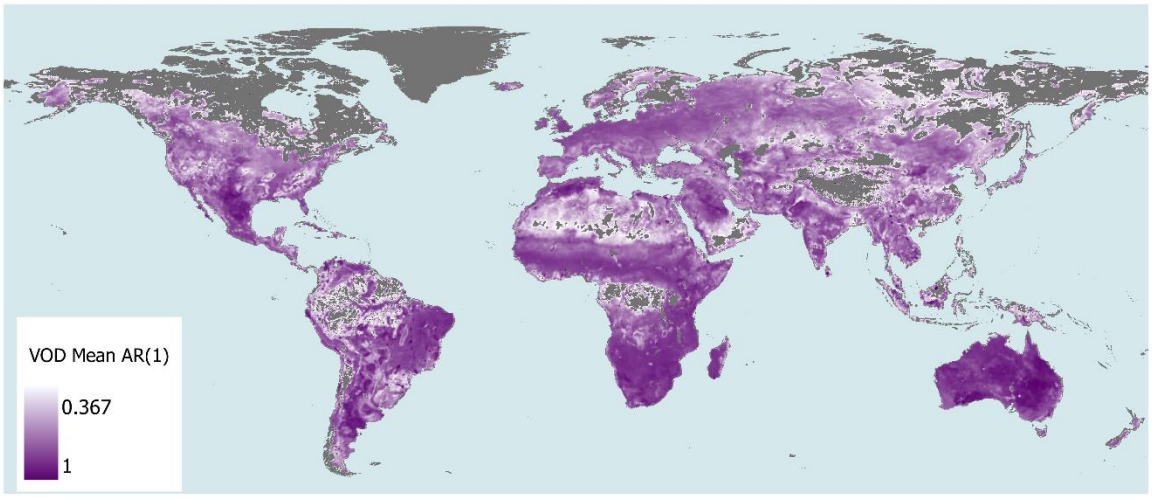

Figure 5.10: Mean VOD AR(1) which have not been detrended or decycled. Grey areas correspond to regions with a recovery time less than 1 month (mean AR(1) <0.367), or to areas with no data.

We then assess whether removing the pixels which display a <1 month recovery time improves the predictive ability of our regression models (Table 5.3). However, we can see that this is not the case for the NDVI AR(1) models. For example, the regression model

which consists of log(MAP), temperature and tree cover has a lower R^2 value when we have filtered out these pixels (R^2 = 0.6009) compared to our initial model (R^2=0.6715). However, the VOD AR(1) regression models seem to be improved by removing these pixels; this suggests that VOD resilience in these highly forested pixels may be difficult to predict with these climatic variables.

Table 5.3: Regression model results of NDVI and VOD resilience for ecoregions where pixels have been removed that correspond to a response timescale which may be too fast to detect with monthly resolution data.

Regression model	NDVI - Ecoregion scale without AR(1) values less than 0.367: R^2 values	VOD - Ecoregion scale without AR(1) values less than 0.367: R^2 values
AR(1) ~ MAP + Temperature	0.4914	0.3268
AR(1) ~ log(MAP)	0.404	0.209
AR(1)~ Temperature	0.08259	0.0538
AR(1) ~ log(MAP) + Temperature	0.5725	0.2996
AR(1)~ Temperature + DSL	0.5051	0.3823
AR(1) ~ log(MAP) + Temperature + DSL	0.5721	0.3875
AR(1) ~ log(MAP) + Temperature + DSL + Tree Cover	0.6002	0.459
AR(1) ~ log(MAP) + Temperature + Tree Cover	0.6009	0.3568

5.5 Discussion

5.5.1 Relationship of resilience with climate

We find a clear relationship between precipitation and vegetation resilience across the world; this is evident at the local pixel, ecoregion and biome scale, with a sharp decline in resilience for precipitation levels <2000 mm year^{-1}. This corroborates and builds upon the results of Verbesselt *et al.* (2016), which identifies this trend within tropical forests. With climate change likely to cause precipitation levels to decline in drier regions (Trenberth, 2011), this is likely to lead to a decline in vegetation resilience in areas which already experience threats to vegetation. In addition to this, we identify the role that temperature plays in vegetation resilience, with hotter and drier regions, such as the Mediterranean, Deserts and Montane Grasslands, showing lower levels of resilience. Expected temperature increases from climate change will further compound vegetation resilience decline in low rainfall regions. The spatial distribution of resilience in this analysis, with low resilience seen in regions such as Australia, southern Africa, the Mediterranean and southwestern USA, is in agreement with the resilience model presented in De Keersmaecker *et al.* (2015).

Regions with higher average precipitation, such as tropical forests, display higher levels of resilience. However, that does not guarantee the long-term stability of these regions. For example much of the moisture in the Amazon basin is recycled within this ecosystem (Salati *et al.*, 1979). Anthropogenic pressure, such as deforestation, can reduce this moisture recycling; consequentially the lower levels of rainfall may lead to a decline in resilience, with Boulton, Lenton and Boers (2022) identifying greater loss of resilience in drier parts of the Amazon.

5.5.2 Comparison of resilience measured from NDVI and VOD

A parallel analysis with VOD data was conducted to assess the validity of the relationship between resilience as measured by NDVI and climatic variables. While VOD is lower resolution that MODIS NDVI, it is not affected by cloud cover and has a lower sensitivity to atmospheric water vapour. Although the time frames of each dataset are not exactly the same, the mean AR(1) values from VOD and NDVI are broadly consistent (Figure 5.11) and are highly correlated (rho = 0.67, $p<2.2e-16$). It also seems that on average, ecoregion level NDVI AR(1) displays a greater range of values than VOD AR(1), with a regression analysis showing a gradient of 0.54. Relatively lower AR(1) values (corresponding to a faster recovery rate) are to be expected for NDVI compared with VOD, as following a perturbation vegetation structure (as measured by VOD) can take longer to return than greenness (as measured by NDVI).

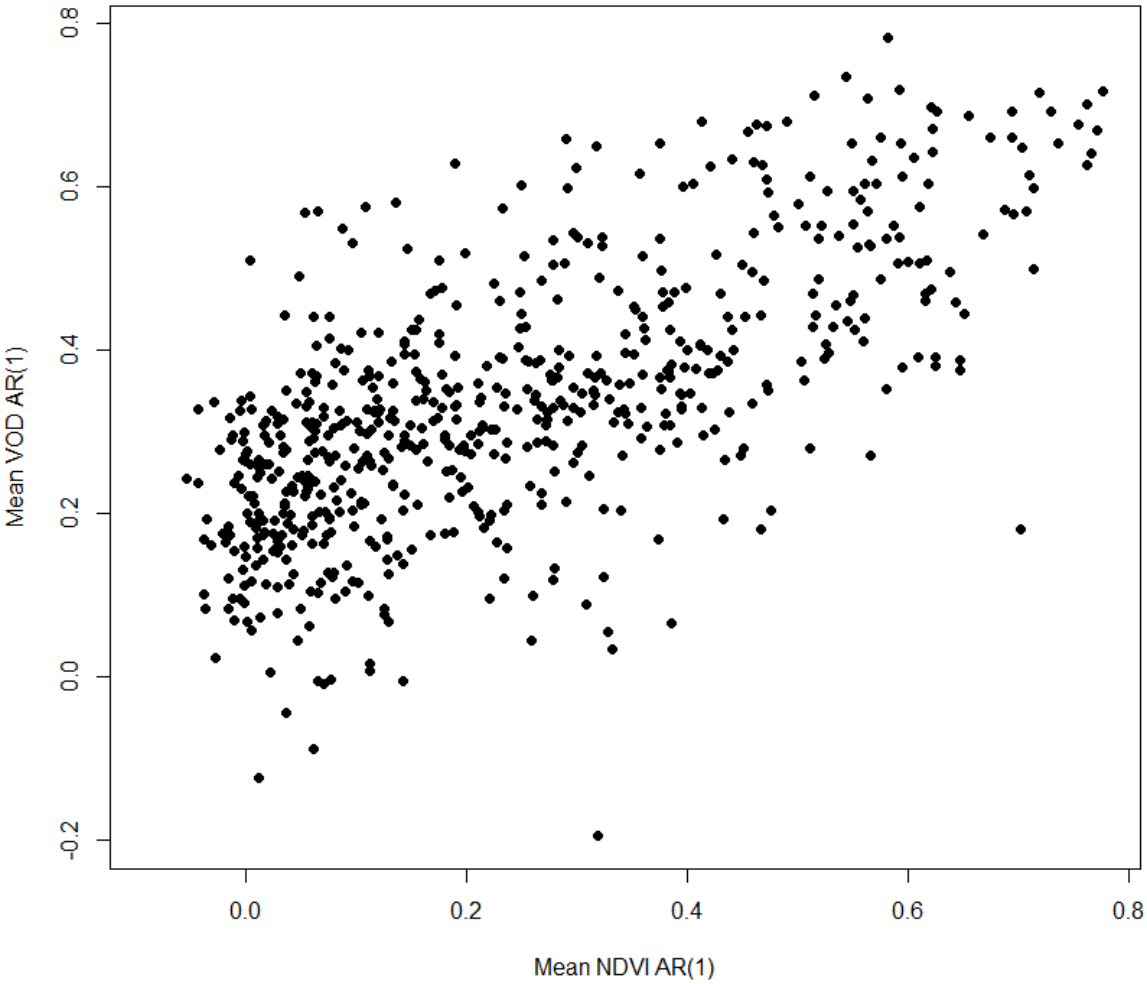

Figure 5.11: Comparison of mean NDVI AR(1) and mean VOD AR(1) at the ecoregion level. Rho = 0.67, p<2.2e-16.

Precipitation accounts for much of the variation in each of these measures. Longer response times seen with VOD (Figure 5.10) are likely due to it providing a measure of changes in vegetation structure, which takes longer to recover from a perturbation, compared to NDVI measuring greenness. It is also possible that following a disturbance, vegetation may be replaced, i.e. forest with grassland; this is more likely to be reflected in a nuanced way in VOD than NDVI. However, at a global scale, climatic means appear to explain NDVI resilience

more than VOD resilience, with precipitation more closely correlated to NDVI AR(1). It is possible that while VOD provides a greater measure of resilience in specific ecosystems, such as tropical forests (Boulton, Lenton and Boers, 2022), the generality of NDVI allows for a broader application across the globe.

5.5.3 Temporal resolution and recovery timescales

We identify densely vegetated, high resilience regions as having an average recovery timescale which may be faster than 1 month, as seen in Figure 5.9 and 5.10. This means that it will not be possible to record the response of an average perturbation for vegetation in these regions. This occurs for both NDVI and VOD, although for a larger area in the NDVI dataset, corresponding to a faster response of greening. These areas are removed from the analysis in De Keersmaecker *et al.* (2015) owing to the poor fit for the resilience model. When we filter out all of the pixels which have a recovery time of less than 1 month, we find no improvement in our regression models. This suggests that while some caution should be applied when considering resilience in these regions, the global relationship between climatic variables and resilience still seems to hold.

5.5.4 Limitations and future work

Our regression model analysis shows that precipitation, temperature and tree cover account for much of the variation in resilience. However, by comparing the initial NDVI AR(1) values with the predicted AR(1) values, it seems that the regression model is unable to predict the highest AR(1) values (corresponding to the ecoregions with the lowest resilience). These ecoregions are generally the hottest and driest, and it may be that there is a non-linear relationship between these variables. This therefore suggests that a non-linear regression

model may need to be used to better predict vegetation resilience. In addition to this, the regression analysis considers all ecoregions regardless of biome classification. It is likely that the relationship between vegetation resilience and climate varies between biomes. Future work may separate this analysis out between biomes to account for these differences and to better predict resilience levels.

High latitudinal regions display low AR(1) values in our study. This would suggest that vegetation in these regions is resilient, a surprising result given the changing climate regimes in high latitudes (Walsh *et al.*, 2020). However snow cover is likely to introduce noise into the data in these regions (De Keersmaecker *et al.*, 2014). We also know that trends in NDVI in these regions are inconsistent, with both browning and greening observed due to climate change (Myers-Smith *et al.*, 2020). This suggests that the resilience values in these regions may be unreliable. The high latitude biomes are clear outliers in Figure 5.3, as such we conduct a regression analysis with these regions removed. This shows that climatic variables have a greater predictive power for ecoregion level resilience when these anomalous high latitudinal regions are removed.

The analysis presented in this study has focused on the mean vegetation resilience state and how this relates to mean climatic variables across the world. This provides the basis to monitor how these resilience states are changing over time. This has been done in regional analysis and there have been some efforts to apply this globally (Feng *et al.*, 2021). However, combining NDVI and VOD data with cloud computing resources may offer an opportunity to detect changing vegetation resilience with a changing climate. Future work may apply NDVI and VOD datasets to analyse resilience in specific ecosystems, with VOD applied to forests and NDVI to grasslands. The biome and ecoregion data from

Ecoregions2017 and tree cover maps providing a useful way to decide this division. In addition to this, other studies may seek to apply data with a greater temporal resolution in an attempt to resolve issues discussed in this study surrounding the response timescale of highly resilient, densely vegetated regions.

5.6 Conclusion

Here we have shown the close relationship between climatic variables, primarily precipitation, and vegetation resilience across the globe, as validated by both NDVI and VOD data. There is a precipitation threshold of approximately 2000 mm $year^{-1}$ below which vegetation resilience declines. This relationship is repeated at the biome, ecoregion and local level. With current water-scarce regions expected to get drier with climate change, this suggests that vegetation will be at further risk in these areas. Increased temperatures are also likely to contribute to resilience loss. Further efforts should seek to monitor these vegetation resilience trends, with a particular focus applied to regions of low resilience.

Chapter 6: Discussion

6.1 Thesis synthesis - Measuring ecosystem resilience using satellite data

The work presented in the previous three chapters of this thesis has sought to assess the ability of remote sensing for analysing and understanding the resilience of terrestrial ecosystems. This has included an analysis of the impact of community-driven agroforestry projects in the Mount Kenya region, the resilience of patterned vegetation in the Sahel and finally how vegetation resilience is influenced by climate across the world. This chapter provides some reflection on the merits of this approach and what has been learnt from it within the context of the initial research questions.

This thesis considers a simple notion of resilience that relates to the increased return time of a system following a perturbation. *Chapters 3* and *4* focused on dryland regions with high turnover of vegetation as likely candidates for the manifestation of detectable vegetation resilience signals. This focus is then expanded to study ecosystem resilience across the globe at multiple spatial scales in *Chapter 5*.

The analysis presented in *Chapter 3* revealed that the actions of a network of smallholder farmers can generate an observable greening effect at the landscape scale in the Mount Kenya region. This greening trend occurred both within and around tree planting groves and it appears that when linked with sustainable agriculture, this network has a multiplicative effect which is observable with Landsat 7 data. Owing to Landsat 7 data constraints (as discussed in *Section 6.2*), an effective assessment of resilience signal from this activity was not possible. However, once sufficient Landsat 8 data is available this will provide fertile territory for future research. This analysis is among the first to focus on applying remote

sensing to assess the effect of a widespread bottom-up approach to afforestation and agroforestry, which has the potential to promote a more sustainable landscape-level change. The rapid growth of networks like TIST which enhance community capital and spread knowledge and environmental awareness to smallholder farmers present a clear example of the power of rapid positive environmental-social tipping points.

The focus on vegetation resilience in dryland systems continues in *Chapter 4*, where consideration is given to patterned vegetation in the Sahel and the applicability of remote sensing to quantify it and its resilience. This work shows the capability of Sentinel-2 data to assess vegetation pattern connectivity through Offset50, a feature vector metric. This enabled the differentiation between four classes of vegetation pattern and assessment of the widespread hypothesis that pattern morphology is an indicator of ecosystem resilience. While this notion has been suggested in the literature (Rietkerk *et al.*, 2004; Mayor *et al.*, 2013), prior to this analysis it had only been tested in models where it was found to not apply for certain classes of vegetation model (Dakos *et al.*, 2011). For the sites featured in this study, the hypothesised relationship between pattern morphology and ecosystem resilience does not hold for the resilience measures considered (AR(1), variance and return rate following a perturbation). It seems that no other studies have applied regularly returning satellite data to assess the resilience of patterned vegetation. Precipitation is identified as a key driver of vegetation patterning and also resilience, with drier regions displaying less connected vegetation patterns with lower levels of resilience. Geographical gradients of patterned vegetation resilience are reflective of wider precipitation gradients. It is clear that observations from high resolution satellites are immensely valuable to studying these sites and the collection of Sentinel-2 data over a longer timeframe will allow the development of a greater understanding of the resilience of these patterned systems.

Having established a link between precipitation and the resilience of patterned vegetation in the Sahel, remote sensing was applied at the global scale to evaluate the impact of climatic variables on vegetation resilience across the world in *Chapter 5*. By considering resilience levels across multiple spatial regions with MODIS NDVI data, i.e. a space-for-time substitution analysis, a strong relationship between vegetation resilience (mean AR(1)) and precipitation is identified. This occurs at the pixel, ecoregion and biome scale. The sharp decline in resilience below a precipitation threshold of 2000 mm per year indicates that declining vegetation resilience in drier regions is a risk should precipitation levels fall. In addition to this, there is a temperature component of resilience, with hotter, drier regions displaying lower vegetation resilience. Comparing these NDVI resilience results with VOD data corroborates this relationship between vegetation resilience and precipitation. However, the greater predictive power of climate variables for NDVI resilience suggests that relative to VOD, NDVI has greater utility when applied at a global level owing to its generality. In addition to this, some regions of the world display a resilience level which is consistent with a return time of less than 1 month following an average perturbation. This suggests that there may be some limitations to the use of monthly resolution satellite data for analysing resilience trends.

While each research chapter in this thesis focuses on a different geographical region, this body of work is unified by its attempt to apply remote sensing data to understand the development and resilience of vegetation systems. A commonality of each of these studies is the use of NDVI to measure the state of vegetation and to infer its resilience. This relies on the link between NDVI, the photosynthetic capability and productivity of these plants, i.e. vegetation health. Changes in NDVI level, and therefore plant health, can be used to understand the resilience of these vegetated systems when they experience a perturbation;

with the recovery rate of these systems indicating its resilience. This can be measured directly or if this is not possible, then indirectly with statistical measures such as AR(1). The resilience of vegetation may be affected by one factor, such as a changing climate or anthropogenic pressure, which leads it to be more susceptible to mortality inducing events from other perturbations, such as fires, pests or disease. Clear increases in NDVI are observed in Kenya through the tree planting activities of TIST in *Chapter 3*, while vegetation resilience is shown to strongly relate to climate via an NDVI derived measure of resilience in *Chapter 5*.

Another lesson that can be drawn from this research is the need to balance the benefits and drawbacks of different remote sensing systems when considering ecosystems at varying spatial and temporal scales. Each research chapter of this thesis has applied a different satellite dataset to assess vegetation; this involves a compromise between the spatial scale of the research subject and the time period of study. High resolution Sentinel-2 data is necessary for quantifying patterned vegetation in *Chapter 4*, while despite its lower resolution, the longer time series of MODIS data makes it more appropriate for evaluating resilience at a global scale in *Chapter 5*. The size and duration of the smallholder farms which constitute the TIST network in *Chapter 3* meant that a high-resolution dataset with a long temporal length was required. In this case, Landsat 7 was the only appropriate dataset, despite its scan-line error issues. Despite the variation in datasets used across this thesis and some of their limitations, it is clear from this work that remotely sensed data enables the study of vegetation resilience in hard-to-reach locations, with increasing data capacity providing further opportunities in the future.

As well as considering the appropriateness of a dataset when designing a study, a further compromise often faced by users of remote sensing data, as with all 'big data', is the computational capacity required to analyse it. The work in each chapter of this thesis has aimed to test the capability of new cloud-computing GIS platforms, such as GEE, for performing resilience analysis across large geographical areas, including at the global scale in *Chapter 5*. It is clear that these new platforms offer the potential to increase the usability, availability and utility of remotely sensed data. However, it was necessary to conduct some parts of these studies 'offline' due to the limitations imposed by these platforms, some of which are inherent in the coding languages required to use them.

6.2 Limitations of remote sensing ecosystem resilience

While the analysis in *Chapter 3* shows the capability of remote sensing data to assess the greening effect of community-led tree planting in the Mount Kenya region, there are difficulties in detecting explicit changes in the resilience of this landscape. This is due to well documented Landsat 7 issues resulting from the scan-line error (Storey, Scaramuzza and Schmidt, 2005). While this did not drastically alter the greening trends (as detailed in *Appendix A*), it suggested that Landsat 7 may not be appropriate for assessing long term resilience trends. With start years of 2013 and 2015, Landsat 8 and Sentinel-2 did not have a sufficiently long dataset to be utilised for resilience analysis for the period of study up to 2019.

Another limitation results from the extent and availability of data. While remotely sensed datasets continue to expand both in spatial and temporal extent, the existing archive of this data does not always align with the time scales associated with changes of vegetation resilience. *Chapters 3* and *4* focused upon equatorial drylands with fast growing vegetation, as it was expected that these resilience signals would be manifested more clearly in these regions. However, for the study conducted in *Chapter 4*, Sentinel-2 data, the only freely available satellite collection of sufficiently high spatial resolution, was only available for four complete years over the study period. While a measure of resilience is provided through AR(1), variance and return rate, it was not possible to provide a longer-term measure of the trends in resilience of these patterns. It is possible that observations of resilience trends from shorter time series are driven by underlying variability in the climate system. Longer term observations from the accumulation of satellite data can begin to detect whether

these trends are a true shift in ecosystem resilience or the manifestation of multi-decadal climate variability.

Consideration must also be given to the resolution of remote sensing data. If the average recovery rate of a system following a perturbation is greater than the temporal resolution of the satellite, then there is a chance that the system's response to an average perturbation may go undetected. It is therefore apparent that there is a trade-off between high temporal resolution to detect all perturbations and the monthly aggregation steps taken in these chapters to decrease the likelihood of missing data or anomalous values due to cloud cover. Similarly, some thought must be given to spatial resolution when designing remote sensing resilience analysis. While commercial satellites can have ultra high resolutions of 0.8m to 6.5 m (Dial *et al.*, 2003; Tyc *et al.*, 2005), for freely available satellites with regular return rates the highest spatial resolution is 10m provided by Sentinel-2 (Malenovský *et al.*, 2012). It is clear that for the majority of satellites, a single pixel incorporates numerous plants, as well as bare soil in heterogenous landscapes. Therefore, metrics of resilience may be masking changes across different vegetation types. The analysis in *Chapter 3* established that 30m pixels are sufficiently high resolution to detect a greening trend in (often) well defined TIST tree planting groves, thus suggesting that this may be an appropriate resolution to begin analysing resilience change in these ecosystems. Similarly, the approach for quantifying patterned vegetation in *Chapter 4* is accurate at 10m. Attempts to verify this at 30m were undermined by the Landsat 7 scan line error.

The work presented in each chapter of this thesis has made use of NDVI, a measure of vegetation greenness, to assess vegetation dynamics. This is a commonly used vegetation metric in the remote sensing community that has been applied to resilience detection (De

Keersmaecker *et al.*, 2014; Verbesselt *et al.*, 2016; van Belzen *et al.*, 2017; Liu *et al.*, 2019; Feng *et al.*, 2021) and was selected due to its broad applicability, both spatially and across satellite datasets. However, NDVI does have limitations, such as saturation in highly vegetated areas (Huete, Liu and van Leeuwen, 1997) and issues with soil brightness, and resilience in NDVI may not always encapsulate the full picture. Other datasets, such as VOD, which is used in *Chapter 5*, can be applied to detect changes in vegetation water content or biomass. As well as appropriate spatial and temporal resolution, the dataset selected should be tailored to the needs of the user.

Cloud cover presents a potential limitation for any remote sensing studies relying on data from passive optical sensors. Steps are taken throughout this thesis to reduce the impact of cloud cover; in the analysis presented in *Chapters 3* and *5* NDVI data is aggregated to a monthly resolution. In addition to this in *Chapter 4* any sub-images which appear as completely black, due to cloud cover, are removed and then resample this sub-image. The use of microwave-frequency sensors, such as those used to create the VOD dataset considered in *Chapter 5*, removes the issue of cloud influence, although these sensors do have limitations relating to spatial resolution.

6.3 Future work

A clear example of the way that community groups can affect environmental change in the form of regreening at a landscape scale is presented in *Chapter 3*. While this is one measure of the impact that these groups can have, there is further work that can be undertaken with other remote sensing systems. For example, LIDAR data enables the quantification of forest biomass and can be used to estimate carbon sequestration rates (Gleason and Im, 2012; Hudak *et al.*, 2012; Kaasalainen *et al.*, 2015). If this data was collected for the Mount Kenya region, it could be coupled with TIST tree growth data. This could provide a large dataset for 'ground truthing' these carbon sequestration remote sensing methods.

With rapid growth through social networks (Figure A.1) and a positive environmental impact on the surrounding landscape, organisations like TIST provide a clear example of the power of positive social tipping points and their potential for enacting environmental change. Further work should examine groups like TIST which expand through underlying social networks to assess what drives this growth. Even within TIST there is variability in its effectiveness; the TIST network in Kenya has been extremely successful in connecting farmers, while in Tanzania its influence has been much more limited. By understanding how these fast spreading and successful environmental-social groups can be replicated, rapid environmental change may be achieved in other regions.

Through this analysis, the spatial extent of TIST's greening influence was assessed, however as discussed earlier, this work was unable to directly detect how the resilience of the Mount Kenya region has changed with the actions of TIST farmers. This is due to issues with Landsat 7 imagery. Future work could utilise Landsat 8 imagery to begin to consider this resilience question. This would require the identification of TIST groves within which trees were

planted after 2013, the year that Landsat 8 was launched (Loveland and Irons, 2016), and a suitably long period prior to the tree planting to observe a change in the resilience. One approach to this may be to identify a known extreme event, such as a drought, and to compare the recovery timescale of vegetation within TIST groves to that within the surrounding area.

While the patterned vegetation analysis in *Chapter 4* focuses on the Sahel, these vegetation forms occur in drylands around the world (Deblauwe *et al.*, 2008). The published *pyveg* software package allows others to apply these analytical techniques to these sites, whether to track vegetation response to well defined events or to monitor long term trends. With the data made available from Sentinel-2 growing over time, the potential for the resilience analysis of patterned vegetation will only increase.

It is also worth considering the potential for the application of deep learning techniques to this form of analysis. With some algorithms, such as Convolution Neural Networks (CNN), being well known for their ability to identify images and patterns (Albawi, Mohammed and Al-Zawi, 2018; Li *et al.*, 2019), there is a clear applicability for these algorithms for the study of patterned vegetation. For example, if trained with a suitable dataset of patterned vegetation images, of the sort that has begun to be built in *Chapter 4*, a CNN could be applied to find and classify vegetation across the globe to enhance the previous work of Deblauwe *et al.* (2008). This could conceivably be coupled with the *pyveg* package to analyse the resilience of patterned vegetation worldwide. This could be developed alongside other efforts to apply machine learning to provide early warning signals of tipping points (Bury *et al.*, 2021).

All of the resilience analysis in this thesis relies on temporal resilience indicators, such as AR(1), variance and return rates. However, as discussed in *Chapter 2*, there are numerous spatial statistics for detecting resilience change which are often underutilised in the literature. The increasing availability of satellite data provides opportunities to assess ecosystem resilience using spatial statistics, with patterned vegetation systems being just one focus for future research.

The work presented in *Chapter 5* provides an example of the applicability of remote sensing to analyse drivers of vegetation resilience at multiple spatial scales across the globe. While this work primarily focuses on NDVI due to its broad applicability, some consideration is given to results from a VOD dataset which broadly agree with the overall trend shown in NDVI. Future work may integrate other vegetation indices or global datasets to enhance this analysis.

All of the work in this thesis focuses on resilience in terrestrial ecosystems, however resilience analysis of marine ecosystems may uncover significant trends and drivers. Rocha (2021) provides an example of the applicability of chlorophyll-a concentration data to analyse marine ecosystem resilience. Other potential analyses may consider the resilience of marine vegetation systems which display alternative states, such as giant kelp forests, which can be observed with satellite data (Cavanaugh *et al.*, 2010).

6.3.1 A framework for remotely sensing resilience trends across the world

The global resilience analysis in *Chapter 5* focused on how climate can determine ecosystem resilience across the world at different spatial scales. In addition to this, increasingly large datasets coupled with cloud computing capabilities provide a means to track changes in

resilience over time. Alongside the mean AR(1), the trend in AR(1) for pixels across the world is also considered in Figure 6.1. From this some spatial structure in the resilience trends can be seen, i.e. areas in eastern Brazil such as the Caatinga dry forests show a decline in resilience. Having identified these regions of interest, online software such as Google Earth Engine can allow the users to then zoom into these areas to undertake further analysis. This begins to provide the framework for a 'resilience sensing system', as discussed in Lenton *et al.* (2022).

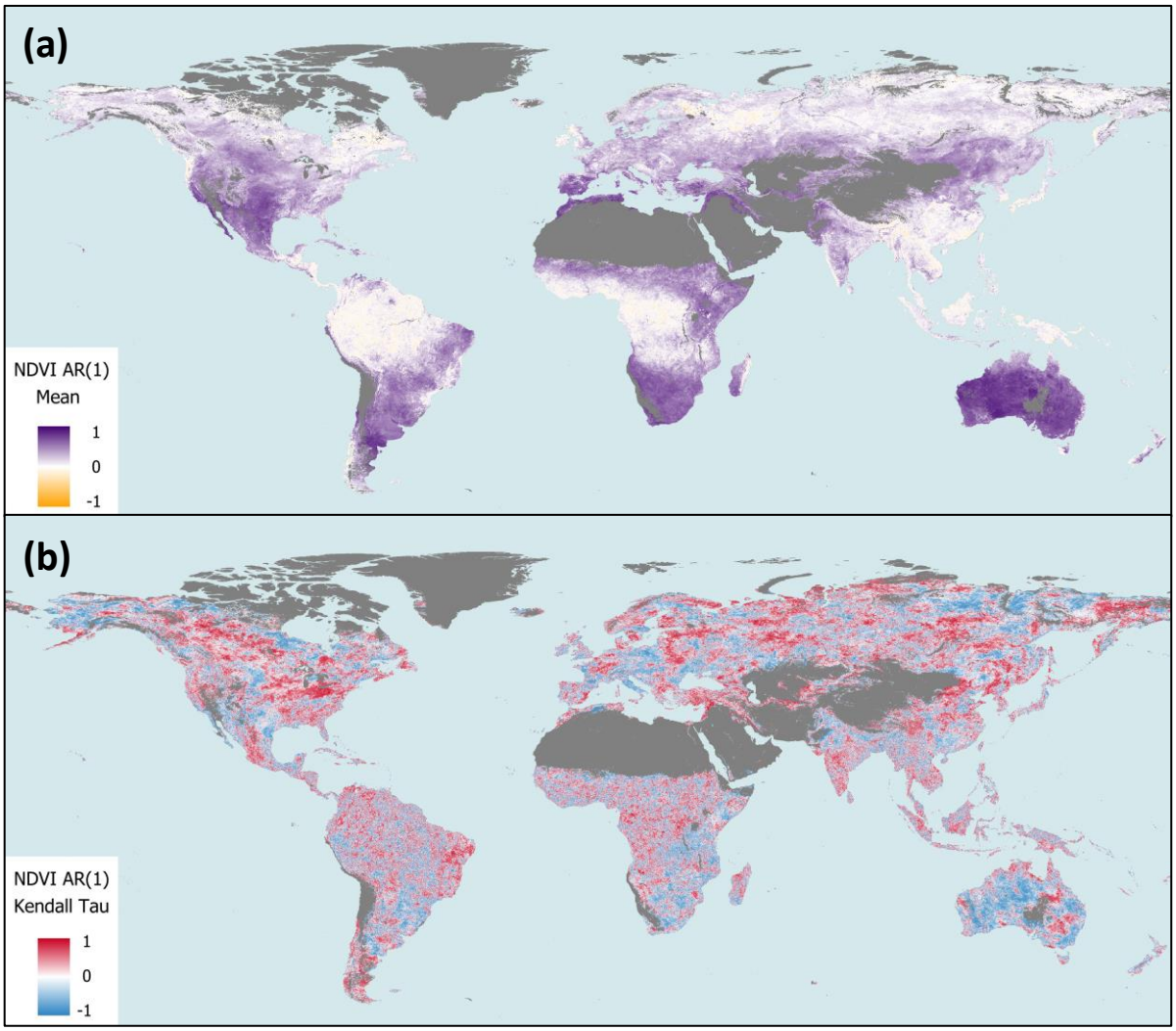

Figure 6.1: (a) Map of mean AR(1) from MODIS NDVI data, high positive values suggest low levels of resilience. (b) Map of Kendall Tau of NDVI AR(1) for each pixel. Values of 1

correspond to a monotonic increase (or loss of resilience), -1 correspond to a decrease. Grey areas are regions of low vegetation cover and are removed if the mean NDVI < 0.16. Analysis and figure production undertaken by the author and is featured in Lenton et al. (2022).

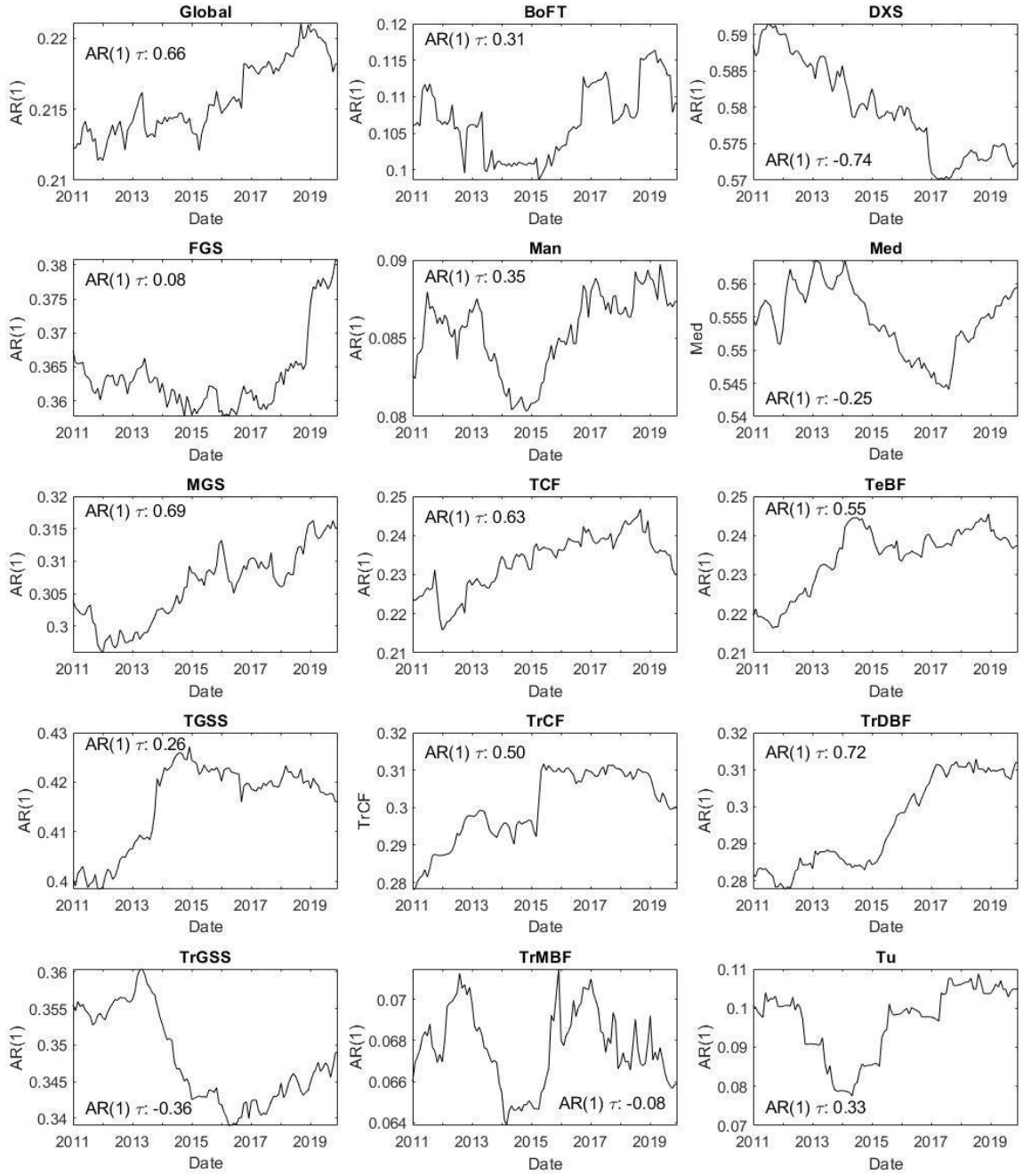

Figure 6.2: Trends in mean AR(1) when aggregated to Biome level, as well as a global average. Each region has had pixels removed where mean NDVI <0.16, in addition to this the global average has pixels removed which are classified as rock or ice. The AR(1) Kendall tau

value is included on each plot to provide a measure of the trend. Biome abbreviations correspond to the following biomes: BoFT – Boreal Forests/Taiga, DXS – Desert and Xeric Shrublands, FGS – Flooded Grasslands and Savannas, Man – Mangroves, Med – Mediterranean Forests, Woodlands and Scrub, MGS - Montane Grasslands and Shrublands, TeBF – Temperate Broadleaf and Mixed Forests, TCF – Temperate Conifer Forests, TGSS – Temperate Grasslands, Savannas and Shrublands, TrCF – Tropical and Subtropical Coniferous Forests, TrDBF - Tropical and Subtropical Dry Broadleaf Forests, TrGSS – Tropical and Subtropical Grasslands, Savannas and Shrublands, TrMBF – Tropical and Subtropical Moist Broadleaf Forests, Tu – Tundra.

Another way to conceptualise this is to aggregate this pixel data to the global and biome level to see how NDVI resilience levels have changed over time, as seen in Figure 6.2. At the global scale, with rock, ice and low mean NDVI (<0.16) pixels removed, NDVI AR(1) has steadily increased over time, with τ= 0.66, suggesting a general loss of global resilience. A noticeable loss of resilience is observable in Tropical and Subtropical Dry Broadleaf Forests (τ= 0.72), Montane Grasslands and Shrublands (τ= 0.69), Temperate Conifer Forests (τ= 0.63) and Temperate Broadleaf and Mixed Forests(τ= 0.55). The three forest biomes which display resilience loss here are identified as highly vulnerable to climate change in Wang, Zhang and Wan (2019), thus suggesting that further resilience loss is possible for these regions. In addition to this, Montane grasslands may be highly sensitive to climate change (Li *et al.*, 2018; Feng *et al.*, 2021), which suggests that the resilience loss seen in this biome here may continue with a changing climate.

One biome that shows a clear trend of AR(1) decline, and therefore resilience increase, is the Deserts and Xeric Shrublands biome. This is somewhat unexpected, as other literature has identified declining resilience in desert regions (Feng *et al.*, 2021). However, in our analysis many pixels classified as being part of the Desert biome have been filtered out due to their low NDVI values, with a majority of pixels remaining in western Australia, Namibia and parts of North America. A particular driver of this resilience trend may be caused by increased precipitation in inland areas of western and northwestern Australia (Dey *et al.*, 2019) , a region with a notable increase in resilience, as seen in Figure 6.1.

By considering which biomes display clear resilience loss trends from Figure 6.2 and then identifying regions with a clear resilience trend from our global map, areas that may warrant further study can begin to be identified. An example of this is given in Figure 6.3, where several ecoregions have been identified from resilience loss biomes which appear clearly in the map. By aggregating at the ecoregion level, the resilience loss trend in each of these regions can be seen (Figure 6.4).

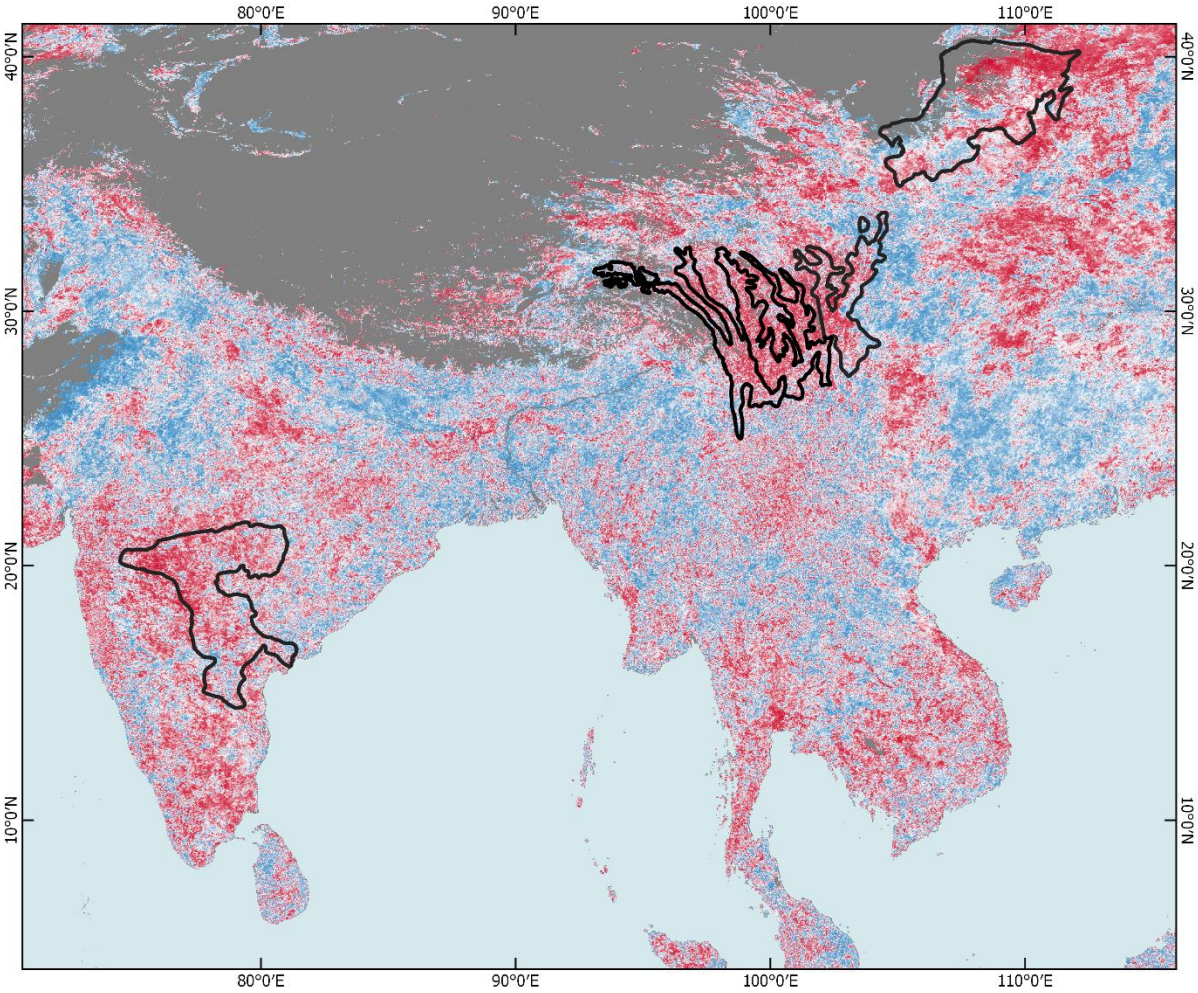

Figure 6.3: Map of AR(1) Kendall tau trends showing spatial structure of resilience loss in southern and eastern Asia with select ecoregions shown. These ecoregions are categorised as being part of three of the top four biomes to suffer resilience loss. From left to right, these ecoregions are 'Central Deccan Plateau dry deciduous forests', 'Nujiang Langcang Gorge alpine conifer and mixed forests', 'Hengduan Mountains subalpine conifer forests', 'Qionglai-Minshan conifer forests' and 'Ordos Plateau steppe'. Pixels with a mean NDVI <0.16 are shown in grey and have been filtered out. Analysis and figure production undertaken by the author and is featured in Lenton et al. (2022). The time series of AR(1) Kendall tau for these ecoregions is shown in Figure 6.4.

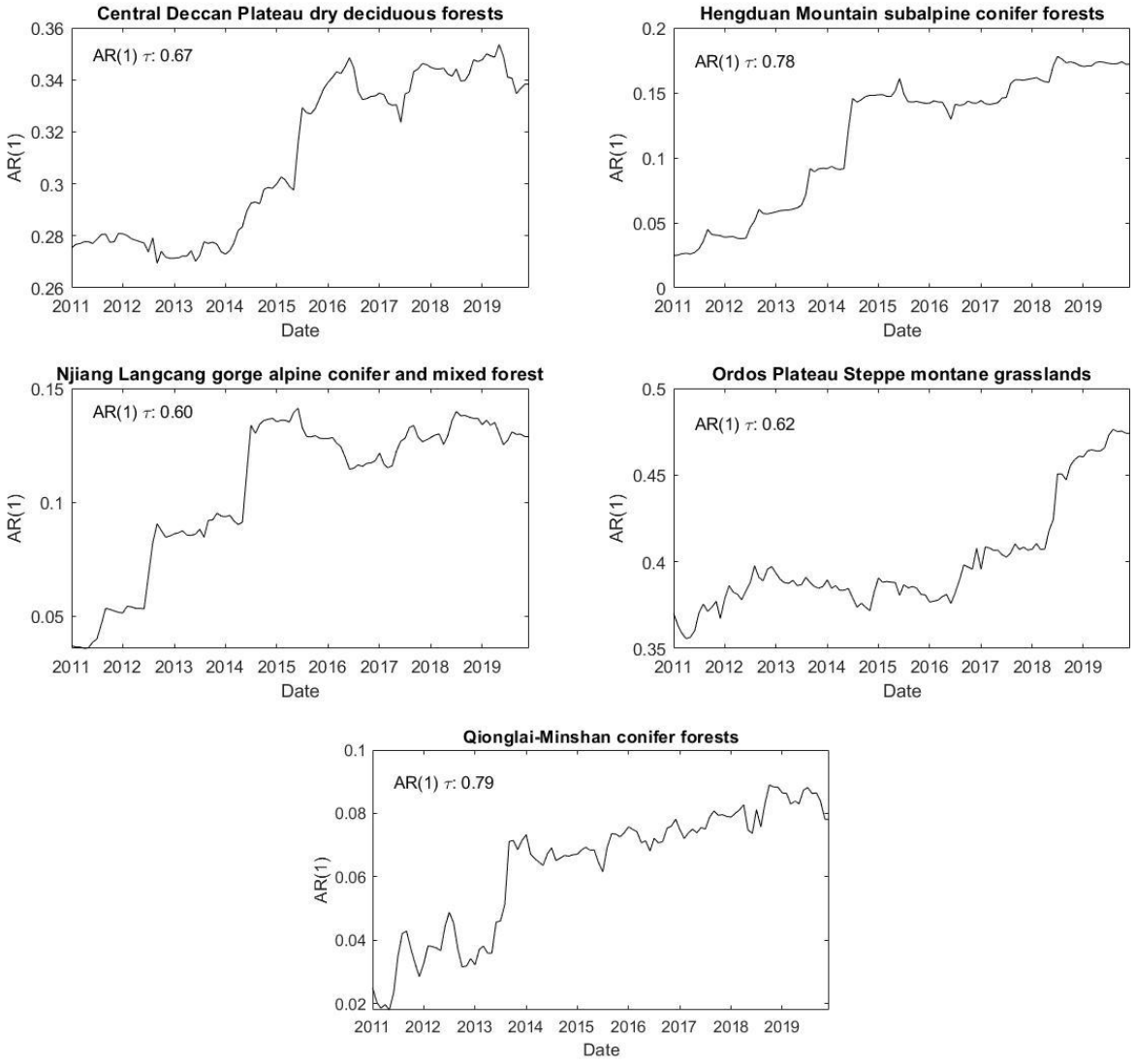

Figure 6.4: Trends in AR(1) averaged over each ecoregion featured in Figure 6.3, along with the Kendall tau value of each time series. Each ecoregion displays an increase in AR(1) over the study period, thus suggesting a loss of resilience.

Here a selection of ecoregions have been presented to show the utility of global scale remote sensing for monitoring resilience vegetation trends. While further work is needed to completely verify the validity of these trends and to investigate the underlying drivers, it is clear that this approach has the potential to yield powerful insights. Several biomes display

noticeable trends in resilience loss and should be the target of further study. Combining remotely sensed data with cloud computing enables a flexible approach to assessing vegetation resilience across the world at multiple spatial scales. Future work should aim to develop this with expanded vegetation resilience monitoring from other remotely sensed datasets, increased accessibility of cloud computing resources and employ vegetation models to assess where resilience loss is most likely in the future, so that monitoring can be targeted. These monitoring efforts will reveal where vegetation is experiencing resilience loss from a changing climate or direct anthropogenic pressure, and could influence targeted interventions to prevent this. Distinguishing between the drivers of these resilience changes could be achieved by monitoring human activity through physical features on the landscape, such as roads and buildings, which can be identified with machine learning land classification algorithms. This can be compared with the influence of climatic variables.

6.4 Conclusion

The research in this thesis has shown the capability of remotely sensed data to assess vegetation resilience and to identify its potential for detecting ongoing changes in resilience. This has taken the form of an evaluation of the potential for rapid change through direct human intervention, the resilience of visually striking vegetation patterning in drylands and then a broader perspective of the climatic drivers of vegetation resilience across the world.

Mobilising positive environmental-social tipping points of the kind presented by TIST offers a potential solution to environmental degradation. Satellite data can then be employed to analyse the effects, both direct and indirect, of these upon the landscape, with future data availability offering a path to directly evaluating the resilience of these landscapes.

Data provided by satellites display great potential for assessing vegetation resilience in hard-to-reach regions, such as patterned vegetation sites. While vegetation morphology may not be directly linked with resilience, it is clear that precipitation is a driver of both morphology and resilience. With the accumulation of more data, there will be an increased ability to conduct long-term resilience monitoring and to untangle multi-decadal climate variability from true ecosystem resilience trends.

Further to this, the global relationship between climatic variables, such as precipitation, and vegetation resilience is shown. This relationship is likely to become more important with climate change induced shifts in precipitation regimes. Through this, and the work presented in the discussion, it is clear that the combination of global level remote sensing data with increasingly available cloud computing platforms provides a path towards adaptable resilience monitoring of terrestrial ecosystems. This can be applied at multiple

spatial scales and targeted to specific regions. Further enhancements of these efforts are possible through the increased accessibility of these platforms and a variety of additional remote sensing datasets.

Appendix A: Supplementary Information for Community-driven tree planting greens the neighbouring landscape

Supplementary Figures:

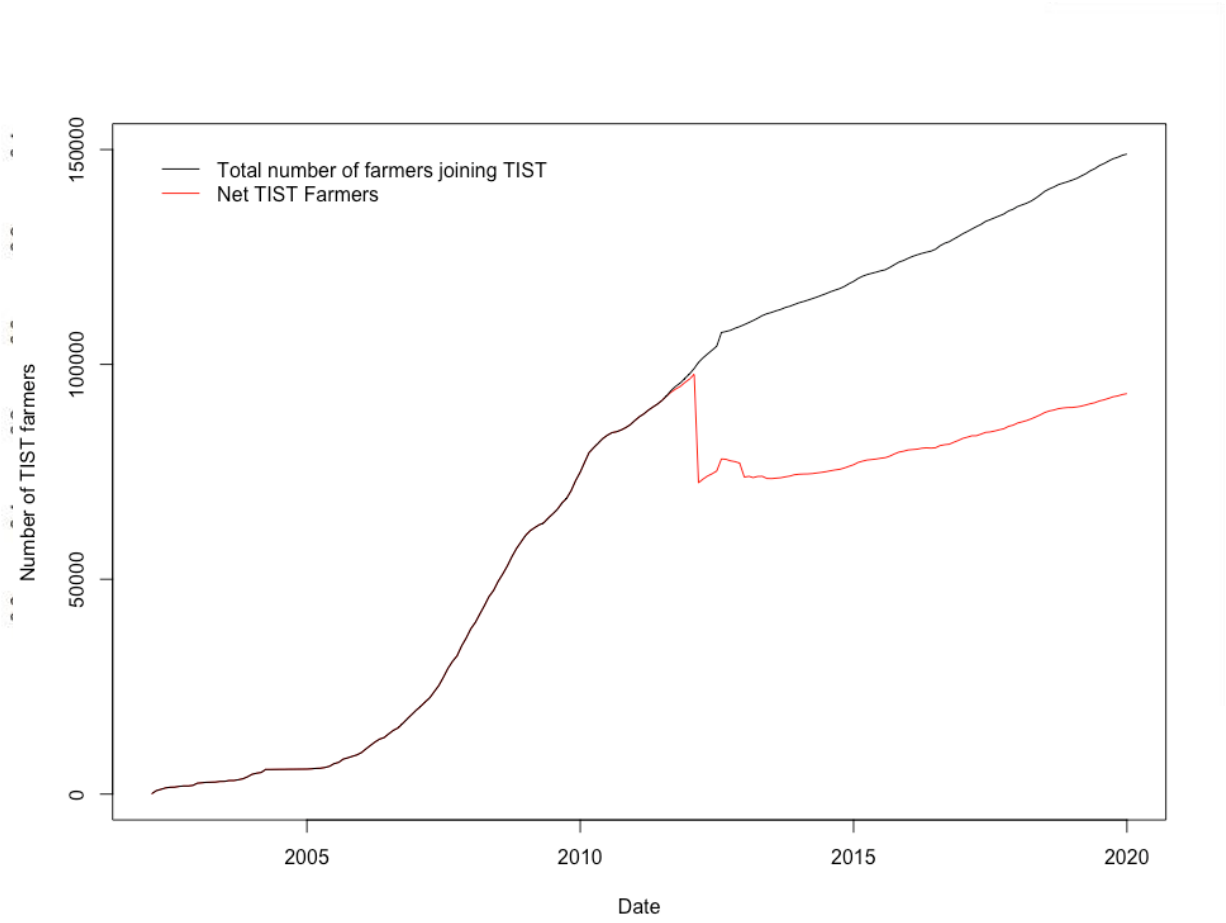

Figure A.1: Plot of the growth of farmers in the TIST network across all four countries (Kenya, Tanzania, Uganda and India). This growth curve shows similarities of an s-curve associated with a tipping point. Data is aggregated at the monthly scale. The black line shows total number of farmers who have joined the network by that month. The red line shows the number of farmers still in the network, with a major decline in March 2012 corresponding to a concerted effort to remove farmers from the database who had left the network.

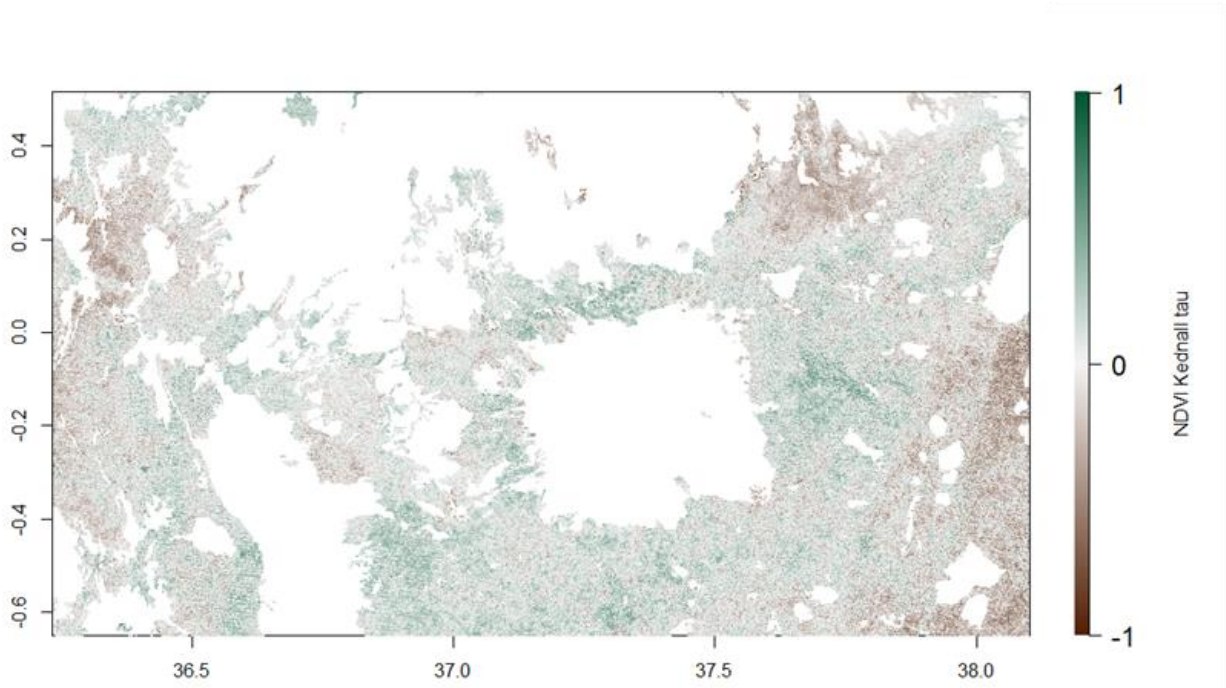

Figure A.2: Map of NDVI Kendall Tau trends across the agricultural land within the study area for the period 2000-2019.

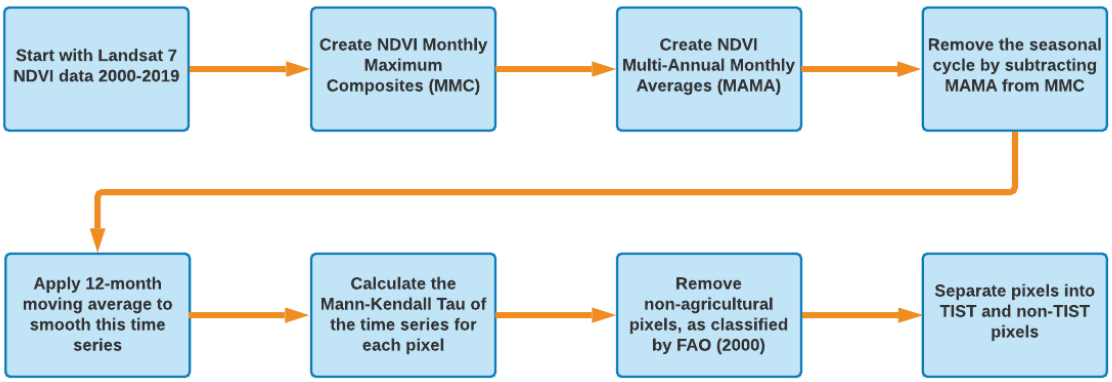

Figure A.3: Data analysis workflow for calculation of NDVI Kendall Tau trends across the study area.

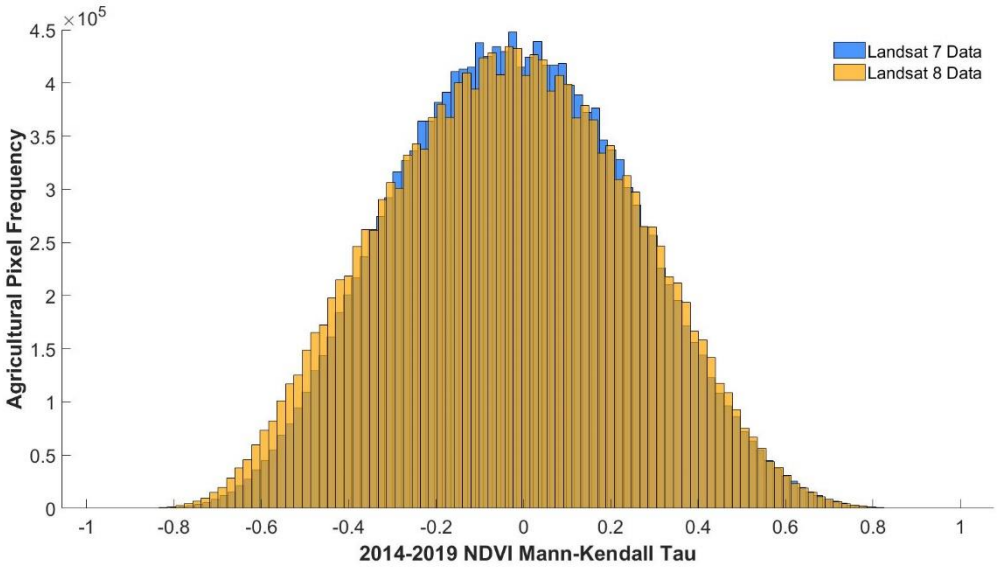

Figure A.4: Comparison of Kendall tau values of 2014-2019 Landsat 7 and Landsat 8 data for agricultural pixels in the study area.

Supplementary Tables:

Table A.1: Standard error of the mean for NDVI Kendall Tau values of TIST neighbouring classes.

Distance from TIST (m)	Standard Error of the Mean
0	3.43E-04
30	3.34E-04
60	3.32E-04
90	3.38E-04
120	3.49E-04
150	3.62E-04
180	3.74E-04
210	3.88E-04
240	4.09E-04
270	4.15E-04
300	4.30E-04
330	3.44E-05
360	3.45E-05
390	3.45E-05
420	3.46E-05
450	3.48E-05
480	3.48E-05
510	3.49E-05

Table A.2: Values from the Categorical Regression Model used to assess the extent of TIST's landscape effects. Values which are significant with a p-value <0.05 are presented in bold. This suggests that areas up to and including 360 metres display a distinct difference to the local background greening trend.

Distance (metres)	Estimate	Std. Error	p-value
0	**0.0668**	**0.000342**	**<2e-16**
30	**0.0364**	**0.000339**	**<2e-16**
60	**0.0228**	**0.000335**	**<2e-16**
90	**0.0176**	**0.000341**	**<2e-16**
120	**0.0144**	**0.00035**	**<2e-16**
150	**0.0117**	**0.000363**	**<2e-16**
180	**0.00914**	**0.000375**	**<2e-16**
210	**0.00694**	**0.000389**	**<2e-16**
240	**0.00518**	**0.000409**	**<2e-16**
270	**0.00449**	**0.000416**	**<2e-16**
300	**0.00308**	**0.00043**	**6.85E-13**
330	**0.0029**	**0.000446**	**8.09E-11**
360	**0.00191**	**0.000456**	**2.75E-05**
390	0.000541	0.000468	0.248
420	0.000582	0.000486	0.231
450	-0.0003	0.000492	0.548
480	0.00046	0.000501	0.358
510	-0.00016	0.00051	0.754

Appendix B: Supplementary Information for Quantitatively monitoring the resilience of patterned vegetation in the Sahel

Supplementary Figures

Testing site size impact

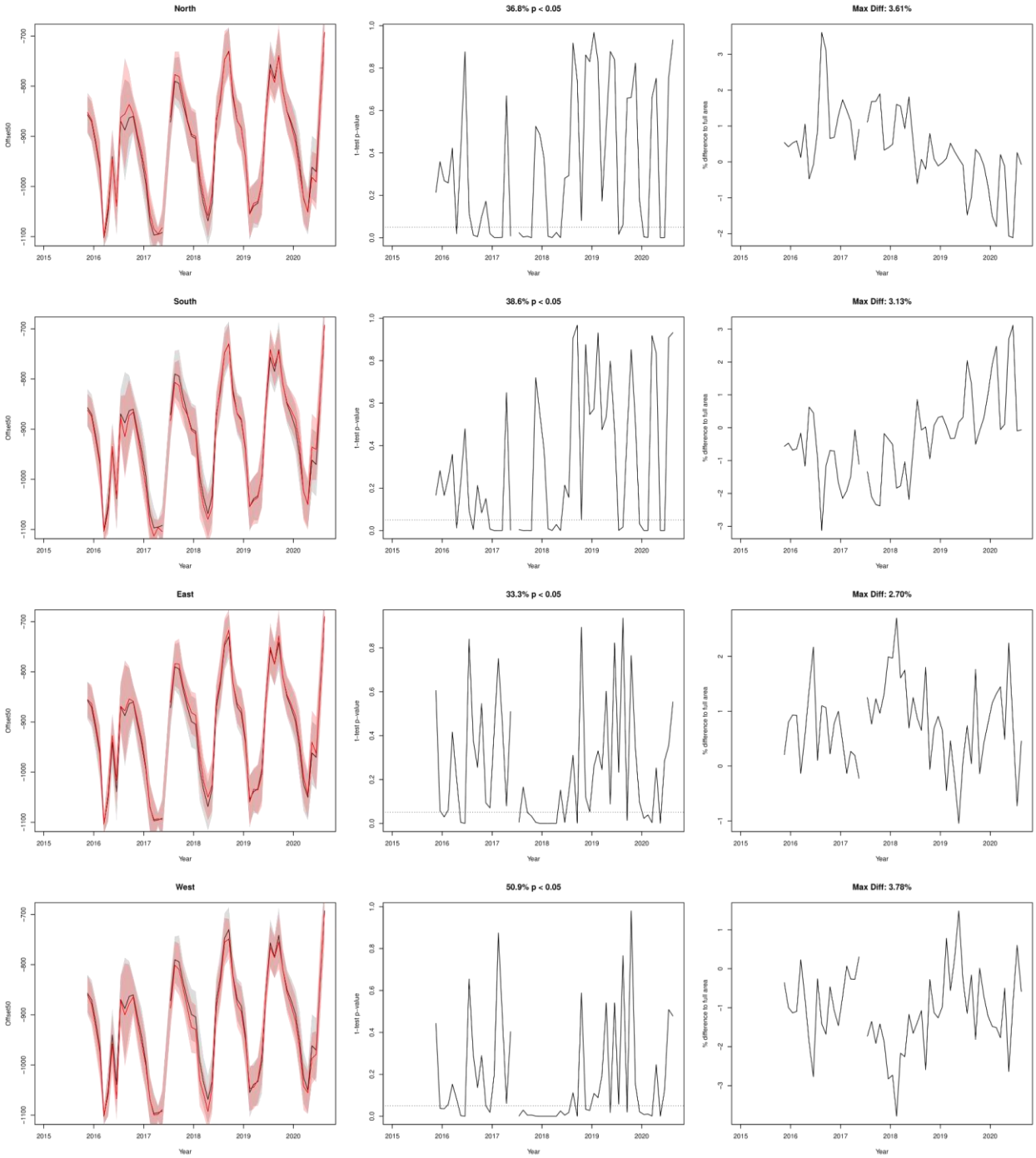

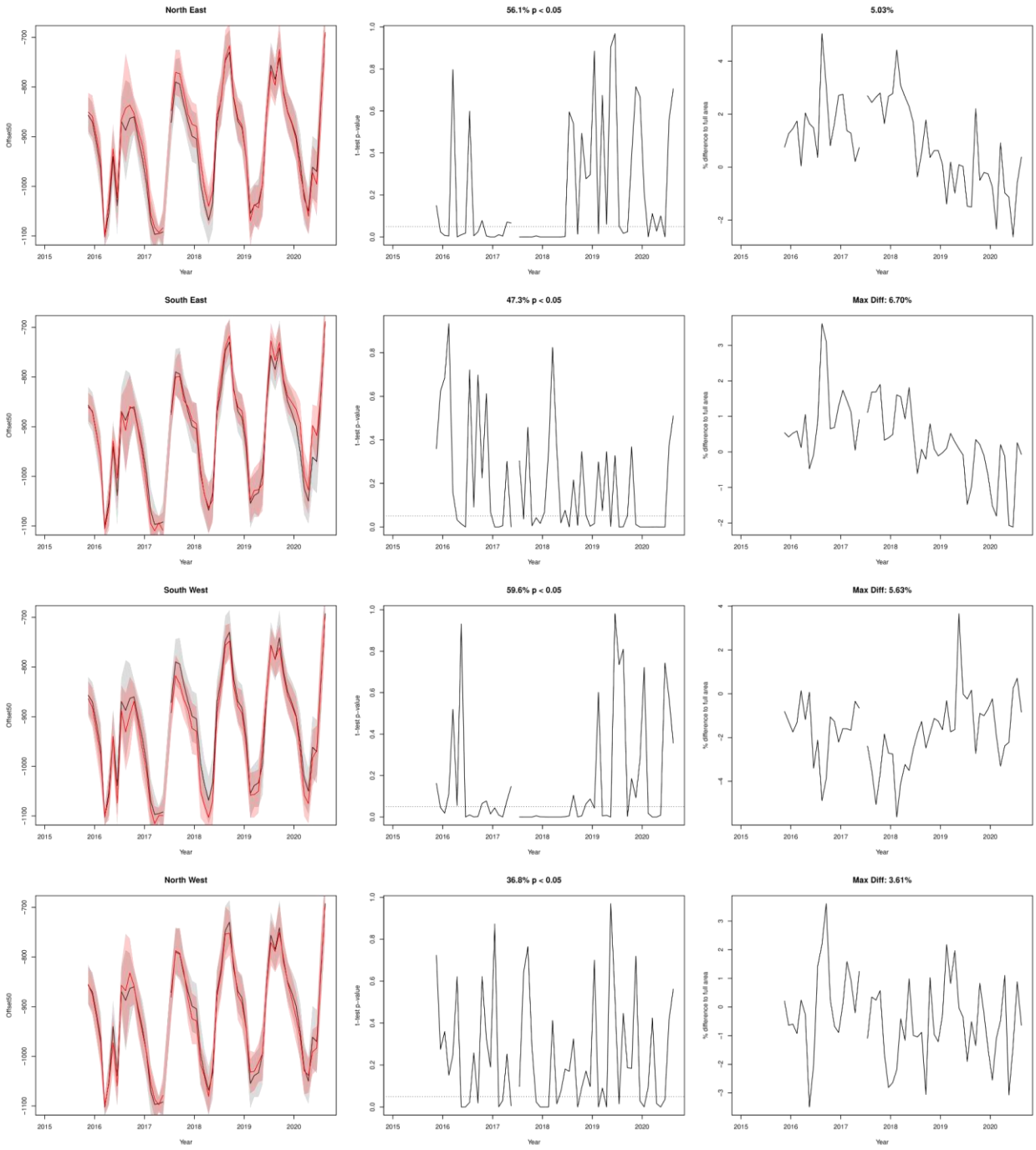

Figure B.1: Test of site size on Offset50 metric. In order to test the impact of the size of the site upon the Offset50 metric, we considered a site which had full coverage of patterned vegetation (ID:00). In this analysis, we divide the site in half horizontally, then further separate these into four quadrants (NE, SE, SW, NW). We then proceed with the analysis for each of these 8 subsections. Column 1 shows the time series for each subregion (red) with

the time series for the whole of the image (black). We can see that this trend is similar, with a similar standard deviation. The middle column shows the p-values for t-test comparisons between the sub-region and the whole image, with a significance value of p=0.05 shown with a horizontal bar. The last column shows the percentage difference between the subregion and the whole image, with the maximum (absolute) difference recorded above. This analysis shows that the size of the region selected does not seem to have a significant effect upon the trend of the Offset50 value, and we hypothesise that any variations are due to heterogeneity of the patterned vegetation.

Image Classifier Results

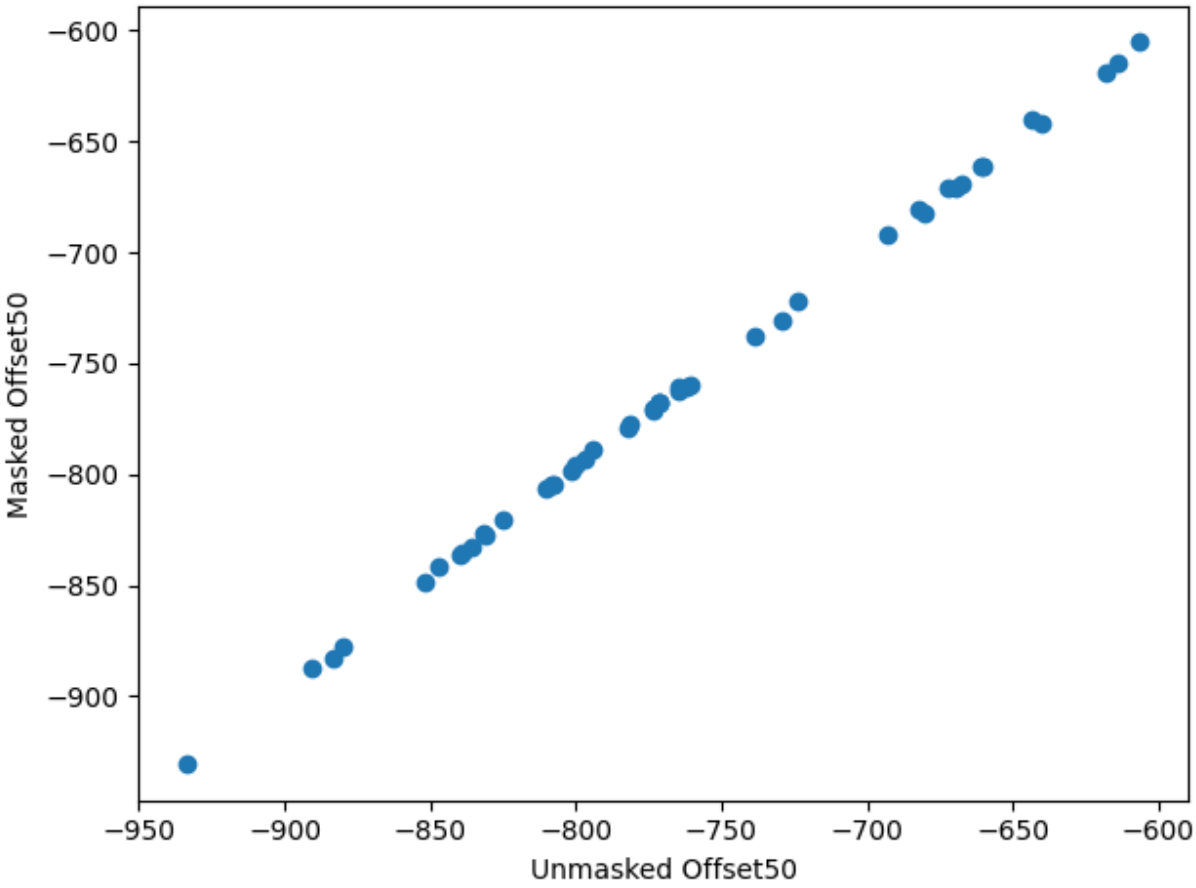

Figure B.2: Test of masking out non-patterned vegetation in heterogenous sites. To test the utility of masking non-patterned vegetation in heterogeneous sites, we had three of the co-authors manually classify all 289 sub-images of an image of a heterogenous site (ID:04). This image was selected as it had little cloud cover, heterogeneous vegetation coverage and was shortly after a rainy season, so had high vegetation coverage. If any of the sub-images were classified as not patterned vegetation by any of the classifiers, i.e. as bare soil or complete vegetation, then they were removed from every image in the series. We then compare the Offset50 values of the masked and unmasked time series above. From this we can see that there is little difference in the values from the manual classification. This is likely due to the

workflow which automatically removes non-patterned vegetation sub-images from the time series and reinforces the utility of this approach.

Spot-labyrinth DEM

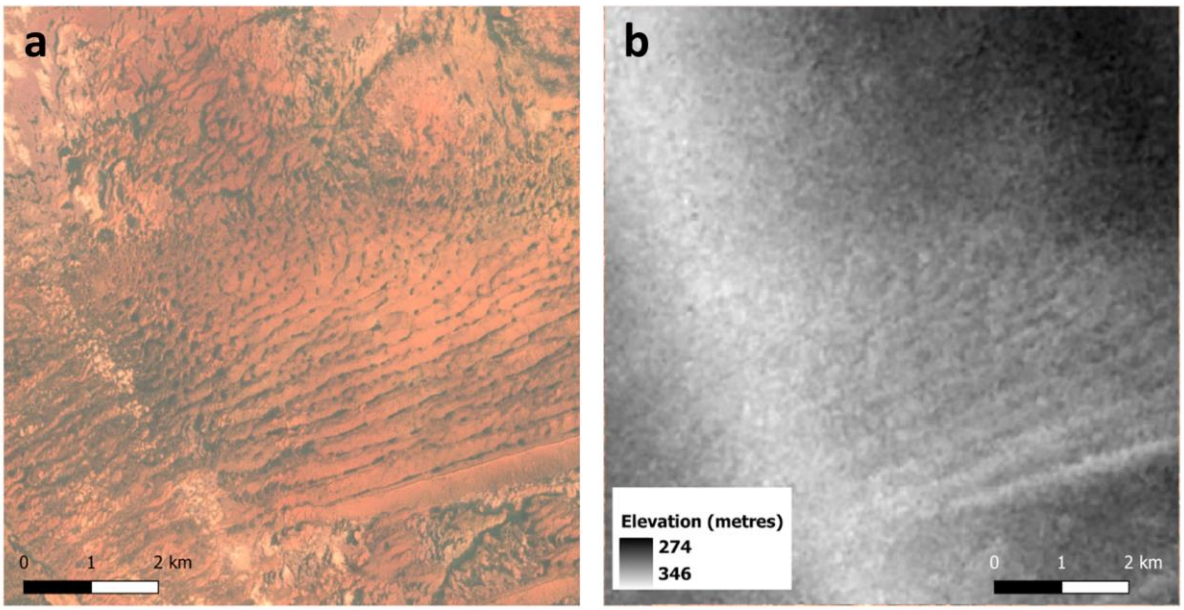

Figure B.3: Spot-labyrinth pattern vegetation site (ID:26) (a) Sentinel-2 RGB image of site from 09-2018. (b) Elevation of the same site. This shows the lower altitude of the channels within which vegetation grows following the rain season. Elevation data from NASA SRTM Digital Elevation Model 30m.

Outlier sites

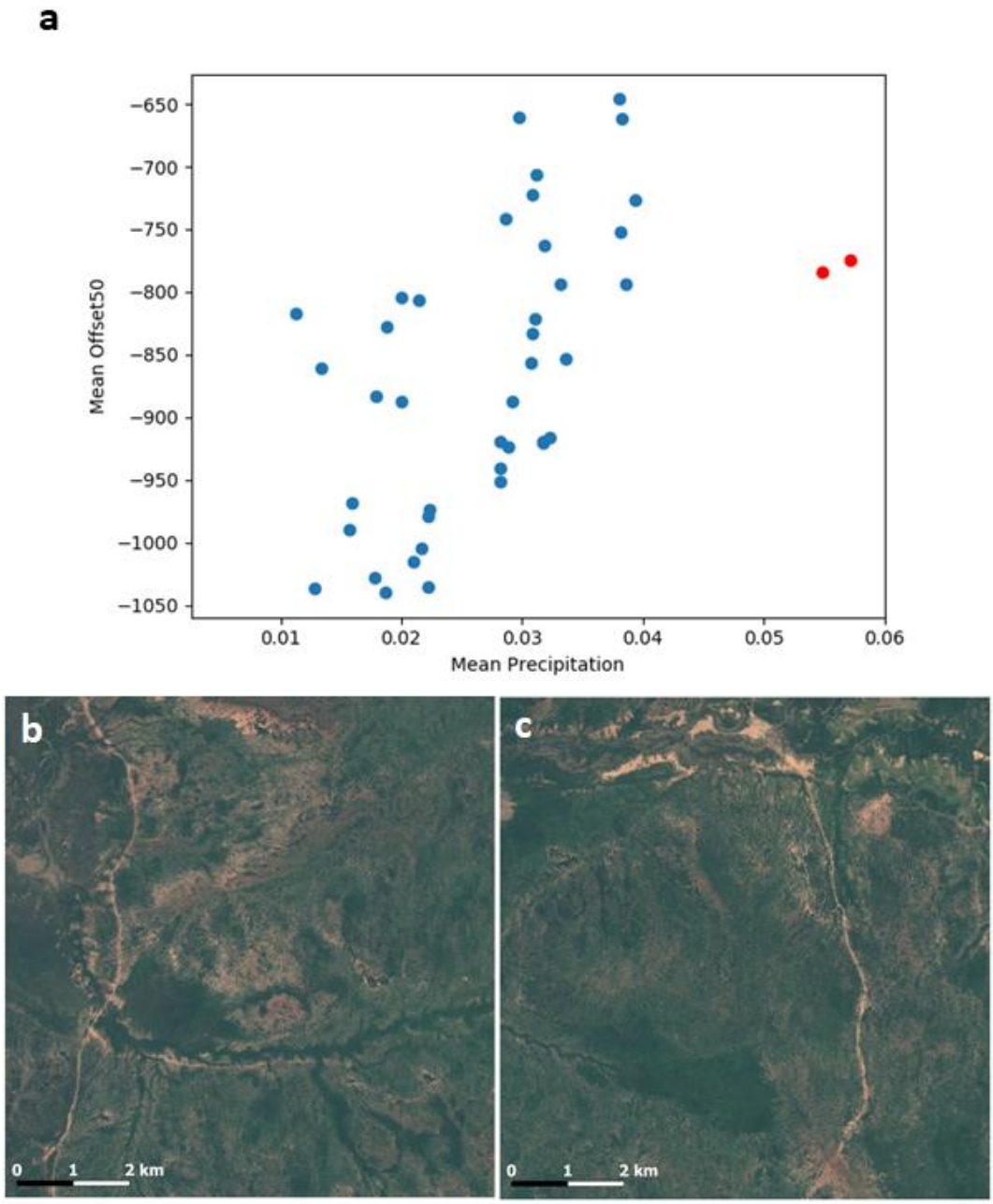

Figure B.4: (a) Mean Offset50 compared with mean precipitation across all sites. Outlier sites shown in red, these prompted further investigation as is detailed below. (b) Sentinel-2 images of outlier sites with (i) ID 46 and (ii) ID 47. These were removed as upon closer inspection, the gaps pattern vegetation were over a small area and the size of the gaps was insufficient to be regularly measured.

Mean Offset50 and NDVI

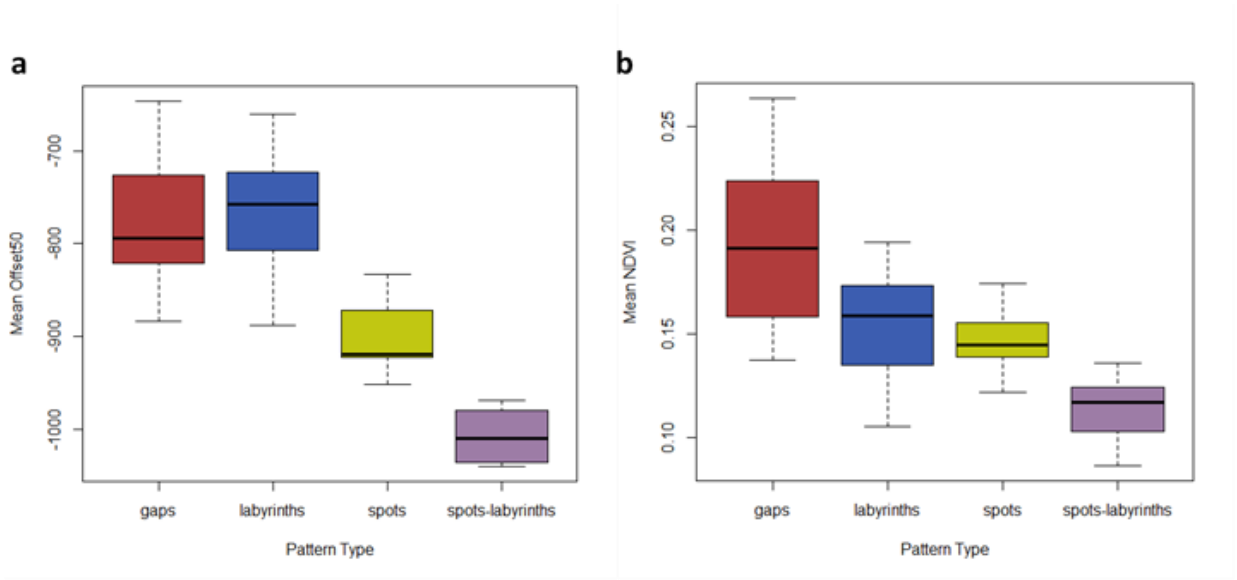

Figure B.5: Pattern vegetation sites separated into classes, displaying boxplots of (a) mean Offset50 and (b) mean NDVI.

Scatter plots

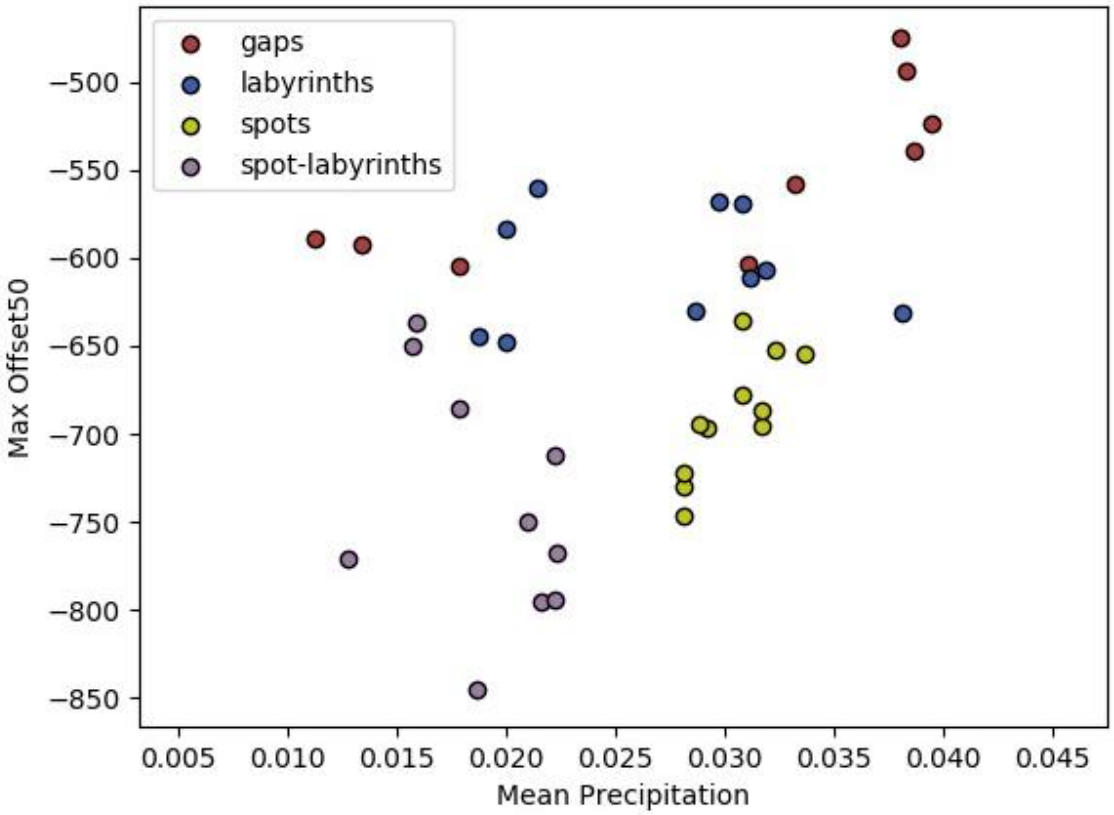

Figure B.6: Scatter plot of mean precipitation and max Offset50 over the course of the time series for each site. Vegetation pattern morphology is indicated by colour. We can see that for all sites higher precipitation values are associated with higher maximum Offset50 values, with this trend consistently followed in most pattern types.

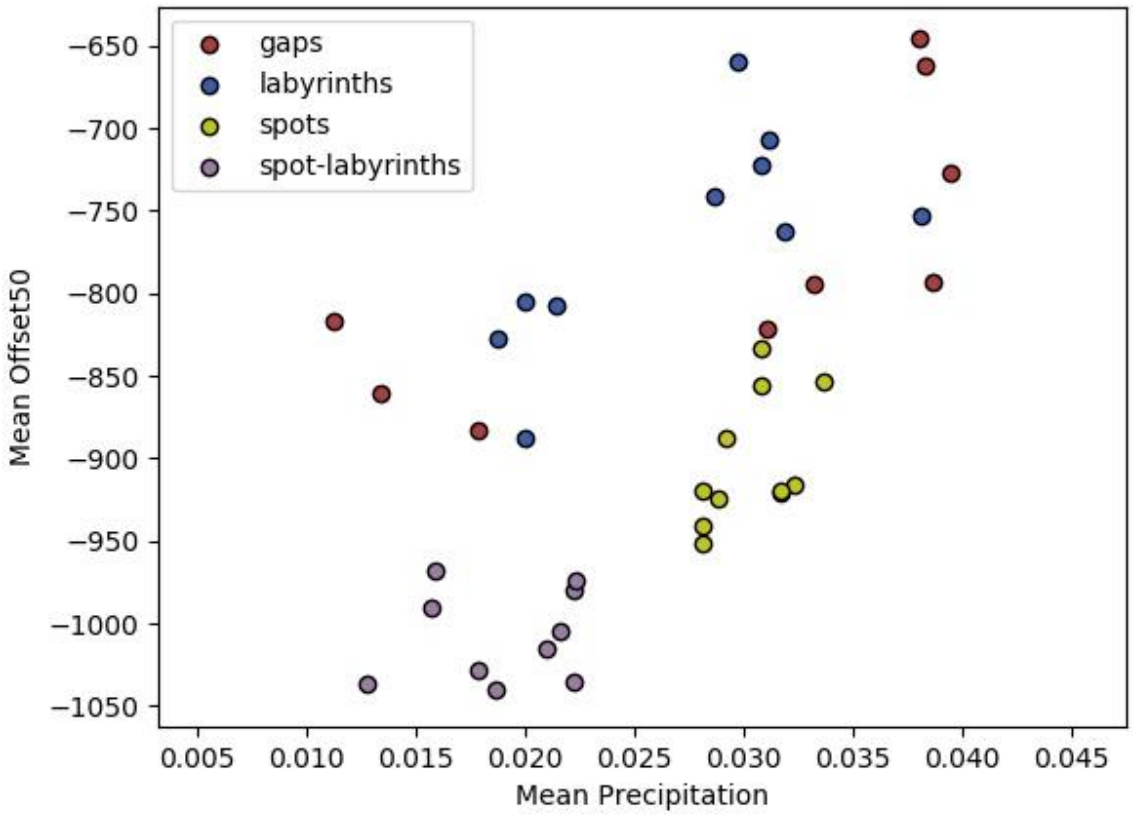

Figure B.7: Scatter plot of mean precipitation and mean Offset50 over the course of the time series for each site. Vegetation pattern morphology is indicated by colour. We can see that higher average precipitation is associated with higher mean Offset50.

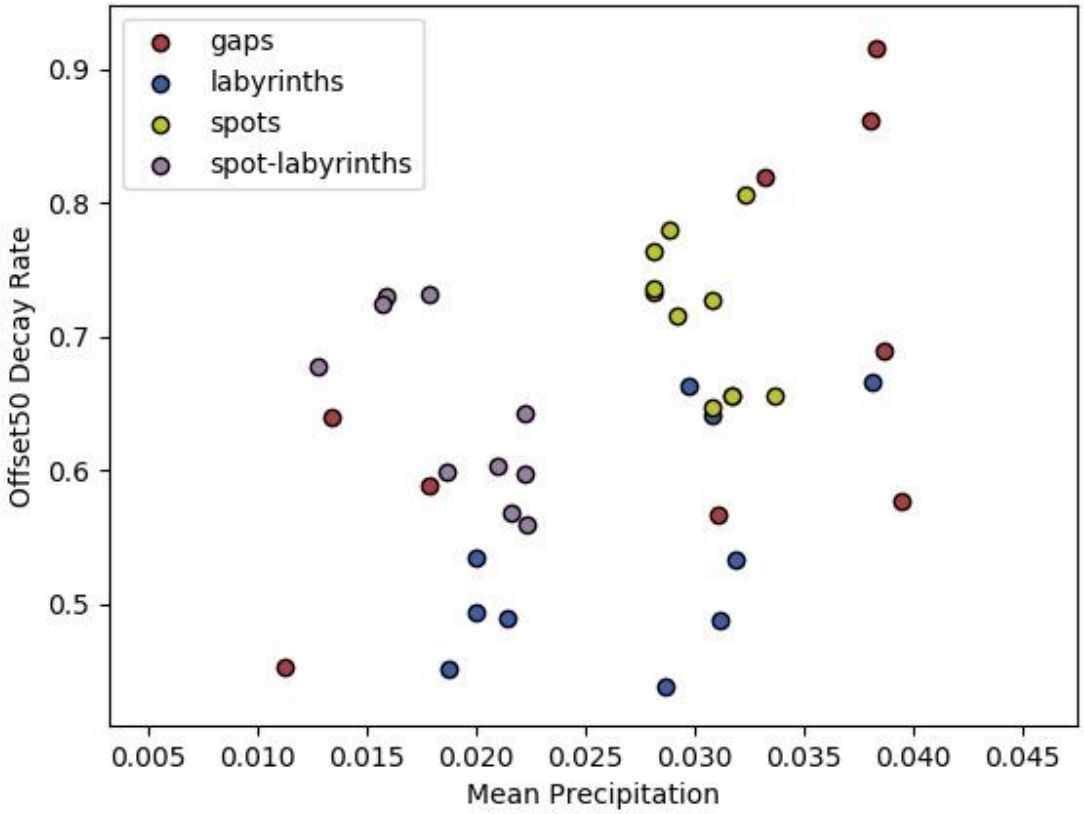

Figure B.8: Scatter plot of mean precipitation and the decay rate of the annual average Offset50. Vegetation pattern morphology is indicated by colour. We can see that higher precipitation values are broadly associated with faster Offset50 decay rates following the rainy season.

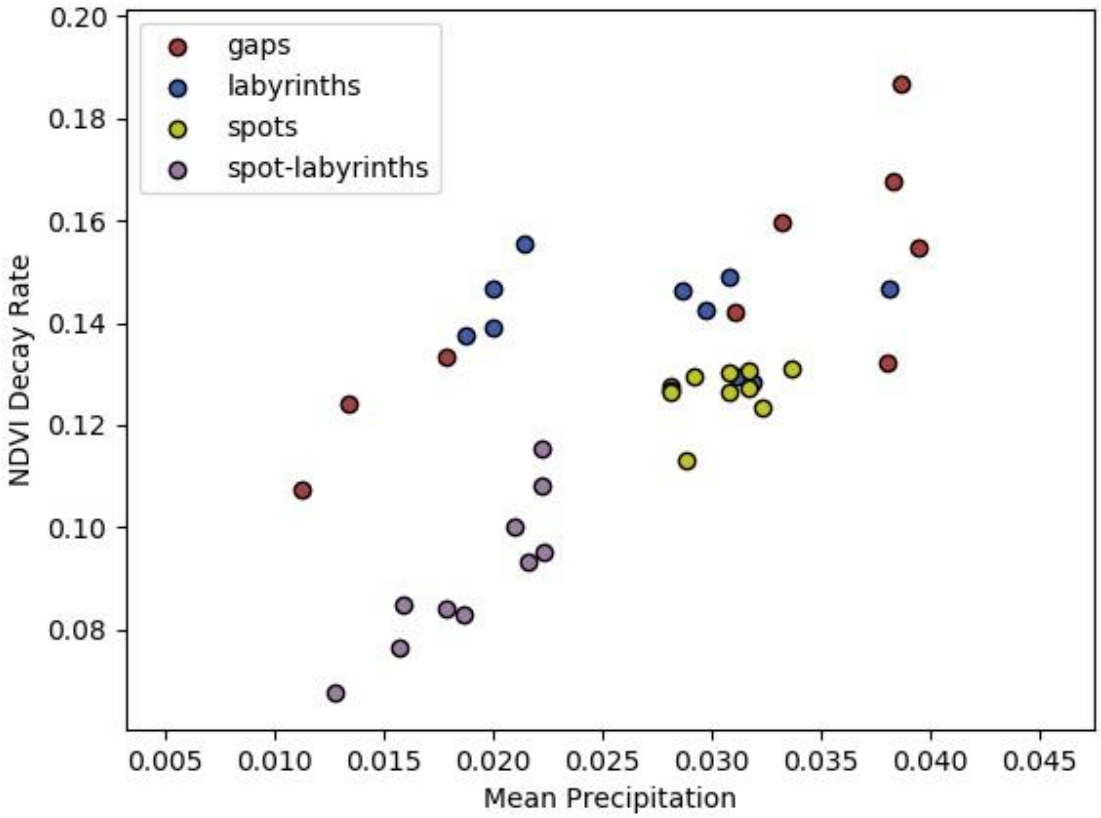

Figure B.9: Scatter plot of mean precipitation and the decay rate of the annual average NDVI. Vegetation pattern morphology is indicated by colour. We can see that higher precipitation values are closely associated with faster NDVI decay rates following the rainy season, this seems especially true for spot-labyrinth vegetation.

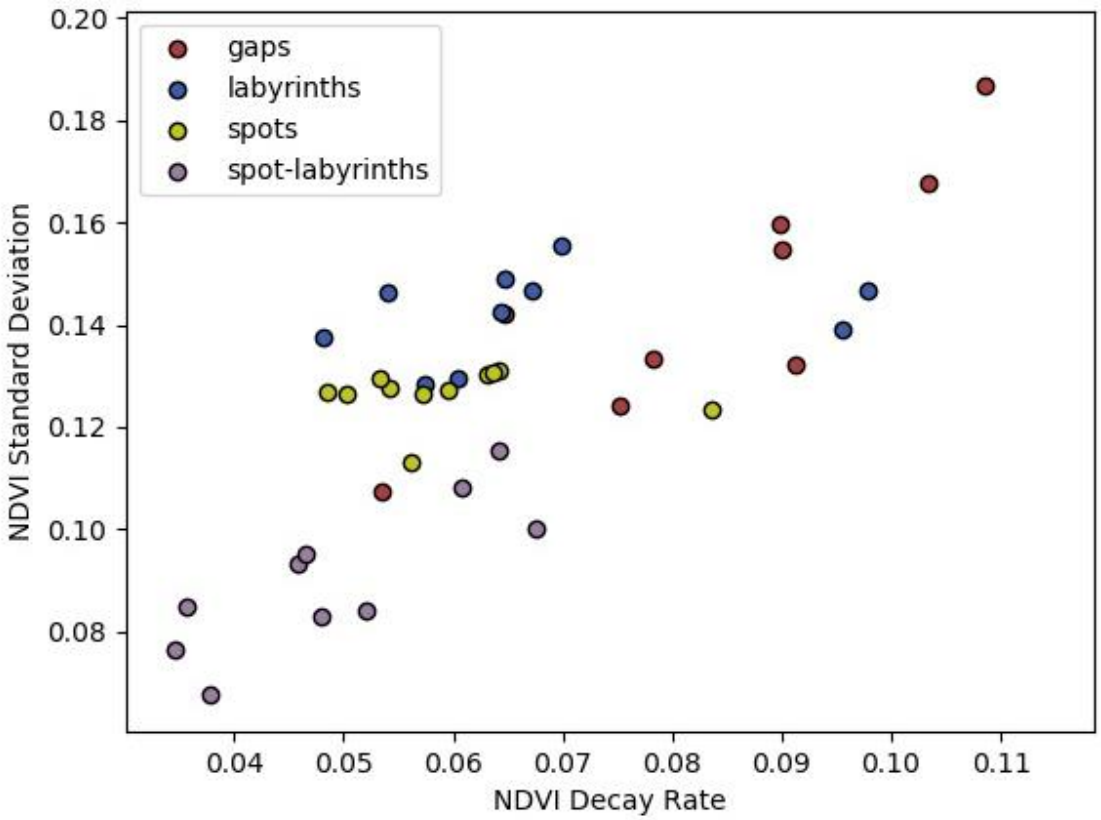

Figure B.10: Scatter plot of NDVI standard deviation and NDVI decay rate. Vegetation pattern morphology is indicated by colour. We can see that the NDVI decay rate is detecting vegetation which rapidly spreads following the rainy season, however this dies away quickly. This is shown through the high standard deviation in sites with higher decay rates.

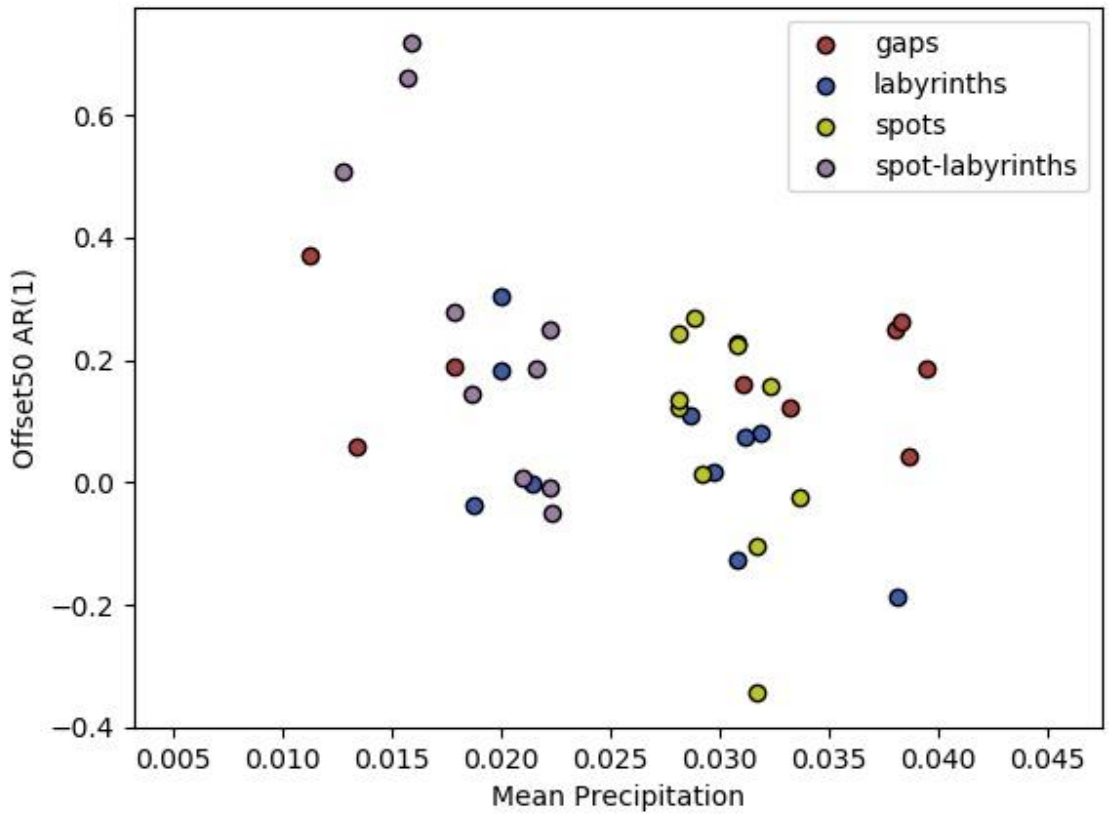

Figure B.11: Scatter plot of mean precipitation and Offset50 AR(1). Vegetation pattern morphology is indicated by colour. We can see that higher precipitation values are broadly associated with lower Offset50 AR(1) values, therefore these sites are more resilient.

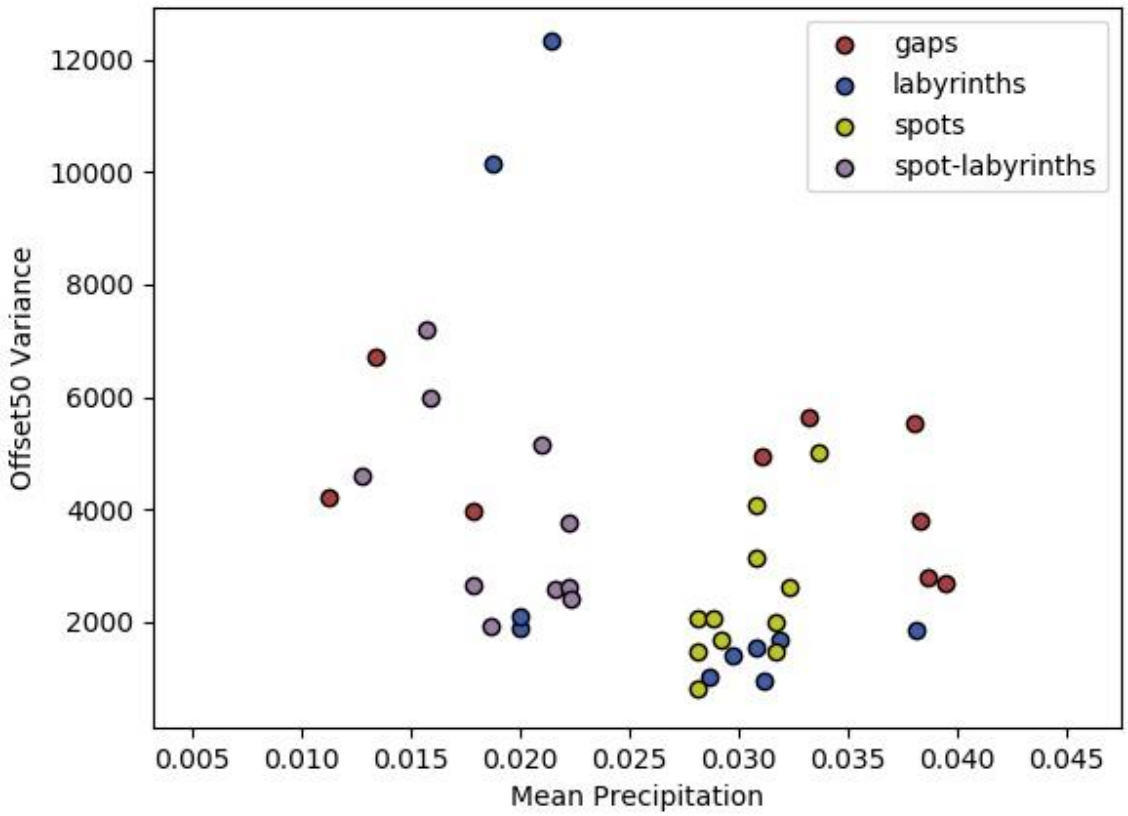

Figure B.12: Scatter plot of mean precipitation and Offset50 variance. Vegetation pattern morphology is indicated by colour. We can see that higher precipitation values are broadly associated with lower Offset50 variance values, therefore these sites are more resilient.

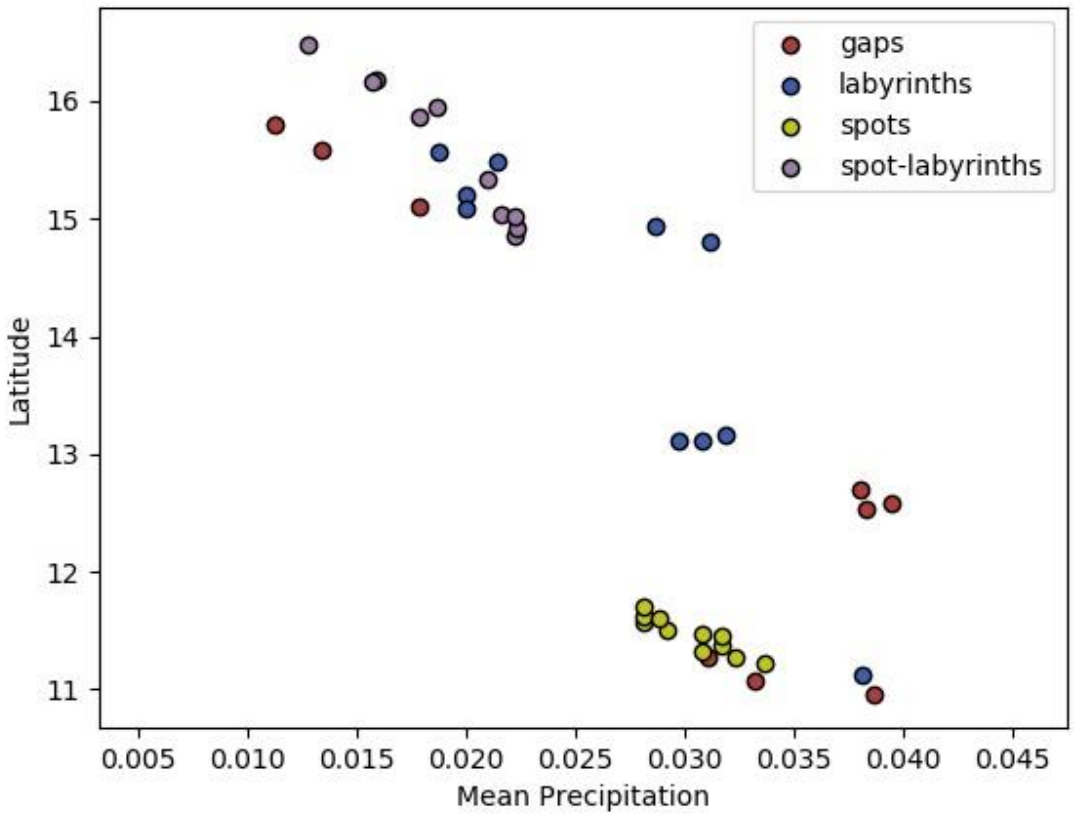

Figure B.13: Scatter plot of latitude and mean precipitation across all sites included in the study. We can see that more northern sites display a lower average rainfall.

Lagged correlation clustering

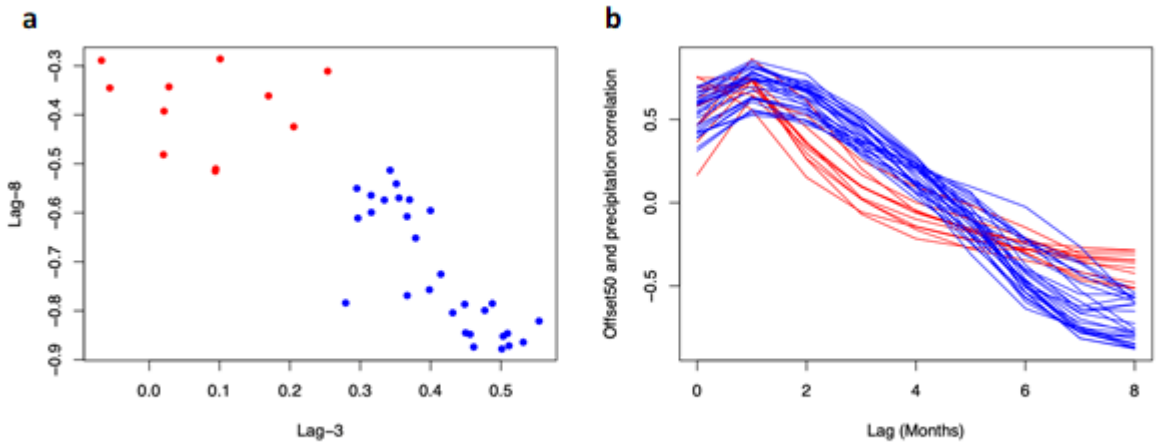

Figure B.14: (a) Cluster analysis of lagged correlation between Offset50 and precipitation across all sites. In order to disentangle the two apparent trends, we use a k-mean clustering algorithm (MacQueen, 1967) with the data points at lag-3 and lag-8. This reveals two distinct clusters which are shown in red and blue, with the correlation trends shown in (b). The blue clustering is composed of almost exclusively spot-labyrinth patterned vegetation.

NDVI and Offset50 Trend Analysis

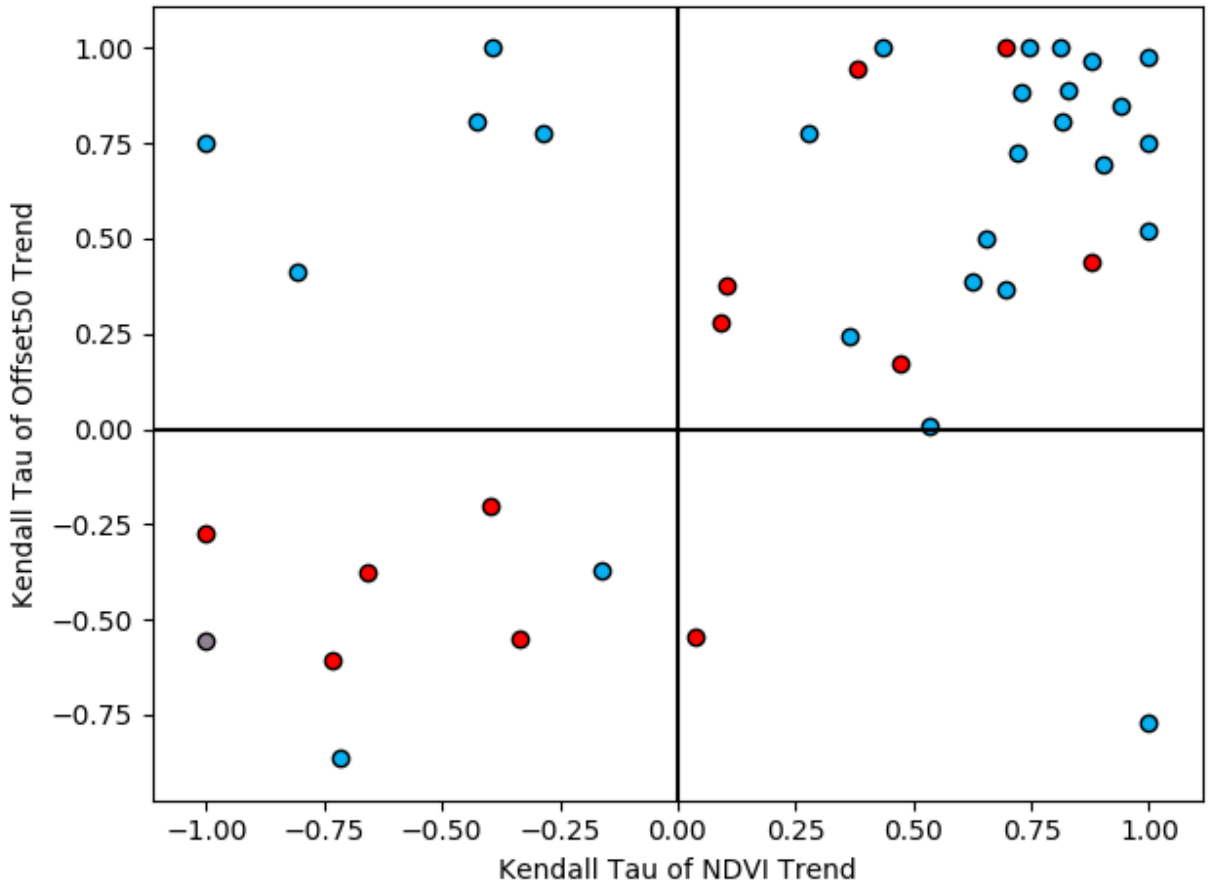

Figure B.15: Analysis of trend in NDVI and Offset50 across all sites. We conduct an STL decomposition of the Offset50, NDVI and precipitation time series for each site between 2016-2019. This reveals the underlying trend of the data. Following this we calculate the Mann-Kendall tau value of this trend to provide a numerical component. This scatter plot shows the trend among Kendall Tau values of the trend component of the NDVI and Offset50 time series of each site. The color of the scatter points corresponds to the precipitation trend of the site, with blue representing an increasing trend, red representing a decreasing trend and grey representing no trend.

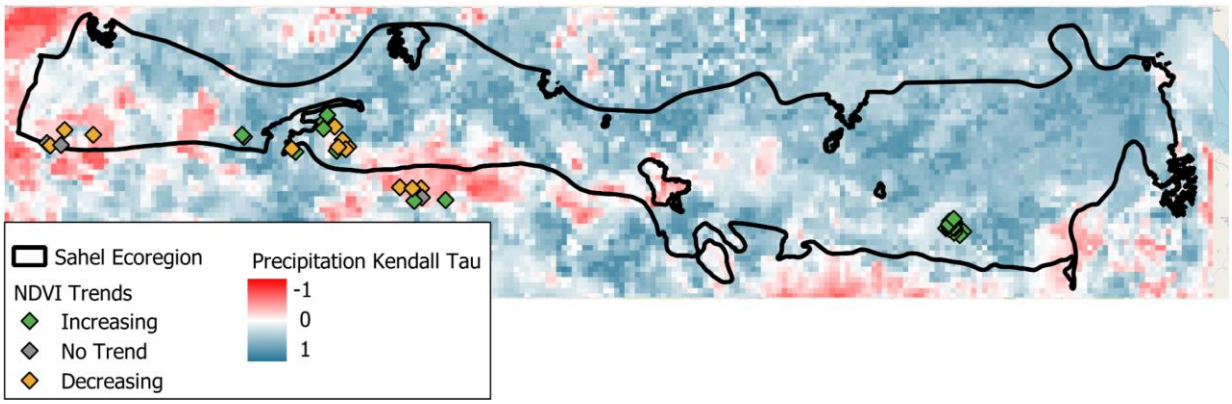

Figure B.16: ERA5 Precipitation trends from 2016-2019 in the Sahel ecoregion. These trends are calculated by taking monthly averages, removing the seasonal trend by subtracting a multi-annual monthly average, then taking a moving average, before the Kendall Tau of each pixel is calculated. Also shown are the NDVI trends of each site.

Supplementary Tables

Table B.1: Table of patterned vegetation sites which were removed from the analysis at various stages. The location and reason for the removal of each site is given within the table.

ID	Country	Lat	Long	Type	Source	Reason for removal
10	Kenya	0.43	40.3	Spots	Deblauwe *et al.* (2008)	Ineligible due to two rainy seasons. Lots of cloud cover.
11	Somalia	8.09	47.44	Labyrinths	Boaler and Hodge (1964)	Ineligible due to two rainy seasons.
15	Burkina Faso	14.91	-0.66	Unclear	Leprun (1999)	Unclear patterned vegetation type, very large scale.
17	Mali	15.23	-0.97	Unclear	Leprun (1999)	Unclear patterned vegetation type, very large scale. Data quality was suboptimal.
19	Mali	15.14	-1.56	Unclear	Trichon *et al.* (2018)	Unclear patterned vegetation type and poor coverage.
22	Mali	15.14	-1.16	Unclear	Leprun (1999)	Unclear patterned vegetation type.
24	Mali	16.25	-1.83	Unclear	Deblauwe *et al.* (2008) (by inspection)	Unclear patterned vegetation type.

37	Somalia	9.34	48.64	Labyrinths	Boaler and Hodge (1964)	Ineligible due to two rainy seasons.
38	Somalia	9.63	47.93	Labyrinths	Boaler and Hodge (1964)	Ineligible due to two rainy seasons.
39	Somalia	9.98	48.44	Labyrinths	Boaler and Hodge (1964)	Ineligible due to two rainy seasons.
40	Somalia	4.64	43.26	Labyrinths	Riché and Ségalen, (1971)	Ineligible due to two rainy seasons. Lots of cloud cover.
41	Ethiopia	4.69	43.21	Gaps	Riché and Ségalen, (1971)	Ineligible due to two rainy seasons. Lots of cloud cover.
42	Ethiopia	7.43	42.90	Labyrinths	Deblauwe *et al.* (2008)	Ineligible due to two rainy seasons.
43	Kenya	0.96	40.37	Gaps	Deblauwe *et al.* (2008)	Ineligible due to two rainy seasons.
46	Chad	12	19.99	Gaps	Deblauwe *et al.* (2008)	Outlier with too little patterned vegetation, and the vegetation patterning is small.

47	Chad	12.05	20.08	Gaps	Deblauwe *et al.* (2008)	Outlier with too little patterned vegetation, and the vegetation patterning is small.

Table B.2: P-values following a Mann-Whitney U-test on max Offset50 values for vegetation pattern classes.

Pattern type	**Gaps**	**Labyrinths**	**Spots**	**Spot-labyrinths**
Gaps	N/A	0.00998	9.85E-05	0.00014
Labyrinths	0.00998	N/A	0.000109	0.000165
Spots	9.85E-05	0.000109	N/A	0.04224
Spot-labyrinths	0.00014	0.000165	0.04224	N/A

Table B.3: P-values following a Mann-Whitney U-test on max NDVI values for vegetation pattern classes.

NDVI Max	**Gaps**	**Labyrinths**	**Spots**	**Spot-Labyrinths**
Gaps	N/A	0.00998	0.00119	0.001874
Labyrinths	0.00998	N/A	0.3493	0.3116
Spots	0.00119	0.3493	N/A	0.3493
Spot-Labyrinths	0.001874	0.3116	0.3493	N/A

Table B.4: Pearson's correlation values for Offset50-precip correlation, Offset50 decay rate correlations, and AR(1) + Variance correlations.

Pearson's correlation coefficient	Offset50 Max	Offset50 Mean	Mean precipitation	Mean historic precipitation	Offset50 decay rate	Offset50 AR(1)	Offset50 Variance	Latitude	Longitude
Offset50 Max	1	0.8613	0.4122	0.3466	0.0962	0.0048	0.2510	-0.2052	-0.1043
Offset50 Mean	0.8613	1	0.5972	0.4647	-0.0289	-0.2438	-0.0052	-0.3343	-0.0028
Mean precipitation	0.4122	0.5972	1	0.8780	0.3794	-0.4309	-0.3410	-0.8404	0.6518
Mean historic precipitation	0.3466	0.4647	0.8780	1	0.3711	-0.4595	-0.2965	-0.9481	0.8055
Offset50 decay rates	0.0962	-0.0289	0.3794	0.3711		0.2115	-0.0999	-0.4902	0.5219
Offset50 AR(1)	0.0048	-0.2438	-0.4309	-0.4595	0.2115	1	0.1918	0.4020	-0.2854
Offset50 Variance	0.2510	-0.0052	-0.3410	-0.2965	-0.0999	0.1918	1	0.3388	-0.2663
Latitude	-0.2052	-0.3343	-0.8404	-0.9481	-0.4902	0.4020	0.3388	1	-0.9051
Longitude	-0.1043	-0.0028	0.6518	0.8055	0.5219	-0.2854	-0.2663	-0.9051	1

Table B.5: Pearson's correlation p-values for Offset50-precip correlation, Offset50 decay rate correlations, and AR(1) + Variance correlations.

p-value	Offset50 Max	Offset50 Mean	Mean precipitation	Mean historic precipitation	Offset50 decay rate	Offset50 AR(1)	Offset50 Variance	Latitude	Longitude
Offset50 Max	0	0	0.0082	0.0284	0.555	0.9768	0.1182	0.2039	0.5217
Offset50 Mean	0	0	0	0.0025	0.8593	0.1295	0.9747	0.035	0.9862
Mean precipitation	0.0082	0	0	0	0.0158	0.0055	0.0313	0	0
Mean historic precipitation	0.0284	0.0025	0	0	0.0184	0.0029	0.0632	0	0
Offset50 decay rates	0.555	0.8593	0.0158	0.0184	0	0.1901	0.5396	0.0013	0.0006
Offset50 AR(1)	0.9768	0.1295	0.0055	0.0029	0.1901	0	0.2358	0.0101	0.0743
Offset50 Variance (0.99 rolling window)	0.1182	0.9747	0.0313	0.0632	0.5396	0.2358	0	0.0325	0.0967
Latitude	0.2039	0.035	0	0	0.0013	0.0101	0.0325	0	0
Longitude	0.5217	0.9862	0	0	0.0006	0.0743	0.0967	0	0

Table B.6: Pearson's correlation values for NDVI decay rate compared with other NDVI variables for all patterned vegetation sites.

Pearson's correlation coefficient	NDVI Max	NDVI Mean	Mean precipitation	Mean historic precipitation	NDVI decay rates	NDVI AR(1)	NDVI Variance	Latitude	Longitude
NDVI Max	1	0.8371	0.3571	0.3504	0.5618	0.0180	0.4971	-0.2158	-0.0713
NDVI Mean	0.8371	1	0.6688	0.5965	0.7338	-0.1914	0.1238	-0.4556	0.1118
Mean precipitation	0.3571	0.6688	1	0.8780	0.6758	-0.2350	-0.3763	-0.8404	0.6518
Mean historic precipitation	0.3504	0.5965	0.8780	1	0.7018	-0.1176	-0.3034	-0.9481	0.8055
NDVI decay rates	0.5618	0.7338	0.6758	0.7018	1	-0.1234	-0.0456	-0.5572	0.2583
NDVI AR(1)	0.0180	-0.1914	-0.2350	-0.1176	-0.1234	1	0.3781	0.1555	-0.0191
NDVI Variance	0.4971	0.1238	-0.3763	-0.3034	-0.0456	0.3781	1	0.3860	-0.3952
Latitude	-0.2158	-0.4556	-0.8404	-0.9481	-0.5572	0.1555	0.3860	1	-0.9051
Longitude	-0.0713	0.1118	0.6518	0.8055	0.2583	-0.0191	-0.3952	-0.9051	1

Table B.7: P-values for NDVI decay rate compared with other NDVI variables for all patterned vegetation sites.

p-values	NDVI Max	NDVI Mean	Mean precipitation	Mean historic precipitation	NDV decay rates	NDVI AR(1)	NDVI Variance	Latitude	Longitude
NDVI Max	0	0	0.0237	0.0266	0.0002	0.9123	0.0011	0.1811	0.662
NDVI Mean	0	0	0	0	0	0.2369	0.4466	0.0031	0.4921
Mean precipitation	0.0237	0	0	0	0	0.1444	0.0167	0	0
Mean historic precipitation	0.0266	0	0	0	0	0.47	0.057	0	0
NDVI decay rates	0.0002	0	0	0	0	0.448	0.7799	0.0002	0.1075
NDVI AR(1)	0.9123	0.2369	0.1444	0.47	0.448	0	0.0162	0.3379	0.9069
NDVI Variance	0.0011	0.4466	0.0167	0.057	0.7799	0.0162	0	0.0139	0.0116
Latitude	0.1811	0.0031	0	0	0.0002	0.3379	0.0139	0	0
Longitude	0.662	0.4921	0	0	0.1075	0.9069	0.0116	0	0

Bibliography

Abis, B. and Brovkin, V. (2017) 'Environmental conditions for alternative tree-cover states in high latitudes', *Biogeosciences*, 14(3), pp. 511–527. doi: 10.5194/bg-14-511-2017.

Albawi, S., Mohammed, T. A. and Al-Zawi, S. (2018) 'Understanding of a convolutional neural network', *Proceedings of 2017 International Conference on Engineering and Technology, ICET 2017*. IEEE, 2018-Janua, pp. 1–6. doi: 10.1109/ICEngTechnol.2017.8308186.

Alibakhshi, S. *et al.* (2017) 'Remotely-sensed early warning signals of a critical transition in a wetland ecosystem', *Remote Sensing*, 9(4). doi: 10.3390/rs9040352.

Armstrong McKay, D. I. *et al.* (2021) 'Updated assessment suggests > 1 . 5 ° C global warming could trigger multiple climate tipping points', *Preprint*, pp. 1–80.

Ashwin, P. *et al.* (2012) 'Tipping points in open systems: Bifurcation, noise-induced and rate-dependent examples in the climate system', *Philosophical Transactions of the Royal Society A: Mathematical, Physical and Engineering Sciences*, 370(1962), pp. 1166–1184. doi: 10.1098/rsta.2011.0306.

Audry, P. and Rossetti, C. (1962) 'Observations sur les sols et la végétation en Mauritanie du sud-est et sur la bordure adjacente du Mali (1959 et 1961)', *Prospection écologique : études en Afrique occidentale. FAO*.

Barbier, N. *et al.* (2006) 'Self-organized vegetation patterning as a fingerprint of climate and human impact on semi-arid ecosystems', *Journal of Ecology*, 94(3), pp. 537–547. doi: 10.1111/j.1365-2745.2006.01126.x.

Barlow, N. *et al.* (2020) 'pyveg: A Python package for analysing the time evolution of patterned vegetation using Google Earth Engine', *Journal of Open Source Software*, 5(55), p. 2483. doi: 10.21105/joss.02483.

Beegle, K. and Christiaensen, L. (2019) *Accelerating Poverty Reduction in Africa*. World Bank Publications. Available at: https://books.google.co.uk/books?id=NPe0DwAAQBAJ.

van Belzen, J. *et al.* (2017) 'Vegetation recovery in tidal marshes reveals critical slowing down under increased inundation', *Nature Communications*, 8, p. 15811. doi: 10.1038/ncomms15811.

Boaler, S. B. and Hodge, C. A. H. (1964) 'Observations on Vegetation Arcs in the Northern Region , Somali Republic', *British Ecological Society*, 52(3), pp. 511–544.

Boers, N. (2021) 'Observation-based early-warning signals for a collapse of the Atlantic Meridional Overturning Circulation', *Nature Climate Change*. Springer US, 11(8), pp. 680–688. doi: 10.1038/s41558-021-01097-4.

Boers, N. and Rypdal, M. (2021) 'Critical slowing down suggests that the western Greenland Ice Sheet is close to a tipping point', *Proceedings of the National Academy of Sciences*

of the United States of America, 118(21), pp. 1–7. doi: 10.1073/pnas.2024192118.

Borish, D., King, N. and Dewey, C. (2017) 'Enhanced community capital from primary school feeding and agroforestry program in Kenya', *International Journal of Educational Development*. Elsevier Ltd, 52, pp. 10–18. doi: 10.1016/j.ijedudev.2016.10.005.

Boulton, C. A., Allison, L. C. and Lenton, T. M. (2014) 'Early warning signals of atlantic meridional overturning circulation collapse in a fully coupled climate model', *Nature Communications*. Nature Publishing Group, 5(Level 7), pp. 1–9. doi: 10.1038/ncomms6752.

Boulton, C. A., Booth, B. B. B. and Good, P. (2017) 'Exploring uncertainty of Amazon dieback in a perturbed parameter Earth system ensemble', *Global Change Biology*, 23(12), pp. 5032–5044. doi: 10.1111/gcb.13733.

Boulton, C. A., Lenton, T. M. and Boers, N. (2022) 'Pronounced loss of Amazon rainforest resilience since the early 2000s', *Nature Climate Change*. Springer US, 12(March). doi: 10.1038/s41558-022-01287-8.

Bury, T. M. *et al.* (2021) 'Deep learning for early warning signals of tipping points', *Proceedings of the National Academy of Sciences of the United States of America*, 118(39). doi: 10.1073/pnas.2106140118.

Buxton, J. *et al.* (2021) 'Community-driven tree planting greens the neighbouring landscape', *Scientific Reports*. Nature Publishing Group UK, 11(1), pp. 1–9. doi: 10.1038/s41598-021-96973-6.

Buxton, J. E. *et al.* (2022) 'Quantitatively monitoring the resilience of patterned vegetation in the Sahel', *Global Change Biology*, 28(2), pp. 571–587. doi: 10.1111/gcb.15939.

CAAC (2020) *Monitoring Report For TIST Program in Kenya. VCS-009, Verification 03.*

Cai, B. and Yu, R. (2009) 'Advance and evaluation in the long time series vegetation trends research based on remote sensing', *Journal of Remote Sensing*, 4619(6), pp. 1170–1186.

Campbell, J. B. and Wynne, R. H. (2011) *Introduction to remote sensing*. Guildford Press.

Carlson, T.N. and Ripley, D.A., (1997). On the relation between NDVI, fractional vegetation cover, and leaf area index. *Remote sensing of Environment*, *62*(3), pp.241-252

Carpenter, S. R. *et al.* (2011) 'Early Warnings of Regime Shifts : A Whole-Ecosystem Experiment', 157(May), pp. 1079–1083.

Carpenter, S. R. and Brock, W. A. (2006) 'Rising variance : a leading indicator of ecological transition', pp. 311–318. doi: 10.1111/j.1461-0248.2005.00877.x.

Cavanaugh, K. C. *et al.* (2010) 'Scaling giant kelp field measurements to regional scales using

satellite observations', *Marine Ecology Progress Series*, 403, pp. 13–27. doi: 10.3354/meps08467.

Charney, B. J. G. (1975) 'Dynamic of deserts and drought in the Sahel', 101(March 1974).

Chen, Y. *et al.* (2015) 'Patterned vegetation, tipping points, and the rate of climate change', *European Journal of Applied Mathematics*, 26(6), pp. 945–958. doi: 10.1017/S0956792515000261.

Chisholm, R. A. and Filotas, E. (2009) 'Critical slowing down as an indicator of transitions in two-species models', 257, pp. 142–149. doi: 10.1016/j.jtbi.2008.11.008.

Clements, C. F. *et al.* (2017) 'Body size shifts and early warning signals precede the historic collapse of whale stocks', *Nature Ecology and Evolution*, 1(7), pp. 1–6. doi: 10.1038/s41559-017-0188.

Clements, C. F., McCarthy, M. A. and Blanchard, J. L. (2019) 'Early warning signals of recovery in complex systems', *Nature Communications*. Springer US, 10(1). doi: 10.1038/s41467-019-09684-y.

Couteron, P. (2002) 'Quantifying change in patterned semi-arid vegetation by Fourier analysis of digitized aerial photographs', *International Journal of Remote Sensing*, 23(17), pp. 3407–3425. doi: 10.1080/01431160110107699.

Cracknell, A. P. (1997) *Advanced very high resolution radiometer AVHRR*. Crc Press.

Crutzen, P. J. (2006) 'The " Anthropocene "', in *Earth system science in the Anthropocene*. Berlin: Springer, pp. 13–18.

Cunliffe, A. M., Brazier, R. E. and Anderson, K. (2016) 'Ultra-fine grain landscape-scale quantification of dryland vegetation structure with drone-acquired structure-from-motion photogrammetry', *Remote Sensing of Environment*. The Authors, 183, pp. 129–143. doi: 10.1016/j.rse.2016.05.019.

Dai, L. *et al.* (2012) 'Generic indicators for loss of resilience before a tipping point leading to population collapse', *Science*, 336(6085), pp. 1175–1177. doi: 10.1126/science.1219805.

Dakos, V. *et al.* (2008) 'Slowing down as an early warning signal for abrupt climate change', *Proceedings of the National Academy of Sciences*, 105(38), pp. 14308–14312. doi: 10.1073/pnas.0802430105.

Dakos, V. *et al.* (2010) 'Spatial correlation as leading indicator of catastrophic shifts', *Theoretical Ecology*, 3(3), pp. 163–174. doi: 10.1007/s12080-009-0060-6.

Dakos, V. *et al.* (2011) 'Slowing down in spatially patterned ecosystems at the brink of collapse vasilis', *American Naturalist*, 177(6). doi: 10.1086/659945.

Dakos, V. *et al.* (2012) 'Methods for detecting early warnings of critical transitions in time series illustrated using simulated ecological data', *PLoS ONE*, 7(7). doi: 10.1371/journal.pone.0041010.

Dardel, C. *et al.* (2014) 'Re-greening Sahel: 30 years of remote sensing data and field observations (Mali, Niger)', *Remote Sensing of Environment*. Elsevier Inc., 140, pp. 350–364. doi: 10.1016/j.rse.2013.09.011.

Deblauwe, V. *et al.* (2008) 'The global biogeography of semi-arid periodic vegetation patterns', pp. 715–723. doi: 10.1111/j.1466-8238.2008.00413.x.

Dey, R. *et al.* (2019) 'A review of past and projected changes in Australia's rainfall', *Wiley Interdisciplinary Reviews: Climate Change*, 10(3), pp. 1–23. doi: 10.1002/wcc.577.

Dial, G. *et al.* (2003) 'IKONOS satellite, imagery, and products', *Remote Sensing of Environment*, 88(1–2), pp. 23–36. doi: 10.1016/j.rse.2003.08.014.

Dinerstein, E. *et al.* (2017) 'An Ecoregion-Based Approach to Protecting Half the Terrestrial Realm', *BioScience*, 67(6), pp. 534–545. doi: 10.1093/biosci/bix014.

Ditlevsen, P. D. and Johnsen, S. J. (2010) 'Tipping points: Early warning and wishful thinking', *Geophysical Research Letters*, 37(19), pp. 2–5. doi: 10.1029/2010GL044486.

Doso Jnr, S. (2014) 'Land degradation and agriculture in the Sahel of Africa: causes, impacts and recommendations', *Journal of Agricultural Science and Applications*, 03(03), pp. 67–73. doi: 10.14511/jasa.2014.030303.

Drake, J. M. and Griffen, B. D. (2010) 'Early warning signals of extinction in deteriorating environments', *Nature*. Nature Publishing Group, pp. 6–9. doi: 10.1038/nature09389.

Drusch, M. *et al.* (2012) 'Sentinel-2: ESA's Optical High-Resolution Mission for GMES Operational Services', *Remote Sensing of Environment*, 120, pp. 25–36. doi: 10.1016/j.rse.2011.11.026.

Eby, S. *et al.* (2017) 'Alternative stable states and spatial indicators of critical slowing down along a spatial gradient in a savanna ecosystem', *Global Ecology and Biogeography*, 26(6), pp. 638–649. doi: 10.1111/geb.12570.

Eckert, S. *et al.* (2015) 'Trend analysis of MODIS NDVI time series for detecting land degradation and regeneration in Mongolia', *Journal of Arid Environments*. Elsevier Ltd, 113, pp. 16–28. doi: 10.1016/j.jaridenv.2014.09.001.

Eckert, S. *et al.* (2017) 'Agricultural Expansion and Intensification in the Foothills of Mount Kenya : A Landscape Perspective', *Remote Sensing*, 9(8), p. 784. doi: 10.3390/rs9080784.

Estrada, E. and Rodríguez-Velázquez, J. A. (2005) 'Subgraph centrality in complex networks', *Phys. Rev. E*. American Physical Society, 71(5), p. 56103. doi:

10.1103/PhysRevE.71.056103.

Estrada, M. and Corbera, E. (2011) 'The Potential of Carbon Offsetting Projects in the Forestry Sector for Poverty Reduction in Developing Countries', in Ingram, J. C., DeClerck, F., and del Rio, C. (eds) *Integrating Ecology and Poverty Reduction: The Application of Ecology in Development Solutions*. New York, NY: Springer New York, pp. 137–147. doi: 10.1007/978-1-4614-0186-5_11.

FAO (2000) *Africover Multipurpose Land Cover Database for Kenya*. Available at: https://datasets.wri.org/dataset/agricultural-areas-in-kenya (Accessed: 4 June 2020).

Feng, Y. *et al.* (2021) 'Reduced resilience of terrestrial ecosystems locally is not reflected on a global scale', *Communications Earth & Environment*. Springer US, 2(1). doi: 10.1038/s43247-021-00163-1.

Fensholt, R. *et al.* (2013) 'Assessing land degradation/recovery in the african sahel from long-term earth observation based primary productivity and precipitation relationships', *Remote Sensing*, 5(2), pp. 664–686. doi: 10.3390/rs5020664.

Fensholt, R. and Proud, S. R. (2012) 'Evaluation of Earth Observation based global long term vegetation trends — Comparing GIMMS and MODIS global NDVI time series', *Remote Sensing of Environment*. Elsevier Inc., 119, pp. 131–147. doi: 10.1016/j.rse.2011.12.015.

Fischer, W. ., Hemphil, W. . and Kover, A. (1976) 'Progress in Remote Sensing', 32, pp. 33–72.

Gichenje, H. and Godinho, S. (2018) 'Establishing a land degradation neutrality national baseline through trend analysis of GIMMS NDVI Time-series', *Land Degradation & Development*. Land Degradation & Development, 29(9), 29(9), p. pp.2985-2997.

Gichenje, H., Pinto-correia, T. and Godinho, S. (2019) 'Remote Sensing Applications : Society and Environment An analysis of the drivers that affect greening and browning trends in the context of pursuing land degradation-neutrality', *Remote Sensing Applications: Society and Environment*. Elsevier B.V., 15(December 2018), p. 100251. doi: 10.1016/j.rsase.2019.100251.

Giusti, G. De, Kristjanson, P. and Rufino, M. C. (2019) 'Agroforestry as a climate change mitigation practice in smallholder farming : evidence from Kenya'. Climatic Change, pp. 379–394.

Gleason, C. J. and Im, J. (2012) 'Forest biomass estimation from airborne LiDAR data using machine learning approaches', *Remote Sensing of Environment*. Elsevier Inc., 125, pp. 80–91. doi: 10.1016/j.rse.2012.07.006.

Gorelick, N. *et al.* (2017) 'Remote Sensing of Environment Google Earth Engine : Planetary-scale geospatial analysis for everyone', *Remote Sensing of Environment*. The

Author(s), 202, pp. 18–27. doi: 10.1016/j.rse.2017.06.031.

Gowda, K., Iams, S. and Silber, M. (2018) 'Signatures of human impact on self-organized vegetation in the Horn of Africa', *Scientific Reports*. Springer US, 8(1), pp. 1–8. doi: 10.1038/s41598-018-22075-5.

Grimm, V. and Wissel, C. (1997) 'Babel, or the ecological stability discussions: An inventory and analysis of terminology and a guide for avoiding confusion', *Oecologia*, pp. 323–334. doi: 10.1007/s004420050090.

Guttal, V. and Jayaprakash, C. (2008) 'Changing skewness: An early warning signal of regime shifts in ecosystems', *Ecology Letters*, 11(5), pp. 450–460. doi: 10.1111/j.1461-0248.2008.01160.x.

Guttal, V. and Jayaprakash, C. (2009) 'Spatial variance and spatial skewness: Leading indicators of regime shifts in spatial ecological systems', *Theoretical Ecology*, 2(1), pp. 3–12. doi: 10.1007/s12080-008-0033-1.

Hansen, M. C. *et al.* (2013) 'High Resolution Global Maps of 21st-Century Forest Cover Change', *Science*, 342. Available at: http://earthenginepartners.appspot.com/science-2013-global-forest.

Von Hardenberg, J. *et al.* (2010) 'Periodic versus scale-free patterns in dryland vegetation', in *Proceedings of the Royal Society B: Biological Sciences*, pp. 1771–1776. doi: 10.1098/rspb.2009.2208.

Held, H. and Kleinen, T. (2004) 'Detection of climate system bifurcations by degenerate fingerprinting', *Geophysical Research Letters*, 31(23), pp. 1–4. doi: 10.1029/2004GL020972.

Helldén, U. (1991) 'Desertification - time for an assessment?', *Ambio*, 20(8), pp. 372–383.

Henry, M. *et al.* (2009) 'Agriculture , Ecosystems and Environment Biodiversity , carbon stocks and sequestration potential in aboveground biomass in smallholder farming systems of western Kenya', 129, pp. 238–252. doi: 10.1016/j.agee.2008.09.006.

Herrmann, S. M. and Hutchinson, C. F. (2005) 'The changing contexts of the desertification debate', *Journal of Arid Environments*, 63(3), pp. 538–555. doi: 10.1016/j.jaridenv.2005.03.003.

Hersbach, H. *et al.* (2020) 'The ERA5 global reanalysis', *Quarterly Journal of the Royal Meteorological Society*, 146(730), pp. 1999–2049. doi: 10.1002/qj.3803.

HilleRisLambers, R. *et al.* (2001) 'Vegetation pattern formation in semi-arid grazing systems', *Ecology*, 82(1), pp. 50–61. doi: 10.1890/0012-9658(2001)082[0050:VPFISA]2.0.CO;2.

Hirota, M. *et al.* (2011) 'Global Resilience of Tropical Forest', *Science*, 334(October), pp. 232–235.

Holben, B. N. (1986) 'Characteristics of maximum-value composite images from temporal AVHRR data', *International Jounal of Remote Sensing*, 7, pp. 1417–1434. doi: 10.1080/01431168608948945.

Holl, B. N. and Brancalion, P. H. (2020) 'Tree planting is not a simple solution', *Science*, 368(6491), pp. 580–582.

Holling (1973) 'RESILIENCE AND STABILITY OF ECOLOGICAL SYSTEMS', 4(1973), pp. 1–23.

Holling, C. S. (1996) 'Engineering resilience versus ecological resilience', *Engineering Within Ecological Constraints*, 31, pp. 31–43. Available at: https://books.google.co.uk/books?hl=en&lr=&id=qXxOAgAAQBAJ&oi=fnd&pg=PT39&dq=holling+1996+engineering+resilience&ots=lKVgsFGjMu&sig=5QkmXS3xTvfgndikBrHVbhhbmJY&redir_esc=y#v=onepage&q=holling 1996 engineering resilience&f=false (Accessed: 6 December 2021).

Le Houérou, H. N. (1989) *The Grazing Land Ecosystems of the African Sahel*. Springer Berlin Heidelberg (Ecological Studies 75). Available at: https://books.google.co.uk/books?id=YZ%5C_vCAAAQBAJ.

Hudak, A. T. *et al.* (2012) 'Quantifying aboveground forest carbon pools and fluxes from repeat LiDAR surveys', *Remote Sensing of Environment*. Elsevier B.V., 123, pp. 25–40. doi: 10.1016/j.rse.2012.02.023.

Huete, A. R., Liu, H. Q. and van Leeuwen, W. J. D. (1997) 'Use of vegetation indices in forested regions: Issues of linearity and saturation', *International Geoscience and Remote Sensing Symposium (IGARSS)*, 4(1), pp. 1966–1968. doi: 10.1109/igarss.1997.609169.

I4EI (2014) 'USAID Kenya TIST Program Final Performance Report'. Available at: http://www.tist.org/tist/docs/USAID-Documents/I4EI%2520USAID%25%0A20KE%2520140616%2520Final%2520Report%2520140619.pdf.

Iiyama, M. *et al.* (2014) 'The potential of agroforestry in the provision of sustainable woodfuel in sub-Saharan Africa', *Current Opinion in Environmental Sustainability*. Elsevier B.V., 6, pp. 138–147. doi: 10.1016/j.cosust.2013.12.003.

Ilstedt, U. *et al.* (2016) 'Intermediate tree cover can maximize groundwater recharge in the seasonally dry tropics', *Scientific Reports*. Nature Publishing Group, 6(February 2015), pp. 1–12. doi: 10.1038/srep21930.

IPBES (2018) 'The IPBES assessment report on land degradation and restoration.', *Secrateriat of the Intergovernmental Science-Policy Platform on Biodiversity and Ecosystem Services*. doi: 10.5281/ZENODO.3237393.

IPCC (2021) *Climate Change 2021: The Physical Science Basis. Contribution of Working Group*

1 to the Sixth Assessment Report of the Intergovernmental Panel on Climate Change. Cambridge University Press.

Jindal, R., Swallow, B. and Kerr, J. (2008) 'Forestry-based carbon sequestration projects in Africa : Potential benefits and challenges', 32, pp. 116–130.

De Jong, B. H. J., Bazán, E. E. and Montalvo, S. . (2007) 'Application of the "' Climafor '" baseline to determine leakage : the case of Scolel Te', *Mitigation and Adaptation Strategies for Global Change,* 12(6), pp. 1153–1168. doi: 10.1007/s11027-006-9068-z.

de Jong, R. *et al.* (2011) 'Analysis of monotonic greening and browning trends from global NDVI time-series', *Remote Sensing of Environment*. Elsevier Inc., 115(2), pp. 692–702. doi: 10.1016/j.rse.2010.10.011.

Jose, S. (2009) 'Agroforestry for ecosystem services and environmental benefits: an overview', *Agroforestry Systems*, 76(1), pp. 1–10. doi: 10.1007/s10457-009-9229-7.

Kaasalainen, S. *et al.* (2015) 'Combining lidar and synthetic aperture radar data to estimate forest biomass: Status and prospects', *Forests*, 6(1), pp. 252–270. doi: 10.3390/f6010252.

De Keersmaecker, W. *et al.* (2014) 'How to measure ecosystem stability? An evaluation of the reliability of stability metrics based on remote sensing time series across the major global ecosystems', *Global Change Biology*, 20(7), pp. 2149–2161. doi: 10.1111/gcb.12495.

De Keersmaecker, W. *et al.* (2015) 'A model quantifying global vegetation resistance and resilience to short-term climate anomalies and their relationship with vegetation cover', *Global Ecology and Biogeography*, 24(5), pp. 539–548. doi: 10.1111/geb.12279.

Kéfi, S. *et al.* (2007) 'Spatial vegetation patterns and imminent desertification in Mediterranean arid ecosystems', *Nature*, 449(7159), pp. 213–217. doi: 10.1038/nature06111.

Kéfi, S. *et al.* (2014) 'Early warning signals of ecological transitions: Methods for spatial patterns', *PLoS ONE*, 9(3), pp. 10–13. doi: 10.1371/journal.pone.0092097.

King, M. D. *et al.* (2003) 'Cloud and aerosol properties, precipitable water, and profiles of temperature and water vapor from MODIS', *IEEE Transactions on Geoscience and Remote Sensing*, 41(2 PART 1), pp. 442–456. doi: 10.1109/TGRS.2002.808226.

Knauer, K. *et al.* (2014) 'Remote sensing of vegetation dynamics in West Africa', *International Journal of Remote Sensing*. Taylor & Francis, 35(17), pp. 6357–6396. doi: 10.1080/01431161.2014.954062.

Konings, A. G. *et al.* (2011) 'Drought sensitivity of patterned vegetation determined by rainfall-land surface feedbacks', *Journal of Geophysical Research: Biogeosciences*, 116(4), pp. 1–15. doi: 10.1029/2011JG001748.

Kusserow, H. (2017) 'Desertification , resilience , and re-greening in the African Sahel – a matter of the observation period ?', pp. 1141–1170.

Lasco, R. D. *et al.* (2014) 'Climate risk adaptation by smallholder farmers : the roles of trees and agroforestry', *Current Opinion in Environmental Sustainability*. Elsevier B.V., 6, pp. 83–88. doi: 10.1016/j.cosust.2013.11.013.

Le, Q. B., Nkonya, E. and Mirzabaev, A. (2016) 'Biomass productivity-based mapping of global land degradation hotspots', *Economics of Land Degradation and Improvement - A Global Assessment for Sustainable Development*, pp. 55–84. doi: 10.1007/978-3-319-19168-3_4.

Leblanc, M. J. *et al.* (2008) 'Land clearance and hydrological change in the Sahel: SW Niger', *Global and Planetary Change*, 61(3–4), pp. 135–150. doi: 10.1016/j.gloplacha.2007.08.011.

Lees, K. J. *et al.* (2021) 'Using remote sensing to assess peatland resilience by estimating soil surface moisture and drought recovery', *Science of the Total Environment*. Elsevier B.V., 761, p. 143312. doi: 10.1016/j.scitotenv.2020.143312.

Lenton, T. M. *et al.* (2008) 'Tipping elements in the Earth System', *Proceedings of the National Academy of Sciences of the United States of America*, 106(49), pp. 20561–20563. doi: 10.1073/pnas.0911106106.

Lenton, T. M. (2011) 'Early warning of climate tipping points', *Nature Climate Change*. Nature Publishing Group, 1(4), pp. 201–209. doi: 10.1038/nclimate1143.

Lenton, T. M. (2020) 'Tipping positive change', *Philosophical Transactions of the Royal Society B: Biological Sciences*, 375(1794), pp. 0–2. doi: 10.1098/rstb.2019.0123.

Lenton, T. M. *et al.* (2022) 'A resilience sensing system for the biosphere', *Phil. Trans. R. Soc. B*. Available at: https://doi.org/10.1098/rstb.2021.0383.

Leprun, J. C. (1999) 'The influences of ecological factors on tiger bush and dotted bush patterns along a gradient from Mali to northern Burkina Faso.', *Catena*, 37(1–2), pp. 25–44.

Lewis, S. L. and Maslin, M. A. (2015) 'Defining the Anthropocene', *Nature*. Nature Publishing Group, 519(7542), pp. 171–180. doi: 10.1038/nature14258.

Li, D. *et al.* (2018) 'Vulnerability of the global terrestrial ecosystems to climate change', *Global Change Biology*, 24(9), pp. 4095–4106. doi: 10.1111/gcb.14327.

Li, S. *et al.* (2019) 'Deep learning for hyperspectral image classification: An overview', *IEEE*

Transactions on Geoscience and Remote Sensing, 57(9), pp. 6690–6709. doi: 10.1109/TGRS.2019.2907932.

Litzow, M. A., Urban, J. D. and Laurel, B. J. (2008) 'Increased spatial variance accompanies reorganization of two continental shelf ecosystems', *America*, 18(6), pp. 1331–1337.

Liu, Y. *et al.* (2015) 'Spatial and Temporal Patterns of Global NDVI Trends: Correlations with Climate and Human Factors', pp. 13233–13250. doi: 10.3390/rs71013233.

Liu, Y. *et al.* (2019) 'Reduced resilience as an early warning signal of forest mortality', *Nature Climate Change*. Springer US, 9(11), pp. 880–885. doi: 10.1038/s41558-019-0583-9.

Loveland, T. R. and Irons, J. R. (2016) 'Landsat 8: The plans, the reality, and the legacy', *Remote Sensing of Environment*. Elsevier Inc., 185, pp. 1–6. doi: 10.1016/j.rse.2016.07.033.

MacQueen, J. (1967) 'Some methods for classification and analysis of multivariate observations', in *Proceedings of the fifth Berkeley symposium on mathematical statistics and probability*, pp. 281–297.

Mafongoya, P. *et al.* (2016) 'Maize productivity and pro fi tability in Conservation Agriculture systems across agro-ecological regions in Zimbabwe : A review of knowledge and practice', *Agriculture, Ecosystems and Environment*. Elsevier B.V., 220, pp. 211–225. doi: 10.1016/j.agee.2016.01.017.

Majumder, S. *et al.* (2019) 'Inferring critical thresholds of ecosystem transitions from spatial data', *Ecology*, 100(7). doi: 10.1002/ecy.2722.

Malenovský, Z. *et al.* (2012) 'Sentinels for science: Potential of Sentinel-1, -2, and -3 missions for scientific observations of ocean, cryosphere, and land', *Remote Sensing of Environment*, 120, pp. 91–101. doi: 10.1016/j.rse.2011.09.026.

Mander, L. *et al.* (2017) 'A morphometric analysis of vegetation patterns in dryland ecosystems', *Royal Society Open Science*, 4(2). doi: 10.1098/rsos.160443.

May, J. F., Guengant, J. P. and Barras, V. (2017) 'Demographic challenges of the Sahel countries.', in *Africa's Population: In Search of a Demographic Dividend*. Springer, Cham.

Mayor, Á. G. *et al.* (2013) 'Feedbacks between vegetation pattern and resource loss dramatically decrease ecosystem resilience and restoration potential in a simple dryland model', *Landscape Ecology*, 28(5), pp. 931–942. doi: 10.1007/s10980-013-9870-4.

Mbow, C. *et al.* (2014) 'Achieving mitigation and adaptation to climate change through sustainable agroforestry practices in Africa', *Current Opinion in Environmental Sustainability*. Elsevier B.V., 6(October 2013), pp. 8–14. doi:

10.1016/j.cosust.2013.09.002.

Mbow, C. *et al.* (2015) 'What Four Decades of Earth Observation Tell Us about Land Degradation in the Sahel?', (1), pp. 4048–4067. doi: 10.3390/rs70404048.

McDowell, N. G. *et al.* (2011) 'The interdependence of mechanisms underlying climate-driven vegetation mortality', *Trends in Ecology and Evolution*, 26(10), pp. 523–532. doi: 10.1016/j.tree.2011.06.003.

Meijer, S. S. *et al.* (2015) 'The role of knowledge , attitudes and perceptions in the uptake of agricultural and agroforestry innovations among smallholder farmers in sub- Saharan Africa', *International Journal of Agricultural Sustainability*. Taylor & Francis, 13(1), pp. 40–54. doi: 10.1080/14735903.2014.912493.

Meron, E. and Gilad, E. (2004) 'Vegetation patterns along a rainfall gradient', 19, pp. 367–376. doi: 10.1016/S0960-0779(03)00049-3.

Moesinger, L. *et al.* (2020) 'The global long-term microwave Vegetation Optical Depth Climate Archive (VODCA)', *Earth System Science Data*, 12(1), pp. 177–196. doi: 10.5194/essd-12-177-2020.

Myers-Smith, I. H. *et al.* (2020) 'Complexity revealed in the greening of the Arctic', *Nature Climate Change*. Springer US, 10(2), pp. 106–117. doi: 10.1038/s41558-019-0688-1.

Ndayambaje, J. D. and Mohren, G. M. J. (2011) 'Fuelwood demand and supply in Rwanda and the role of agroforestry', *Agroforestry Systems*, 83, pp. 303–320. doi: 10.1007/s10457-011-9391-6.

Van Nes, E. H. and Scheffer, M. (2007) 'Slow Recovery from Perturbations as a Generic Indicator of a Nearby Catastrophic Shift', 169(6).

Nicholson, S. E., Fink, A. H. and Funk, C. (2018) 'Assessing recovery and change in West Africa's rainfall regime from a 161-year record', *International Journal of Climatology*, 38(10), pp. 3770–3786. doi: 10.1002/joc.5530.

Nicholson, S. E., Tucker, C. J. and Ba, M. B. (1998) 'Desertification, Drought, and Surface Vegetation: An Example from the West African Sahel', *Bulletin of the American Meteorological Society*, 79(5), p. 815=830.

Nieke, J. and Mavrocordatos, C. (2017) 'Sentinel-3a: commissioning phase results of its optical payload', *International Conference on Space Optics*, 10562(October 2016), p. 187. doi: 10.1117/12.2296174.

Oborny, B., Meszéna, G. and Szabó, G. (2005) 'Dynamics of populations on the verge of extinction', *Oikos*, 109(2), pp. 291–296. doi: 10.1111/j.0030-1299.2005.13783.x.

Oppenheimer, S. (2011) 'Impact Evaluation of the TIST Program in Kenya', pp. 1–38. Available at: http://www.tist.org/tist/docs/PDD-

Documents/TIST%25%0A20KE%2520PD-VCS-Ex23%2520GL2%2520Community%2520Survey%2520Result.pdf.

Penny, G. G., Daniels, K. E. and Thompson, S. E. (2013) 'Local properties of patterned vegetation: Quantifying endogenous and exogenous effects', *Philosophical Transactions of the Royal Society A: Mathematical, Physical and Engineering Sciences*, 371(2004). doi: 10.1098/rsta.2012.0359.

Pettorelli, N., Vik, J.O., Mysterud, A., Gaillard, J.M., Tucker, C.J. and Stenseth, N.C., (2005). Using the satellite-derived NDVI to assess ecological responses to environmental change. *Trends in ecology & evolution*, *20*(9), pp.503-510.

Pimm, S. L. (1984) 'Complexity and stability of ecosystems', *Nature*, 307.

QGIS.org (2021) 'QGIS Geographic Information System'. QGIS Association. Available at: http://www.qgis.org.

R Core Team (2021) 'A Language and Environment for Statistical Computing', *R Foundation for Statistical Computing*. Vienna, Austria.: R Foundation for Statistical Computing, p. https://www.R-project.org. Available at: http://www.r-project.org.

Raleigh, C. (2010) 'Political Marginalization, Climate Change, and Conflict in African Sahel States', *International Studies Review*, 12(1), pp. 69–86. doi: 10.1111/j.1468-2486.2009.00913.x.

Reed, M. S. (2007) 'Participatory technology development for agroforestry extension : an innovation-decision approach', *African Journal of Agricultural Research*, 2(8), pp. 334–341. Available at: http://link.springer.com/article/10.1007%2FBF00120189#.

Riché, G. and Ségalen, P. (1971) 'Evolution du relief et pédogenèse dans la basse vallée du Wabi-Shebelli (Ethiopie)', *Cahiers ORSTOM, série pédologie*, 9(2), pp. 189–203.

Rietkerk, M. *et al.* (2004) 'Self-Organized Patchiness and Catastrophic Shifts in Ecosystems', *Science*, 305. doi: 10.1126/science.1101867.

Rietkerk, M. *et al.* (2021) 'Evasion of tipping in complex systems through spatial pattern formation', 169(October). doi: 10.1126/science.abj0359.

Rietkerk, M. and Koppel, J. Van De (2008) 'Regular pattern formation in real ecosystems', (February). doi: 10.1016/j.tree.2007.10.013.

Rocha, J. C. (2021) 'Ecosystems are showing symptoms of resilience loss', *[Preprint]*, pp. 1–19. Available at: http://arxiv.org/abs/2107.03307.

Rouse, J. W. (1973) *Monitoring the vernal advancement and retro gradation of natural vegetation*.

Rouse, J. W., Benton, A. R. and Haas, R. H. (1975) 'Three examples of applied remote sensing

of vegetation', *NASA Lyndon B. Johnson Space Center NASA Earth Resouces Surv. Symp,* 1–C.

Salati, E. *et al.* (1979) 'Recycling of water in the Amazon Basin: An isotopic study', *Water Resources Research*, 15(5), pp. 1250–1258. doi: 10.1029/WR015i005p01250.

Sanchez, P. A. (2002) 'Soil fertility and hunger in Africa', *Science*, 295(5562), pp. 2019–2020. doi: 10.1126/science.1065256.

Scheffer, M. *et al.* (2001) 'Catastrophic shifts in ecosystems', *Nature*, 413(6856), pp. 591–596. doi: 10.1038/35098000.

Scheffer, M. *et al.* (2009) 'Early-warning signals for critical transitions', *Nature*, 461(7260), pp. 53–59. doi: 10.1038/nature08227.

Scheffer, M. *et al.* (2012) 'Anticipating Critical Transitions', *Science*, 338(6105), pp. 344–348. doi: 10.1126/science.1225244.

Scheffer, M. *et al.* (2015) 'Generic Indicators of Ecological Resilience: Inferring the Chance of a Critical Transition', *Annual Review of Ecology, Evolution, and Systematics*, 46(1), pp. 145–167. doi: 10.1146/annurev-ecolsys-112414-054242.

Schmocker, J. *et al.* (2016) 'Trends in mean and extreme precipitation in the Mount Kenya region from observations and reanalyses', 1514(August 2015), pp. 1500–1514. doi: 10.1002/joc.4438.

Schwalm, C. R. *et al.* (2017) 'Global patterns of drought recovery', *Nature*. Nature Publishing Group, 548(7666), pp. 202–205. doi: 10.1038/nature23021.

Seddon, A. W. R. *et al.* (2016) 'Sensitivity of global terrestrial ecosystems to climate variability', *Nature*. Nature Publishing Group, 531(7593), pp. 229–232. doi: 10.1038/nature16986.

Shames, S. *et al.* (2012) *Institutional innovations in African smallholder carbon projects*, *CCAFS Report No. 8*. Copenhagen, Denmark.

Short, N. M. (1976) 'Mission to Earth: Landsat views the world', *Scientific and Technical Office, National Aeronautics and Space Administration*, Vol. 1.

Siero, E. *et al.* (2015) 'Striped pattern selection by advective reaction-diffusion systems: Resilience of banded vegetation on slopes', *Chaos*, 25(3). doi: 10.1063/1.4914450.

Siero, E. *et al.* (2019) 'Grazing Away the Resilience of Patterned Ecosystems', 193(3). doi: 10.1086/701669.

Smith, T., Traxl, D. and Boers, N. (*in press*) 'Empirical Evidence for Global Declines in Vegetation Resilience', *Nature Climate Change*.

Staver, A. C., Archibald, S. and Levin, S. A. (2011) 'The global extent and determinants of

savanna and forest as alternative biome states', *Science*, 334(6053), pp. 230–232. doi: 10.1126/science.1210465.

Storey, J., Scaramuzza, P. and Schmidt, G. (2005) 'Landsat 7 scan line corrector-off gap filled product development.', in *PECORA 16 Conference Procedings*. Sioux Falls, South Dakota, pp. 23–27.

Su, H. *et al.* (2021) 'Long-term empirical evidence, early warning signals and multiple drivers of regime shifts in a lake ecosystem', *Journal of Ecology*, 109(9), pp. 3182–3194. doi: 10.1111/1365-2745.13544.

Takimoto, G. (2009) 'Early warning signals of demographic regime shifts in invading populations', pp. 419–426. doi: 10.1007/s10144-009-0148-2.

Thépaut, J. N. *et al.* (2018) 'The Copernicus programme and its climate change service', in *International Geoscience and Remote Sensing Symposium (IGARSS)*, pp. 1591–1593. doi: 10.1109/IGARSS.2018.8518067.

Thorlakson, T. and Neufeldt, H. (2012) 'Reducing subsistence farmers ' vulnerability to climate change : evaluating the potential contributions of agroforestry in western Kenya', pp. 1–13.

Tian, J., Wang, L., Li, X., Gong, H., Shi, C., Zhong, R. and Liu, X., (2017). Comparison of UAV and WorldView-2 imagery for mapping leaf area index of mangrove forest. *International journal of applied earth observation and geoinformation*, *61*, pp.22-31.

Tirabassi, G. *et al.* (2014) 'Interaction network based early-warning indicators of vegetation transitions', *Ecological Complexity*. Elsevier B.V., 19, pp. 148–157. doi: 10.1016/j.ecocom.2014.06.004.

TIST (2011) *The Tree: TIST Uganda December 2011 Newsletter*. Available at: https://program.tist.org/uganda-newsletters (Accessed: 5 February 2021).

TIST (2012) *Mazingira Bora: TIST Kenya January 2012 Newsletter*. Available at: https://program.tist.org/kenya-newsletters (Accessed: 5 February 2021).

Torres, R. *et al.* (2012) 'GMES Sentinel-1 mission', *Remote Sensing of Environment*. Elsevier Inc., 120, pp. 9–24. doi: 10.1016/j.rse.2011.05.028.

Trenberth, K. E. (2011) 'Changes in precipitation with climate change', *Climate Research*, 47(1–2), pp. 123–138. doi: 10.3354/cr00953.

Trichon, V. *et al.* (2018) 'The persistent decline of patterned woody vegetation: The tiger bush in the context of the regional Sahel greening trend', *Global Change Biology*, 24(6), pp. 2633–2648. doi: 10.1111/gcb.14059.

Turing, A. M. (1952) 'The chemical basis of morphogenesis', *Bulletin of Mathematical*

Biology, 52(1–2), pp. 153–197. doi: 10.1007/BF02459572.

Tyc, G. *et al.* (2005) 'The RapidEye mission design', *Acta Astronautica*, 56(1–2), pp. 213–219. doi: 10.1016/j.actaastro.2004.09.029.

Valentin, C. and D'Herbès, J. M. (1999) 'Niger tiger bush as a natural water harvesting system', *Catena*, 37(1–2), pp. 231–256. doi: 10.1016/S0341-8162(98)00061-7.

Veraart, A. J. *et al.* (2012) 'Recovery rates reflect distance to a tipping point in a living system', *Nature*, 481(7381), pp. 357–359. doi: 10.1038/nature10723.

Verbesselt, J. *et al.* (2016) 'Remotely sensed resilience of tropical forests', *Nature Climate Change*, 6(11), pp. 1028–1031. doi: 10.1038/nclimate3108.

Walsh, J. E. *et al.* (2020) 'Extreme weather and climate events in northern areas: A review', *Earth-Science Reviews*. Elsevier, 209(December 2019), p. 103324. doi: 10.1016/j.earscirev.2020.103324.

Wang, C. J., Zhang, Z. X. and Wan, J. Z. (2019) 'Vulnerability of global forest ecoregions to future climate change', *Global Ecology and Conservation*. Elsevier Ltd, 20, p. e00760. doi: 10.1016/j.gecco.2019.e00760.

Wang, J. *et al.* (2004) 'Relations between NDVI and tree productivity in the central Great Plains', *International Jounal of Remote Sensing*, 25(16), pp. 3127–3138. doi: 10.1080/0143116032000160499.

Waring, R.H. (1983). Estimating forest growth and efficiency in relation to canopy leaf area. In *Advances in ecological research* (Vol. 13, pp. 327-354). Academic Press.

Waswa, B. S. *et al.* (2013) 'Evaluating indicators of land degradation in smallholder farming systems of western Kenya', *Geoderma*. Elsevier B.V., 195–196, pp. 192–200. doi: 10.1016/j.geoderma.2012.11.007.

Webb, N. P. *et al.* (2017) 'Land degradation and climate change: building climate resilience in agriculture', *Frontiers in Ecology and the Environment*, 15(8), pp. 450–459. doi: 10.1002/fee.1530.

White, H. J. *et al.* (2020) 'Quantifying large-scale ecosystem stability with remote sensing data', *Remote Sensing in Ecology and Conservation*, 6(3), pp. 354–365. doi: 10.1002/rse2.148.

White, H. J. *et al.* (2021) 'Ecosystem stability at the landscape scale is primarily associated with climatic history', (October), pp. 1–13. doi: 10.1111/1365-2435.13957.

Willemen, L. *et al.* (2020) 'How to halt the global decline of lands', *Nature Sustainability*. Springer US, 3(3), pp. 164–166. doi: 10.1038/s41893-020-0477-x.

Williams, D. L., Goward, S. and Arvidson, T. (2006) 'Landsat: Yesterday, Today , and

Tomorrow', *Photogrammetric Engineering & Remote Sensing*, 72(10), pp. 1171–1178.

De Wispelaere, G. (1980) 'Les photographies aériennes témoins de la dégradation du couvert ligneux dans un géosystème sahélien sénégalais.', *Cahiers ORSTOM, série Sc. Hum*, 27(3–4), pp. 155–166.

Wissel, C. (1984) 'A universal law of the characteristic return time near thresholds', *Oecologia*, 65(1), pp. 101–107. doi: 10.1007/BF00384470.

Woodcock, C. E. *et al.* (2008) 'Free access to landsat imagery', *Science*. American Association for the Advancement of Science, 320(5879), p. 1011. doi: 10.1126/SCIENCE.320.5879.1011A/ASSET/702BD2AE-519F-42A1-9E01-18FC13B57888/ASSETS/GRAPHIC/1011A-1.GIF.

Wu, J. and Liang, S. (2020) 'Assessing Terrestrial Ecosystem Resilience using Satellite Leaf Area Index', *Remote Sensing*, pp. 1–20.

Wulder, M. A. *et al.* (2012) 'Opening the archive : How free data has enabled the science and monitoring promise of Landsat', *Remote Sensing of Environment*. Elsevier B.V., 122, pp. 2–10. doi: 10.1016/j.rse.2012.01.010.

Wulder, M. A. *et al.* (2019) 'Environment Current status of Landsat program , science , and applications', 225(November 2018), pp. 127–147. doi: 10.1016/j.rse.2019.02.015.

Wuyts, B., Champneys, A. R. and House, J. I. (2017) 'Amazonian forest-savanna bistability and human impact', *Nature Communications*. Nature Publishing Group, 8(May), pp. 1–11. doi: 10.1038/ncomms15519.

Yin, Z. *et al.* (2016) 'Network based early warning indicators of vegetation changes in a land-atmosphere model', *Ecological Complexity*. Elsevier B.V., 26, pp. 68–78. doi: 10.1016/j.ecocom.2016.02.004.

Zhang, Y. *et al.* (2016) 'Multiple afforestation programs accelerate the greenness in the "Three North" region of China from 1982 to 2013', *Ecological Indicators*. Elsevier Ltd, 61, pp. 404–412. doi: 10.1016/j.ecolind.2015.09.041.

Zhu, X. and Liu, D., (2015). Improving forest aboveground biomass estimation using seasonal Landsat NDVI time-series. *ISPRS Journal of Photogrammetry and Remote Sensing*, *102*, pp.222-231